Performance of solution processable perovskite solar cells under a simulated Mars environment

By:
Rokas Apanavicius

Submitted to Swansea University in fulfilment of the requirements for the Degree of MSc in Materials Engineering by Research

Swansea University
2024

Summary

This thesis explores the performance and stability of solution-processable perovskite solar cells, focusing on methylammonium lead iodide ($MAPbI_3$) and triple cation ($Cs_{0.05}(MA_{0.17}FA_{0.83})_{0.95}Pb(I_{0.17}Br_{0.13})_3$) perovskite formulations, under conditions that simulate the extreme environment on Mars. The primary goal was to assess how well these perovskite devices perform when subjected to Martian-like temperature fluctuations and humidity variations, with a particular emphasis on their power conversion efficiency and long-term stability. By delving into this unique setting, the research aims to advance the understanding of perovskite solar cells in non-Earth conditions and their potential for space applications.

The devices were tested across a wide range of temperatures, from 20 °C to -125 °C, and exposed to varying humidity levels from 10% to 90% relative humidity, mimicking Martian extremes within controlled environmental chambers.

The results show that triple cation perovskite solar cells consistently outperform $MAPbI_3$ devices, demonstrating better efficiency and stability during thermal cycling and temperature profiles designed to reflect Jezero Crater on Mars. Interestingly, $MAPbI_3$ devices showed improved stability at temperatures below -50 °C, highlighting their potential under extremely cold conditions. In addition, the triple cation perovskites outperformed $MAPbI_3$ in humidity tests, exhibiting greater stability, though both types of solar cells experienced significant fluctuations in performance when exposed to high humidity for prolonged periods.

Nonetheless, the device degradation caused by extreme temperatures and humidity is a major obstacle. These issues underscore the necessity for further research to optimise device longevity and performance for future space exploration.

DECLARATION

This work has not previously been accepted in substance for any degree and is not being concurrently submitted in candidature for any degree.

Signed [redacted]

Date 15/09/2024

STATEMENT 1

This thesis is the result of my own investigations, except where otherwise stated and other sources are acknowledged by footnotes giving explicit references. A bibliography is appended.

Signed [redacted]

Date 15/09/2024

STATEMENT 2

I hereby give consent for my thesis, if accepted, to be available for electronic sharing.

Signed [redacted]

Date 15/09/2024

STATEMENT 3

The University's ethical procedures have been followed and, where appropriate, that ethical approval has been granted.

Signed [redacted]

Date 15/09/2024

Table of Contents

Acknowledgements

I would like to express my deepest gratitude to my academic supervisor, Dr. Wing Chung Tsoi, for suggesting this fascinating topic and for his unwavering support throughout the course of my research. His guidance, introduction to esteemed colleagues, and readiness to assist with any challenges, even those outside the scope of the project, have been invaluable.

I am also profoundly grateful to Dr. Declan Hughes, who served as an unofficial second supervisor. His dedication, including taking time away from his own projects to help me set up, run, and maintain the lab equipment, has been instrumental in the success of this research. Dr. Hughes's willingness to answer questions and aid, both within and outside university hours, has greatly contributed to my progress and understanding.

Lastly, I would like to extend my sincere thanks to Dr. Ram Datt. His constant presence and eagerness to help with any issues I encountered have been a source of great encouragement. His support has been crucial in navigating the various challenges faced during this research.

To all of you, thank you for your invaluable contributions and unwavering support.

List of Figures and Tables

List of Abbreviations

AC	Alternating Current
AM	Air-Mass
Au	Gold
Br	Bromide
$CaTiO_3$	Calcium titanium oxide
CdTe	Cadmium Telluride
CH_3NH_3I	Methylammonium Iodide
$CH_3NH_3PbI_3$	$MAPbI_3$
CIGS	Cu(In,Ga)Se2
Cl	Chloride
Cs	Cesium
$Cs_{0.05}(MA_{0.17}FA_{0.83})_{0.95}Pb(I_{0.17}Br_{0.13})_3$	Triple cation perovskite
CsFAMA	$Cs_{0.05}(MA_{0.17}FA_{0.83})_{0.95}Pb(I_{0.17}Br_{0.13})_3$
DC	Direct Current
DMF	N,N-Dimethylformamide
DMSO	Dimethyl Sulfoxide
E_B	Binding Energy of Excitons
E_g	Band Gap Energy
EQE	External Quantum Efficiency
ETL	Electron Transport Layer
FA	Formamidinium
FAI	Formamidinium Iodide
FF	Fill Factor
FS	Forward Scan
FWHM	Full Width At Half Maximum
GaAs	Gallium Arsenide
GaInP	Indium gallium phosphide
Ge	Germanium
H_2	Hydrogen
H_2O	Water
HI	Hydrogen Iodide
HTL	Hole Transport Layer
I	Iodide
I_2	Iodine
InP	Indium phosphide
ITO	Indium Doped Tin Oxide
J_{SC}	Short-Current Density
J-V	Current–Voltage
LTST	Local True Solar Time
MA	Methylammonium
MaBr	Methylammonium Bromide
$MAPbI_3$	Methylammonium Lead Iodide

MAPI	Methylammonium Lead Iodide
N_2	Nitrogen
ND	Neutral Density
n-i-p	n-type layer (ETL), intrinsic layer (perovskite absorber layer), p-type layer (HTL)
O_2	Oxygen
OC	Open-Circuit
P3HT	Regioregular Poly(3-Hexylthiophene-2,5-Diyl)
Pb	Lead
$PbBr_2$	Lead Bromide
PbI_2	Lead Iodide
PCBM	fullerene derivative [6,6]-phenyl-C_{61}-butyric acid methyl ester
PCE	Power Conversion Efficiency
p-i-n	p-type layer (HTL), intrinsic layer (perovskite absorber layer), n-type layer (ETL)
PL	Photoluminescence
PL_{OC}	Open-Circuit Photoluminescence
PL_{SC}	Short-Circuit Photoluminescence
pr-µm	µm of precipitable water
PTAA	Poly[Bis(4-Phenyl)(2,4,6-Trimethylphenyl)Amine
PTFE	Polytetrafluoroethylene
R2R	Roll to roll
Rb	Rubidium
RH	Relative Humidity
RS	Reverse Scan
SC	Short-Circuit
Si	Silicon
Sn	Tin
SnO_2	Tin Oxide
Spiro-OMeTAD	2,2',7,7'-Tetrakis[N,N-Di-P-Methoxyphenyl-Amine] 9,9'-Spirobifluore
TC	Triple Cation
TiO_2	Titanium Dioxide
UV	Ultraviolet
V_{OC}	Open-Circuit Voltage
ZnO	Zinc oxide

Chapter 1: Introduction

This chapter offers a brief introduction to Mars and its unique environmental conditions, exploring the concept of Mars exploration and potential landing locations on the planet. Solar energy is highlighted as a critical resource for powering and sustaining the equipment on Mars. Additionally, the chapter delves into perovskite solar cells, which could be an intriguing option for Martian environments. It explains their operational principles and discusses their potential and challenges posed by the atmospheric conditions of Mars.

1.1 Solar Cells

The quest for sustainable and clean energy sources has become one of the foremost challenges of the 21st century. Among the various renewable energy options, solar energy stands out due to its ubiquitous availability, high energy potential, and minimal environmental impact.

Using solar cells is an effective, reliable, clean, and limitless way to convert solar energy into electricity. The history of solar cell technology dates to 1839, when Edmund Bequerel discovered the photoelectric effect, noting that light could create a current between platinum electrodes in a metal halide solution. The modern era of photovoltaic devices began in 1954 with Bell Labs' creation of the first silicon solar cell, which had a modest power conversion efficiency of 6%. The oil crisis of the 1970s sparked significant scientific interest and investment in PV technology, leading to major advancements and cost reductions [1].

For decades, silicon-based solar cells have been at the forefront of terrestrial photovoltaic technology due to relative abundance and environmentally friendly nature of silicon. Nevertheless, it has a severe drawback. Firstly, crystalline silicon is an indirect semiconductor and therefore is a relatively poor absorber of long-wavelength sunlight [2]. To offset this, a thick silicon structure is used. Although this thickness enhances solar absorption, it also results in a rigid structure. Additionally, silicon solar cells are expensive to produce because their processing requires a significant amount of energy [3]. These limitations have spurred considerable interest in various thin-film solar materials, including cadmium telluride (CdTe), perovskites, and various polymers [4]. Thin-film PV offers advantages such as low-cost production and reduced material usage. It supports a wide range of applications, semi-transparent devices, and the ability to deposit on various substrates, including flexible materials.

For extraterrestrial applications the picture is different though. III-V solar cells are predominant in space applications due to their high efficiency and radiation resistance. The history of solar cells in space dates back to the Vanguard 1 satellite, launched in 1958, marking the beginning of space photovoltaics [5].

Over the past two decades, GaInP/GaAs/Ge triple-junction cells have become a staple in space missions, consistently achieving efficiencies exceeding 30%. Despite their high efficiency, multijunction solar cells (MJSCs) have limitations such as rigidity, significant thickness (~80 to ~200 µm) and complex and costly fabrication process [6]. With the rapidly growing demand for more compact, lightweight, and cheaper satellites the need to find alternative PV technologies has arisen and there are several options like silicon (Si), copper indium gallium selenide (CIGS) and perovskite solar cells.

Silicon solar cells, which achieve a PCE of 26.1% in lab-scale devices, are attractive for short-duration missions due to their lower production costs when compared to other aerospace grade solar cell technologies. However, they are non-flexible, heavy (thickness >100 µm), and require labour intensive manufacturing processes.

Cu(In,Ga)Se2 (CIGS) thin-film solar cells offer advantages such as high radiation resistance, light weight, and flexibility, making them ideal for next-generation space missions. They can be produced using low-cost techniques and adapted to various shapes, simplifying spacecraft design. However, their relatively low PCE (23.4%) limits their use in satellites [7].

As the search for alternative photovoltaic technologies intensifies, the spotlight now shifts to perovskite solar cells (PSCs). Unlike traditional silicon and CIGS technologies, PSCs offer a distinct combination of high efficiency, low-cost production through solution processing methods, and a flexible, lightweight design that is well-suited for space applications. Notably, their exceptional radiation hardness further underscores their potential in the rigorous environment of space. In the next section, we explore the unique attributes and recent advancements in perovskite solar cell technology, highlighting their promising role in shaping the future of space photovoltaics.

1.2 Perovskite Solar Cells

1.2.1 History

The term "perovskite" refers to a class of materials that possess the same crystal structure as calcium titanium oxide ($CaTiO_3$). It was first discovered in the Ural Mountains of Russia by the German scientist Gustav Rose in 1839 and was subsequently named in honour of the Russian mineralogist Lev Perovski [8].

1.2.2 Characteristics

In scientific terms, a perovskite structure is typically represented by the formula ABX_3, where it mirrors the crystalline arrangement of the mineral perovskite. In this structure, as illustrated in figure 1.1, the A site is occupied by a monovalent cation (or positive ion), such as organic methylammonium (MA), formamidinium (FA), or an inorganic cation like cesium (Cs), rubidium (Rb), or combinations mix of these ions. The B site hosts divalent metal cations, commonly lead (Pb), tin (Sn), germanium (Ge), or their mixtures. The X site is occupied by monovalent anions (or halides), typically halides like iodide (I), bromide (Br), chloride (Cl), or a combination of these [9].

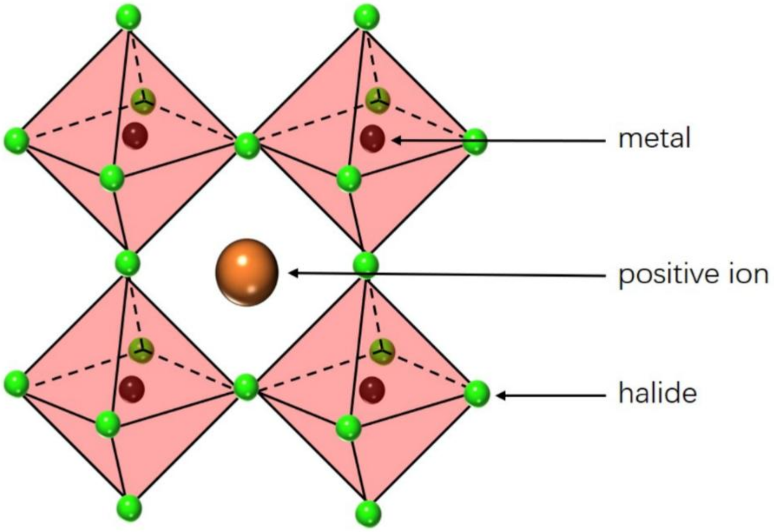

Figure 1. 1: Perovskite crystal structure. Halide ions (small green balls) create an octahedral shape (pink) around a metal atom (dark red ball). In the middle of a group of four octahedral shapes lies a positive ion (orange ball) [10].

Perovskites, a type of semiconductor material, demonstrate outstanding qualities in the field of solar cells. Single-junction perovskite cells currently achieve efficiencies surpassing 26%, are cheaper to produce because they can be fabricated at lower temperatures and use printing methods that work on both hard and flexible materials [11]. These attributes highlight the significant potential of perovskite solar cells in the photovoltaic market [12]. Their rapid technological advancement since their inception in 2009 positions them as strong contenders against other active layer-based solar cells like Si, CdTe, CIGS, and GaAs, as illustrated in figure 1.2 [13].

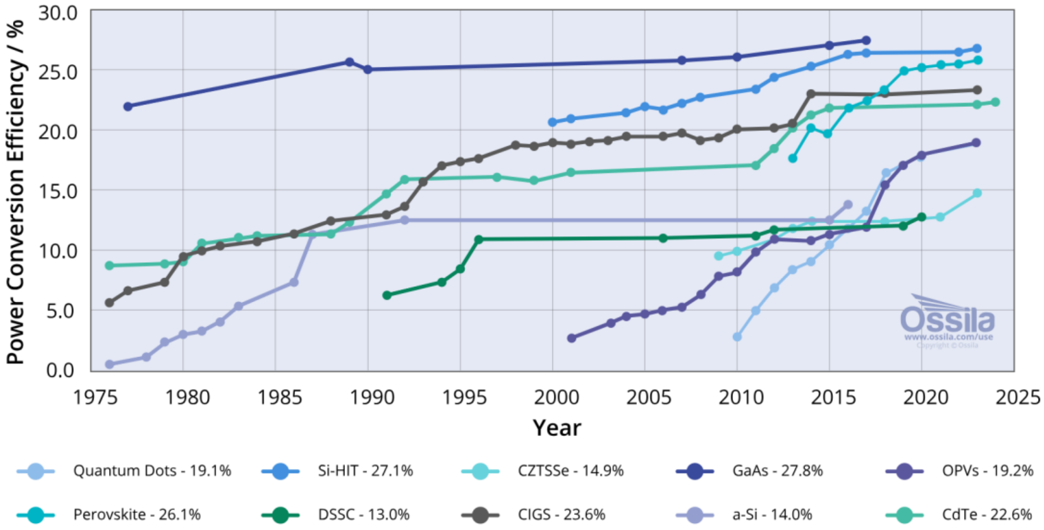

Figure 1. 2: a chart of the highest confirmed power conversion efficiencies of lab based-photovoltaic devices from 1976 to 2024 [14].

One of the most compelling attributes of PSCs is their high specific power, which is crucial for aerospace applications where weight is a critical factor. Flexible perovskite solar cells have demonstrated specific power values reaching up to 29.4 W g^{-1} [15], significantly outperforming other photovoltaic technologies like multi junction solar cells (~0.4–3.8 W g^{-1} for GaInP/GaAs/Ge), silicon (~0.38 W g^{-1}) and CIGS (~3 W g^{-1}), as illustrated in figure 1.3 [7]. This high power-to-weight ratio is essential for reducing the payload of spacecraft, thereby enhancing the efficiency and feasibility of space missions.

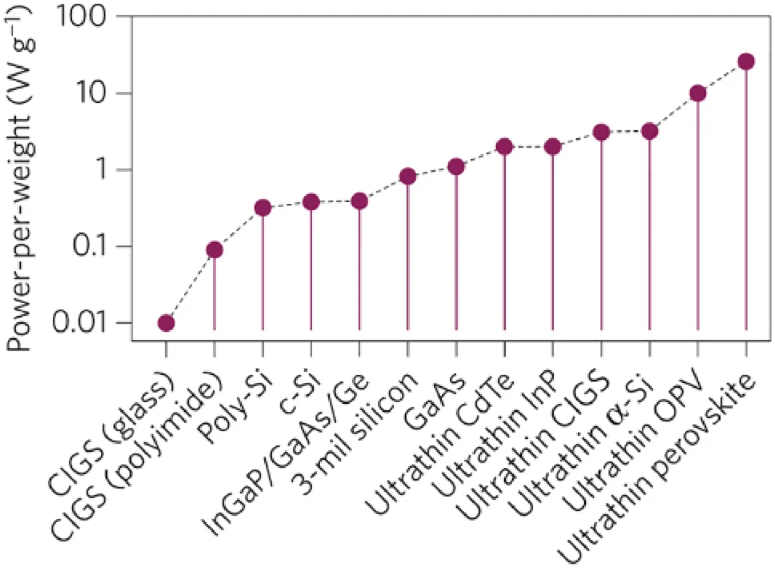

Figure 1. 3: Comparison of the power-to-weight ratio of common solar cells [16].

Another crucial factor is the maximum photon energy utilisation (defined as the open circuit voltage V_{OC} divided by the optical bandgap E_g). A high photon energy utilisation means that the solar cell is effectively using a sizeable portion of the photon's energy to generate electricity, rather than losing it as heat or other forms of energy. In figure 1.4 below, it is shown how much of a photon's energy is converted from light to electricity. Perovskite solar cells exceed almost 70% of photon energy utilisation, meaning they convert almost 70% of the photon's energy into electrical energy, and this has high potential to be improved. This is not far off top-class solar cells like GaAs, however, at a small fraction of the cost [14].

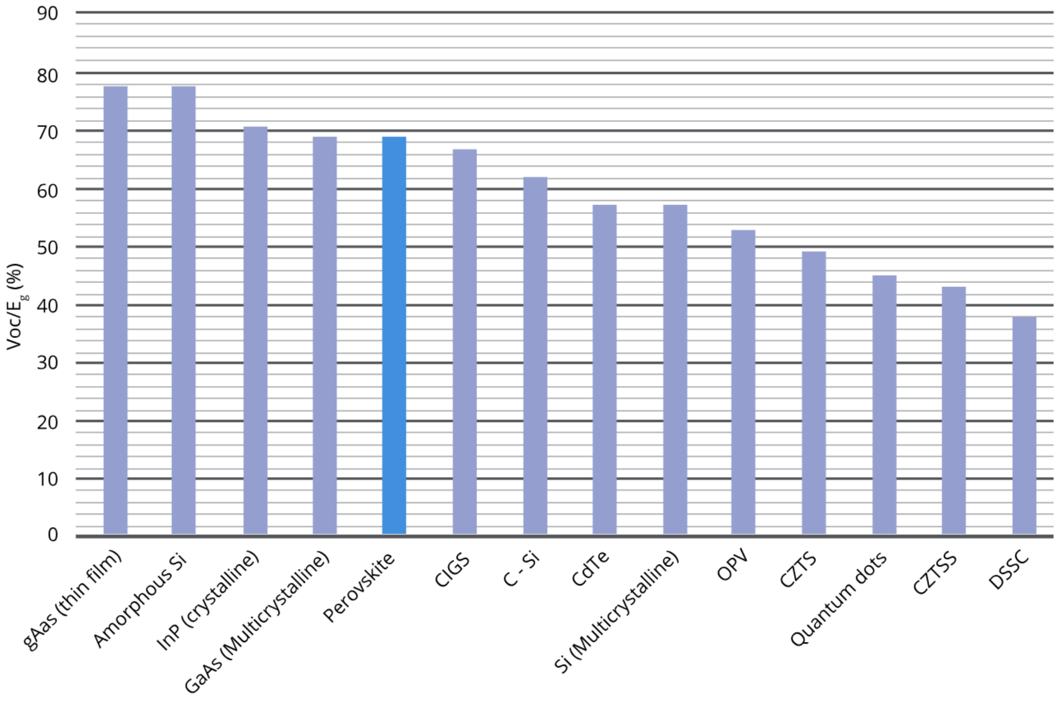

Figure 1. 4: The maximum photon energy utilisation for common single junction solar cells material systems.

Furthermore, perovskite-based solar cells demonstrate strong radiation resistance, which is crucial for their application in space environments. Studies have shown that PSCs can withstand high-energy electron and proton particle irradiation [17], UV [18] and gamma-ray [19] exposure with lesser PCE degradation when compared to other solar cell technologies [17]. However, they are not completely immune to space radiation. Increased lattice defects can accelerate the decomposition of perovskite, while energetic radiation particles can darken the glass substrate. These issues pose challenges that can adversely affect the performance and longevity of perovskite solar cells.

It is important to mention that not all perovskites are semiconductors. For semiconducting perovskites, the energy gap between the valence band (where electrons reside) and the conduction band (where electrons are free to move and conduct electricity) is small enough, allowing them to conduct electricity when excited by light, but they do not conduct as readily as metals. Metallic perovskites are a subclass of perovskite materials characterized by their high electrical conductivity, similar to that of metals, due to overlapping bands that allow for free electron movement. Lastly, perovskites can also exhibit insulating behaviour, where the energy gap between the valence band and conduction band is large enough that electrons cannot easily move across it. This results in high electrical resistance and prevents the material from conducting electricity effectively.

1.2.3 Challenges

However, perovskite solar cells are not perfect and face several challenges. Firstly, scaling up from lab-scale to industrial production is necessary, but producing large-scale, uniform crystalline thin films is difficult due to the strict defect tolerances required for films only a few hundred nanometres thick. Additionally, issues like toxicity, film stability, and the need for high-throughput manufacturing processes with high yields further complicate the process.

Secondly, ensuring long-term stability is a major concern. Unlike silicon and gallium arsenide solar cells, which have lifespans of about 20 years, perovskite solar cells have a much shorter lifespan and are prone to degradation from moisture, oxygen, heat, and light. [20]. Crystal defects, ion migration, and hysteresis further compromise their performance and stability [21].

Despite these challenges, considerable progress is being made in addressing them. For instance, the roll-to-roll (R2R) coating technique shows promise for large-scale production. Beynon *et al*. successfully fabricated fully R2R 20-meter-long flexible substrates, achieving a stabilized power conversion efficiency (PCE) of 10.8%. They accomplished this using low-cost and scalable carbon ink instead of the traditional, more expensive Spiro-OMeTAD/gold electrodes [22]. It is also noteworthy that the absence of moisture and oxygen in space mitigates some concerns regarding perovskite decomposition. Ongoing discussions focus on encapsulation and structural modifications to optimize perovskite solar cells for enhanced performance and stability. Due to their lightweight, efficient, and durable nature, perovskite solar cells are set to play a crucial role in future space exploration missions.

1.2.4 Device Structure

To begin, planar perovskite solar cells feature a simple, flat structure where the perovskite layer is sandwiched between an electron transport layer (ETL) and a hole transport layer (HTL). This structure can be arranged in two ways:

1) n-i-p (conventional) Configuration: The ETL is deposited first, followed by the perovskite layer and then the HTL.
2) p-i-n (inverted) Configuration: The HTL is deposited first, followed by the perovskite layer and then the ETL.

Planar perovskite structures are characterized by simple fabrication, larger perovskite grains, longer radiative recombination lifetimes and faster charge mobilities, highlighting a key advantage over mesoscopic morphologies. [23]. Each structure has its own set of advantages, but this discussion will focus on the planar (n-i-p) device structure.

Then, there is the mesoporous structure, as shown in figure 1.5. Mesoporous devices feature a mesoporous ETL scaffold, often made from titanium dioxide (TiO_2), embedded within the perovskite layer. These structures provide clear benefits for carrier transport and recombination resistance [24]. However, they are expensive to produce and unsuitable for creating flexible PSCs. This is because they require high-temperature sintering, typically over 500 °C, to remove organic materials from the TiO_2 paste and improve the crystallinity of the TiO_2 film [25].

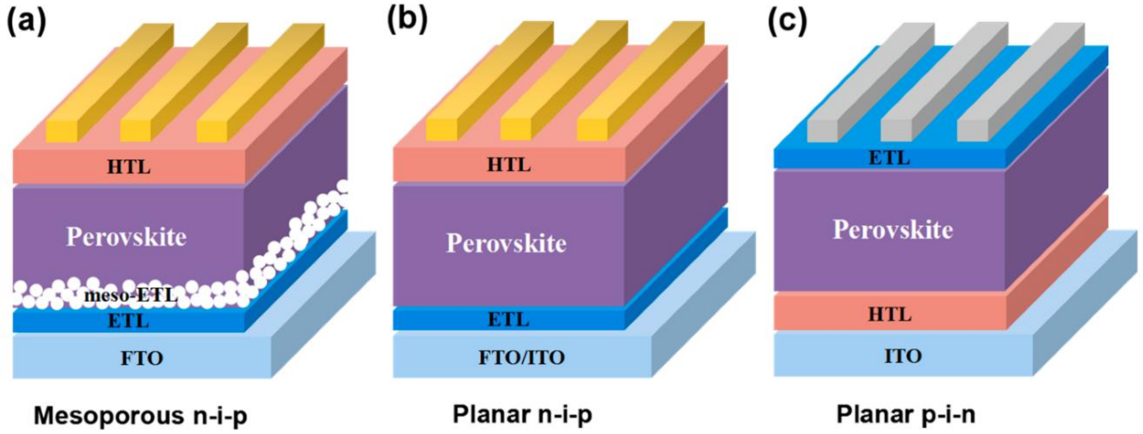

Figure 1. 5: Typical device structures of PSCs: (a) mesoporous n-i-p structure, (b) regular planar structure (n-i-p), and (c) inverted planar structure (p-i-n) [25].

1.3 Working Principle of Perovskite Solar Cells

1.3.1 Functions of the Layers

To fully understand the working principles of conventional structure perovskite solar cells, it is first, important to understand how each layer functions. An active perovskite layer is sandwiched between carrier transport layers, specifically a hole transport layer and an electron transport layer. They aid in the extraction and collection of charges, but they manage different types of charges – the HTL facilitates the movement of holes, while the ETL assists in electron transport.

The ETL (n-type region) performs a complementary role by aiding the extraction and collection of electrons from the perovskite layer and transferring them to the front electrode (cathode). It also blocks holes to prevent recombination at the front electrode. Typical ETL materials are ZnO, TiO_2, SnO_2 and PCBM.

The HTL (p-type region) serves multiple purposes: it aids in the extraction and collection of holes from the perovskite layer and transfers them to the back electrode (anode). It also blocks electrons to prevent recombination at the back electrode. Common HTL materials include Spiro-OMeTAD and P3HT.

The cathode and anode are the two electrodes that facilitate the flow of electric current when the cell generates power from sunlight. The cathode is responsible for collecting the electrons generated in the perovskite active layer and facilitating their movement out of the cell. The cathode used in conventional structured device is typically made from a transparent conductive oxide (TCO), such as fluorine-doped tin oxide (FTO), indium tin oxide (ITO) or aluminium-doped zinc oxide (AZO), they each share a combination of properties like low reflectivity, high transparency, excellent electrical conductivity, and ease of patterning.

The anode is typically the electrode where holes are collected. The anode used in conventional structured device is made of metals such as aluminium (Al), silver (Ag) or gold (Au), which efficiently facilitate the extraction of holes.

1.3.2 Working Principle

Solar cells operate on the principle of converting sunlight directly into electricity through the photovoltaic effect. The working principle of perovskite solar cells involves three main processes: light absorption, charge dissociation and separation, and charge transport to the electrodes (shown in figure 1.6).

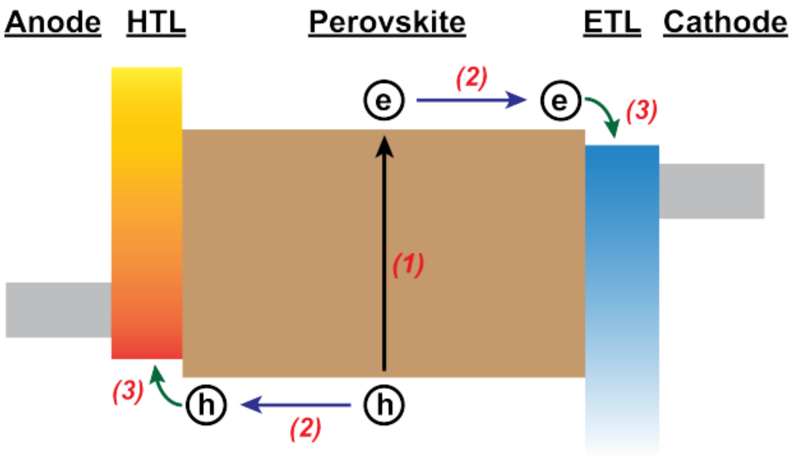

Figure 1. 6: The schematic of a perovskite solar cell's working principle. (1) Light absorption and generation of free electrons and holes; (2) Charge dissociation and separation; (3) Charge transport to their respective layers and extraction at the electrodes [26].

Initially, a thin layer of perovskite material absorbs sunlight. The minimum energy required to achieve the absorption of light is that the photon has energy equal or higher to the E_g of the material. The energy band gaps of active perovskite materials used in PSCs fall between 1.48 eV and 1.62 eV. For the highest-performing PSCs, the ideal band gap is usually within the narrow range of 1.53 eV to 1.56 eV [21]. Using compositional engineering, doping and interface engineering, however, the bandgap can be tuned to achieve better performance [27].

The absorption excites electrons moving them to a higher energy level. These excited electrons jump from a valence band to conduction band due to the electric field within the solar cell, which is created due to the movement of electrons and holes, creating pairs of free electrons and holes (positively charged spaces left behind by the excited electrons) [28].

These free electrons and holes need to move through the absorber material to be extracted as electrical current. They move through a process called diffusion or migration. In perovskite materials, the electron–hole pairs (excitons) can either recombine – which can lead to a loss of electrical charge or separate into free carriers (free electrons and holes) that generate electrical current [29].

The electrons, which are the minority carriers, are extracted through the ETL to the cathode. This extraction happens because of the electrostatic force present in the depletion region of the solar cell. Once extracted, these electrons travel through the ETL of the solar cell and then through an external electric circuit. This movement of electrons generates electricity that can be used to power devices.

The holes, which are the positively charged counterparts of the electrons, move in the opposite direction to the electrons. They are extracted through the hole transport layer, which facilitates their movement towards the anode.

In simpler terms, perovskite solar cells generate electricity by first capturing the photons with a thin perovskite layer, then generating and separating free electrons and holes, and finally transporting these charges to the electrodes through selective layers that ensure efficient collection and minimal loss.

1.4 Mars Exploration

The prospect of exploration of Mars has captivated scientific communities, policymakers, and the public for decades. The allure of the Red Planet stems from a confluence of scientific curiosity, technological ambition, and the innate human desire to explore the unknown.

One of the foremost reasons for venturing to Mars is the pursuit of scientific knowledge. Mars presents an unparalleled opportunity to study the processes that have shaped not only its own geology and climate but also those of Earth. By analysing Martian soil, rocks, and atmospheric conditions, scientists hope to unravel the history of the planet and its potential to have once harboured life. Discoveries in these areas could provide critical insights into the origins and evolution of life in our solar system.

The exploration of Mars holds significant potential for advancing technology. The challenges associated with Mars missions necessitate the development of innovative technologies in aerospace, robotics, AI, and energy production. These advancements often have far-reaching applications beyond space exploration, driving innovation and economic benefits on Earth.

Furthermore, the drive to explore and potentially colonise Mars is motivated by existential concerns. Humanity faces various threats on Earth, including natural disasters and potential self-inflicted crises such as climate change and nuclear conflict. Establishing a human presence on Mars is seen as a step towards ensuring the long-term survival of our species. By creating a self-sustaining colony on Mars, humanity could protect itself from planet-wide catastrophes.

Lastly, the endeavour to reach Mars resonates deeply with the intrinsic human spirit of exploration. From the voyages of ancient mariners to the Apollo moon landings, human history is marked by a relentless quest to push beyond known boundaries. Mars represents the next frontier in this storied tradition, offering a chance to achieve feats that were once relegated to the realm of science fiction.

Mars is of interest due to several key factors. Firstly, Mars shares several Earth-like characteristics, such as similar day length and seasonal cycles, and it contains vital resources like water ice [30]. Moreover, the gravity of Mars is ~38% of Earth's, which is more favourable to human health than the microgravity experienced in space [31]. Its relative proximity to Earth makes Mars one of the more accessible planets for exploration, and we already possess the technology needed for Martian missions. Additionally, evidence suggests that Mars once had liquid water on its surface and a milder climate, indicating that it might have, and still does support microbial life [32]. Unlike the gas giants Saturn and Jupiter, Mars has a solid surface that can be landed on and explored. Furthermore, Mars contains potential resources such as water ice, which could be used for human colonisation. These factors collectively make Mars a compelling target for exploration and future human settlement.

Efforts to explore Mars using rovers present significant opportunities for utilising solar energy. The power requirements on Mars necessitate efficient photovoltaic systems to ensure a reliable energy supply, supporting everything from small robotic spacecraft like the Ingenuity helicopter to larger, more complex rovers. These systems must be designed with redundancy to support scientific instruments, communication systems, heating, and data transmission. Given the inflated costs and limited transportation capacity of Mars missions, developing lightweight and reliable energy sources is imperative. The demand for photovoltaic power on Mars, even for small robotic operations, suggests a promising market for cost-effective solar technologies.

1.5 Environmental Conditions of Mars

1.5.1 Atmosphere

The atmosphere of Mars is thin and as shown in figure 1.7 – is composed primarily of carbon dioxide (about 96%), with traces of nitrogen (1.9%) and argon (1.9%). This composition contrasts sharply with the atmosphere of Earth, which is rich in nitrogen and oxygen [33]. Additionally, the Martian atmosphere contains only trace amounts of water vapor and is known for its significant dust content, which can affect surface conditions and solar power generation, by settling on solar panels, high dust content can reduce visibility, hence affecting navigation or dust can infiltrate the machinery and electric parts causing damage and wear.

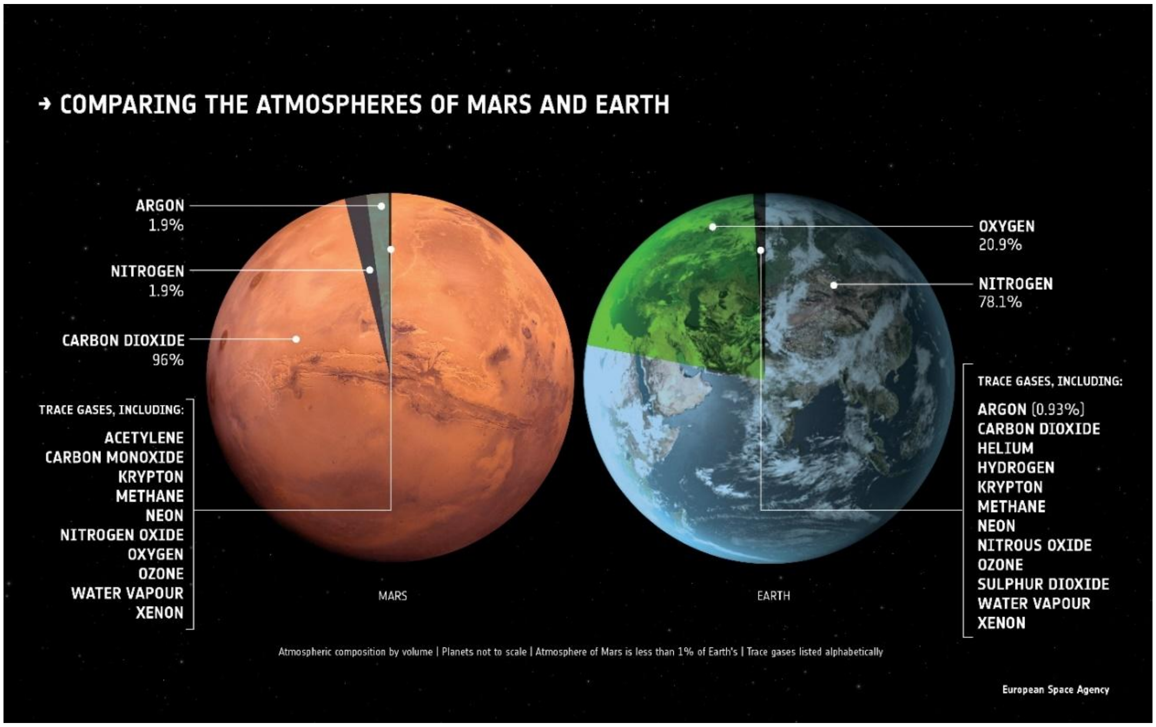

Figure 1. 7: Comparing the atmospheres of Mars and Earth [34].

1.5.2 Temperature

Temperatures on Mars can vary dramatically, ranging from -125 °C during winter at the poles to up to 20 °C in summer at the equator [35]. However, at other locations the temperatures vary less. For example, figure 1.8 shows the rise and fall of air and ground temperatures on Mars obtained by NASA's Curiosity rover at Gale Crater [36]. Ground temperatures on there can range from a high of 3 °C to a low of -91 °C, illustrating significant daily temperature fluctuations. In contrast, air temperatures vary from a high of -2 °C to a low of -75 °C – the variations in air temperatures are less extreme compared to those of the ground, due to the low thermal inertia of Martian surface (meaning it heats up and cools down quickly in response to sunlight) and due to the thin atmosphere, because it is less effective at conducting and retaining heat, leading to more rapid surface temperature changes as the ground absorbs and radiates heat more directly. The air above, being less dense, does not store as much heat and therefore changes temperature more gradually.

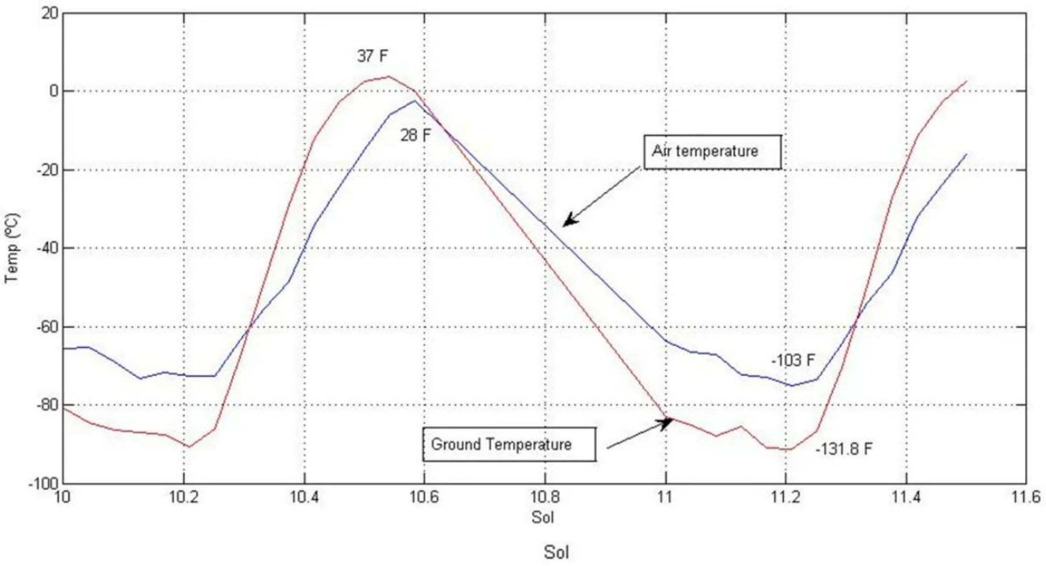

Figure 1. 8: The rise and fall of air and ground temperatures on Mars obtained by NASA's Curiosity rover at Gale Crater [36].

1.5.3 Pressure

The atmospheric pressure on Mars is approximately 0.6% of Earth's Sea level pressure (~6.1 mbar) [37].

1.5.4 Humidity

It is estimated that the average amount of water vapor on Mars is on average around 10 µm of precipitable water (pr-µm; the thickness of the water layer if all the water vapor of the atmosphere were to be condensed onto the surface, 1 pr-µm thus being 1 g of water per square meter). In comparison, the atmosphere of Earth holds several centimetres of water vapor. This highlights the extreme dryness of Mars in absolute terms. Despite this, the atmosphere can reach saturation [38].

Relative humidity sensor data from the Phoenix rover can be seen in figure 1.9 [39]. During Martian nights, when temperatures drop significantly and sunlight is absent, the thin atmosphere allows relative humidity (RH – it is relative to the temperature and pressure of the air, and it indicates how close the air is to being saturated with moisture) to reach 100%.

This occurs despite the low overall concentration of water vapor in the Martian atmosphere, typically around 0.1% [40]. This high humidity leads to the formation of frost – mostly carbon dioxide, due to the abundance of CO_2 – and sometimes water ice in regions with higher water vapor levels.

As dawn approaches and temperatures rise, the frost on Mars sublimates directly into vapor. This process is crucial because the atmosphere of Mars is so thin that liquid water cannot exist on the surface, as any liquid water would swiftly evaporate or sublimate because of the low atmospheric pressure and frigid temperatures.

During Martian daytime, temperatures increase due to sunlight. Although warmer temperatures can hold more water vapor, due to Mars' thin atmosphere, the absolute amount of water vapor remains low. Consequently, daytime relative humidity drops dramatically to below 5%. This combination of low humidity and a thin atmosphere result in extremely dry conditions on Mars. Water vapor on Mars can be moved and redistributed by atmospheric processes like winds. However, due to low gravity and thin atmosphere of Mars, some water vapor can escape into space over time – a phenomenon known as atmospheric escape. This gradual loss contributes to the overall decrease in water vapor content on Mars.

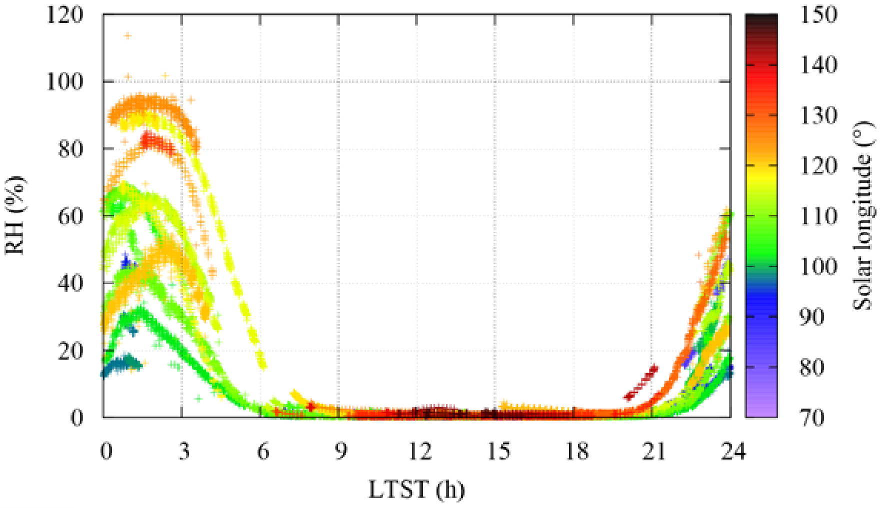

Figure 1. 9: Relative humidity measurements recorded by the Phoenix Rover at Green Valley of Vastitas Borealis, over local true solar time (LTST – it represents the time based on the position of

the Sun directly overhead at a specific location, taking into account the rotation and the local longitude of the planet) colour coded by solar longitude (L_S – a measure of the position of the planet in its orbit around the Sun relative to a reference point) as a local relative humidity.

1.5.5 Dust

Mars has lacked oceans and significant water sources for over a billion years, making it the dustiest planet in our solar system. The surface of the planet cannot sustain liquid water for prolonged periods, as mentioned earlier. This dust results from the prolonged weathering of rocks, with loose particles being continuously redistributed by the Martian winds. The lower gravity of Mars is approximately 38% of Earth’s, and its thin atmosphere, less than 1% as dense as Earth’s, allow dust to ascend to high altitudes and remain suspended for extended periods. This airborne movement causes further erosion as dust particles collide with rocks, over time – breaking them down into even finer particles.

On average, Martian dust particles measures between 1 and 4 µm in diameter, 10 times smaller than those found on Earth [41]. These dust particles significantly alter the solar spectrum at the surface of the planet, enriching it with red and infrared wavelengths while reducing blue light, compared to the AM0 spectrum. This occurs because dust particles absorb blue light and scatter red light. Consequently, the spectral composition of Martian sunlight varies with the dust concentration in the atmosphere and the path length of sunlight. As the dust level increases, or during mornings and afternoons when sunlight travels through more of the atmosphere, the light shifts more towards the red end of the spectrum [42].

The number of aerosols (tiny particles) in the atmosphere is characterised by optical depth (τ). This measurement indicates how much sunlight is absorbed or scattered by aerosols as it travels through the atmosphere. A higher optical depth means there is more tiny particles, resulting in less sunlight reaching the surface. Conversely, a lower optical depth signifies a clearer atmosphere, allowing more sunlight to penetrate through.

Mars periodically experiences extensive global dust storms that obscure planetary-scale sections for 50-100 Martian days (sols) or even more, whereas local dust storms dissipate in several sols [43]. These storms significantly increase the optical depth of the atmosphere, thereby diminishing the efficiency of solar panels. These storms are influenced by Martian seasons and occur roughly every three Martian years and can persist from several weeks to several months [44], this in turn can greatly reduce the solar irradiance at the surface (more than 90% at the equator to more than 99% at the poles) [45].

1.5.6 Radiation

On Earth, the daily dose from natural background radiation is approximately 0.0055 millisieverts (mSv). This value represents the combined radiation exposure from various natural sources, including terrestrial, cosmic, internal, and environmental radiation, that people typically experience in their everyday environment.

In comparison, the average daily dose rate of cosmic radiation on Mars is 0.67 millisieverts, which is significantly higher. This increase is primarily due to the lack of a protective atmosphere and magnetic field on Mars, allowing more galactic cosmic rays (GCRs) and solar energetic particles (SEPs) to reach the surface unimpeded [46] [47]. GCRs originate outside the solar system, likely formed by explosive events such as supernovae, while SEPs are high-energy, charged particles originating from the solar atmosphere and solar wind.
This substantial difference in radiation levels underscores the challenges posed by the Martian environment. The increased radiation impacts electronic components and materials, posing a risk to the functionality and longevity of equipment. Moreover, it presents significant health risks to humans, complicating eventual long-term exploration and habitation efforts on Mars.

1.5.7 Light Intensity

A comparative analysis of spectral irradiance per wavelength for AM1.5G and AM0 is illustrated in the figure 1.10 below, highlighting the differences in energy distribution across these spectra.

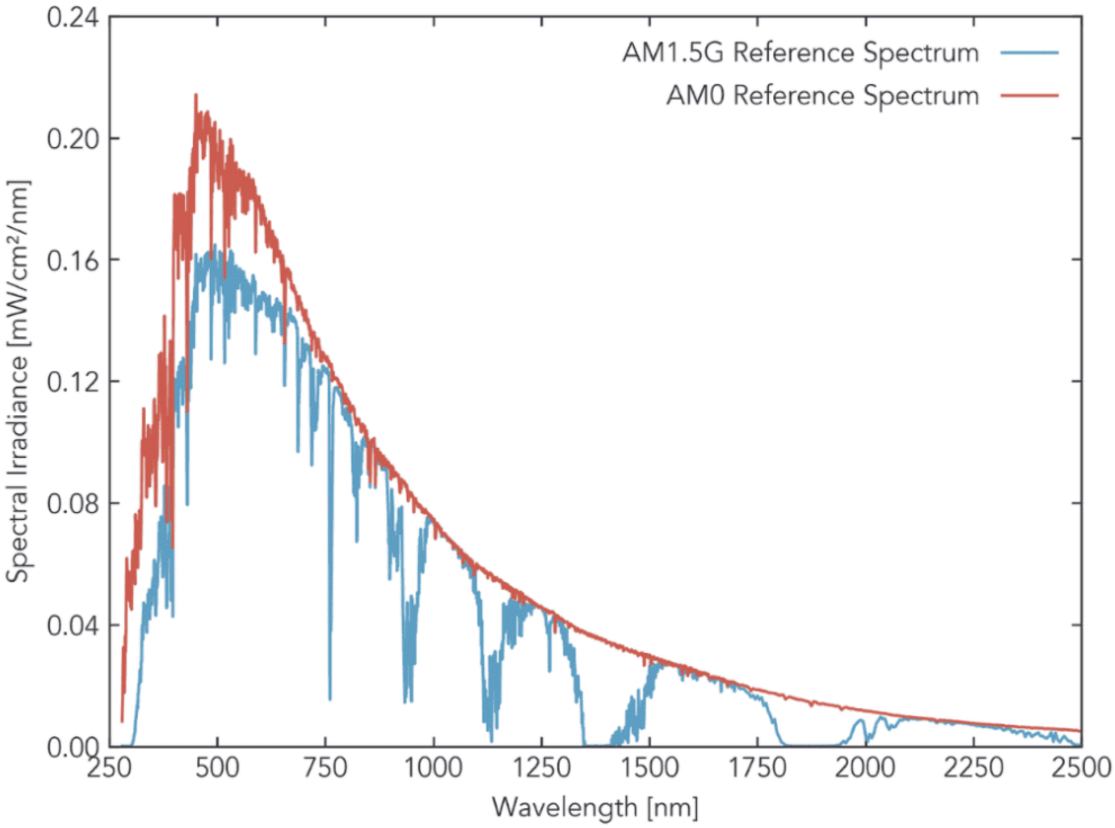

Figure 1. 10: Standard Solar Spectra for terrestrial and space use [49].

Mars orbits at an average distance of approximately 211 million kilometers from the Sun, resulting in a substantial reduction in light intensity available on its surface and in orbit. The solar irradiance on Mars is approximately 590 W/m², equivalent to only 43% of the solar irradiance measured outside Earth's atmosphere (AM0), which is 1366 W/m². This significant reduction underscores the challenges of harnessing solar energy on Mars compared to Earth [48]. The AM1.5 Global (AM1.5G) spectrum is the standard for terrestrial applications, specifically designed for flat-plate photovoltaic modules. It features an integrated light density of 1000 W/m², providing a reference for solar energy conversion efficiency under real-world conditions [49].

1.6 Energy Generation Options on Mars

1.6.1 Solar

The power requirements for Martian missions can range from watts – for small robotic spacecraft to gigawatts – for eventual human settlements in the future. Historically, Mars missions have utilised either solar or radioisotope power sources, depending on specific mission requirements. With future missions, especially crewed ones and long-term settlements, the energy demands will be more diverse and extensive.

Solar energy is a promising option for powering equipment on Mars due to its safety, lightweight nature, and feasibility for large-area placement. Currently, solar cells widely used in space missions are either silicon-based or multi-junction photovoltaic cells based on III–V semiconductor materials. These cells have demonstrated effective operation on Mars. For instance, the solar-powered Opportunity rover (fig. 1.11) operated for 15 years, far exceeding its expected lifespan [50]. Despite concerns that dust accumulation on solar panels could shorten missions, the experience with Opportunity suggests that dust accumulation is somewhat self-cleaning, allowing for effective operation using solar power alone. Self-cleaning events, including wind gusts and dust devils (a significantly weaker and smaller form of tornadoes on Earth), periodically cleared the solar panels and enabled continued operation.

However, solar power on Mars faces significant challenges. The solar irradiance on Mars is only 43% of the sunlight available outside the atmosphere of the Earth due to the planet's greater distance from the Sun. Additionally, dust storms on Mars can last for months, further reducing the efficiency of solar arrays.

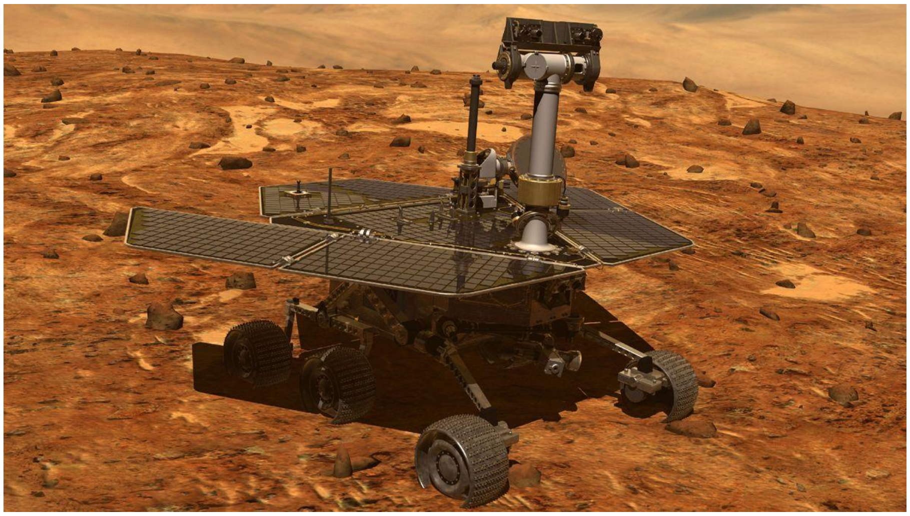

Figure 1. 11: NASA Opportunity Rover [51].

1.6.2 Nuclear

Radioisotope power sources, such as Radioisotope Thermoelectric Generators (RTGs), are known for their long lifetimes and high reliability, making them valuable for space missions. There are drawbacks, however, for instance, a 45 kg RTG, fuelled by 4.8 kilograms of plutonium-238 dioxide, generating 110 watts costs approximately 70 million US dollars [52]. Despite these drawbacks, RTGs have been successfully employed in Mars missions. A notable example is the Multi-Mission Radioisotope Thermoelectric Generator (MMRTG) used on the Perseverance rover (fig. 1.12) [53].

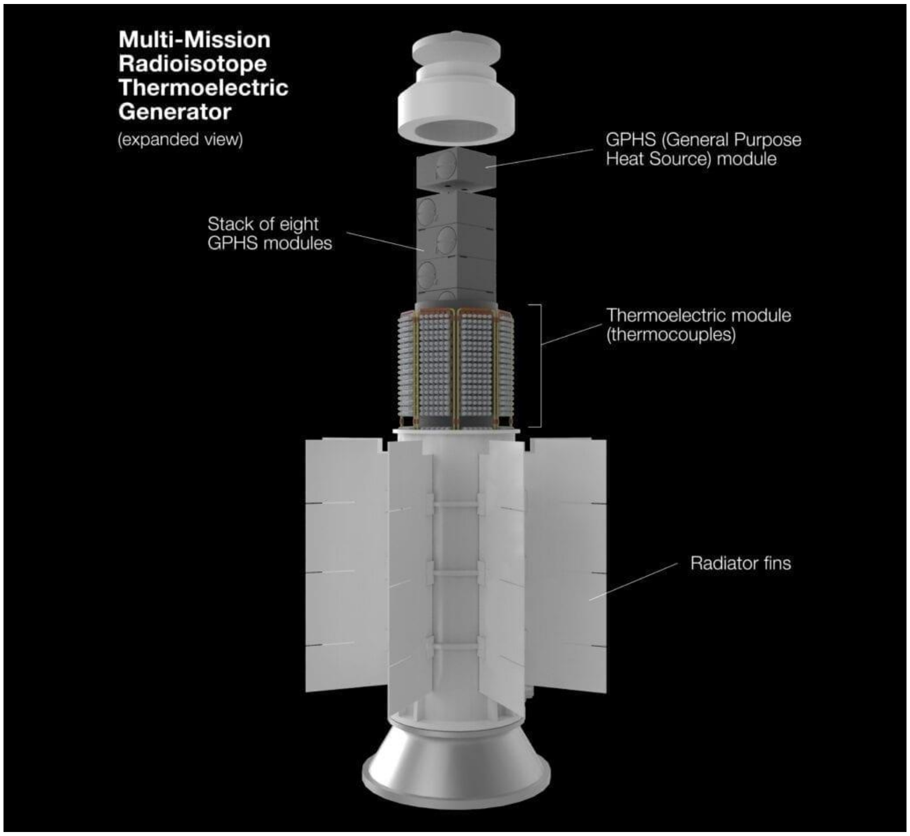

Figure 1. 12: the MMRTG used on board of the Perseverance rover [53].

RTGs operate by harnessing heat generated from the natural decay of radioisotope materials, primarily plutonium-238, to produce electricity. Each RTG comprises a heat source containing the radioisotope fuel and solid-state thermocouples that facilitate the conversion of thermal energy into electrical power. Thermocouples function by generating an electric voltage when two different conductive materials are joined in a closed circuit with junctions maintained at different temperatures. These junction pairs, known as thermoelectric couples, are crucial components in RTGs. In RTGs, the heat from the decaying radioisotope fuel heats one side of the thermocouple (the hot side), while the cold of space cools the opposite side (the cold side), thereby facilitating the generation of electricity [53]. The MMRTG on Perseverance operates by converting heat from plutonium-238 decay into electricity. Initially, it produces about 110 watts, with a gradual, predictable decline over time. Additionally, the excess heat from the MMRTG helps maintain the operational temperature of the rover. This power system also charges two lithium-ion batteries, used during peak energy demands, such as science activities, which can require up to 900 watts [54].

An MMRTG provides significant advantages over solar panels by enabling continuous operation regardless of daily or seasonal sunlight variations and preventing dust accumulation issues. This capability enhances the mobility and operational flexibility of the rover, allowing activities to be conducted day or night across various Martian latitudes and conditions. The design of the MMRTG, identical to that used by the Curiosity rover since 2011, is expected to function for at least 14 years, well beyond Perseverance’s primary mission duration of one Martian year (approximately two Earth years) [55]. However, their high production cost and limited output power pose challenges for large-scale applications.

Fission reactor, however, is one of the best options for such large-scale applications, like powering human settlements and life support systems on Mars, due to their high-power output. NASA's Project Kilopower (fig. 1.13) [56], for example, uses uranium-235, producing between one and ten kilowatts of electrical power continuously for 12-15 years. A space-rated 10 kW reactor weighs 1500 kilograms and contains 43.7 kg of uranium-235. These reactors provide a stable and continuous power source, crucial for sustaining human habitats and operations on Mars. The Kilopower system utilizes a compact uranium-235 reactor core. The fission reactor involves splitting uranium-235 atoms, releasing energy in the form of heat. The heat generated from the fission reactions is transferred through passive sodium heat pipes. Sodium is chosen for its excellent heat transfer properties. The transferred heat is then used to drive high-efficiency Stirling engines. As the gas in the Stirling engine expands and contracts, it drives a piston that generates mechanical power. This mechanical power is then converted into electricity by an attached alternator or generator. Therefore, while the technology and engineering details of Kilopower are advanced and specialized for space missions, at its core, it operates based on the fundamental principle of nuclear fission – the splitting of atoms to release energy [57].

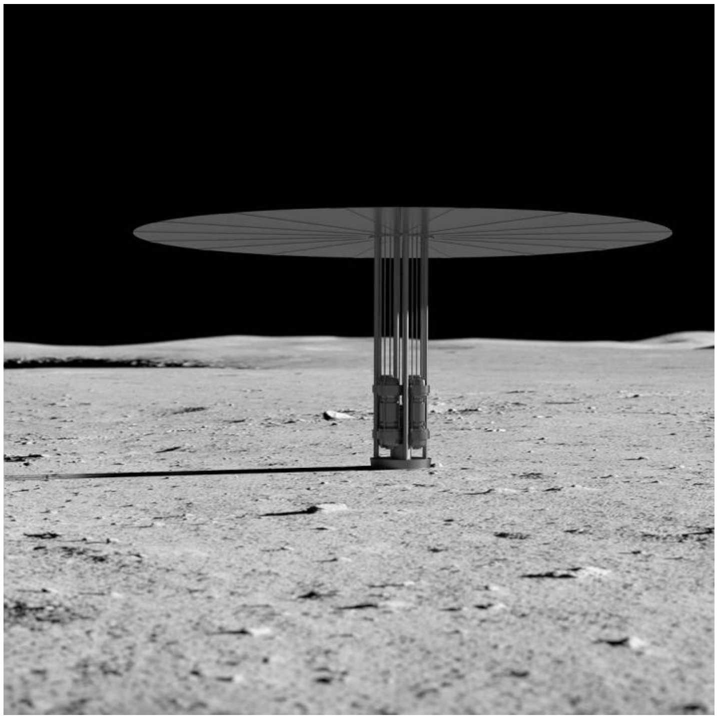

Figure 1. 13: NASA Kilopower system [56].

The advantages and disadvantages of both power sources are summarized in the table 1.1 below.

Table 1. 1: Comparison for solar and nuclear power for Martian applications

Aspect	Solar Power	Nuclear Power
Advantages	Lightweight	Continuous power supply, independent of sunlight
	Safe	Resistant to dust accumulation
	Feasible for large-area deployment	High reliability
	Relatively low cost compared to nuclear options	Ideal for small to large scale, long-term missions and equipment
	Easily scalable for larger arrays	Provides heat for maintaining operational temperatures.

Disadvantages	Dependent on sunlight availability	Very high production and material costs.

Overall, while nuclear power systems offer long lifetimes, flexible power output, and high reliability, which make them suitable for both small and large-scale applications on Mars, their high costs and the complexity of obtaining and refining fissionable materials such as plutonium and uranium make them viable only for flagship missions. In contrast, solar cells are preferred for Martian applications due to their lightweight nature, safety, simpler production process compared to nuclear options, and suitability for both small and large-scale installations [52].

1.7 Site Selection

1.7.1 Requirements

Selecting an appropriate landing site on Mars is a critical and multifaceted decision that has profound implications for the success of exploration missions. The choice of landing site is influenced by scientific objectives, safety considerations, and the potential for future human habitation.

The primary objective of selecting a landing site on Mars is to maximize scientific return. Mars presents a diverse geological landscape, with features such as ancient river valleys, lake beds, and volcanic regions offering invaluable insights into the history of the planet. Sites like Gale Crater, explored by the Curiosity rover, have been chosen for their potential to reveal past environmental conditions that might have supported microbial life. Similarly, Jezero Crater, targeted by the Perseverance rover, was selected for its ancient river delta, believed to contain well-preserved biosignatures and organic molecule. These sites are not only scientifically rich but also strategically located to advance our understanding of Mars' geological and climatic evolution. Sites of other Martian missions and sites of interest are illustrated in figure 1.14.

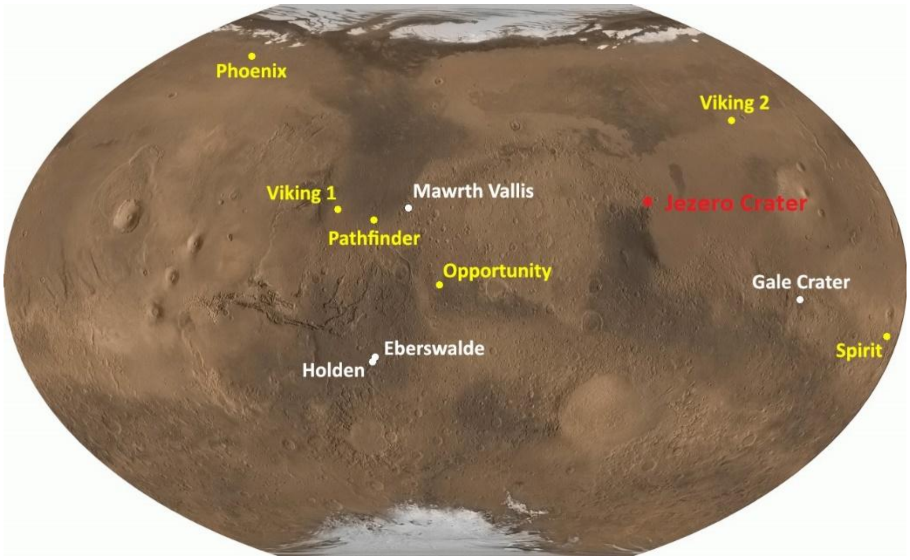

Figure 1. 14: Red marks the location of Jezero Crater on the surface of Mars relative to the location of other missions (yellow) and sites of interest (white) [58].

The chosen site must have smooth terrain to minimize landing risks and avoid hazards such as large boulders, steep slopes, or dust storms. Additionally, the site must be accessible, with favourable conditions for communication with Earth and for the operation of solar cells.

Furthermore, the selection of landing sites is influenced by the potential for future human exploration and habitation. Regions with access to essential resources, such as water ice, are prioritised as they are crucial for sustaining human life and supporting long-term missions. The presence of subsurface ice deposits, particularly in mid-latitude regions, offers a promising solution for in-situ resource utilisation. These ice deposits can be heated to produce drinking water, while it has been shown that electrolysis of Martian brines at the average Martian ambient temperature (237 K) can generate hydrogen fuel and oxygen for life support [59].

The selection process involved a thorough evaluation of over 60 potential sites by an international team of scientists over five years. Each site was scrutinized for its scientific value and suitability for safe landing and operations. Jezero stood out due to its diverse and well-preserved geological history [60].

1.7.2 Jezero Crater

Jezero Crater is in the Isidis Planitia region, which was significantly altered by an ancient meteorite impact, creating a large crater about 1200 kilometres across. Within this basin, a subsequent smaller impact formed Jezero Crater, as shown in figure 1.15 below [61].

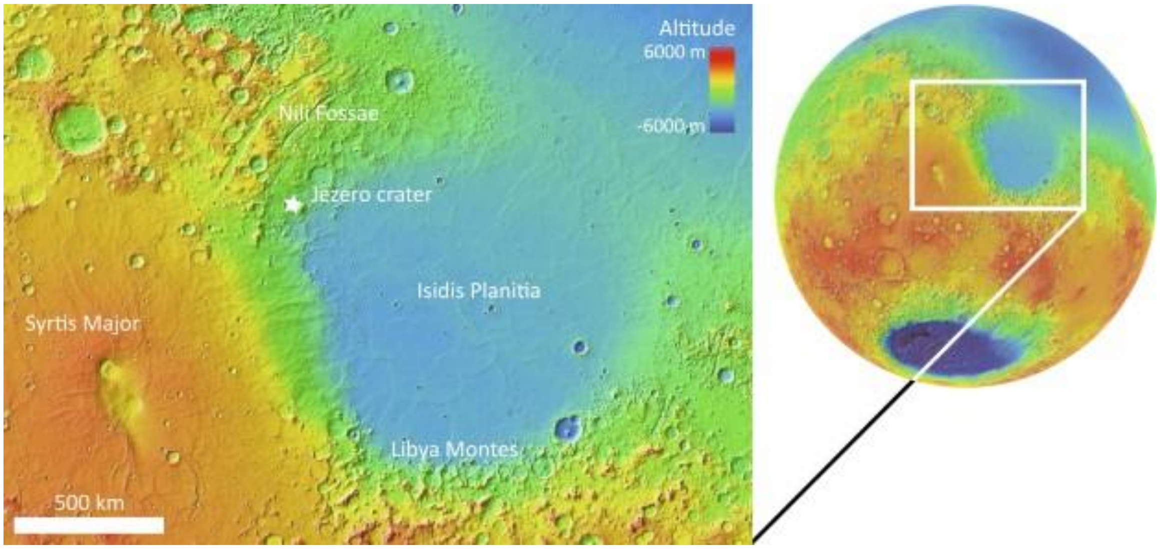

Figure 1. 15: This topographical map depicts the Nili Fossae region on Mars, which includes the landing site of NASA Perseverance Rover landing site: Jezero Crater (marked with a white star). The map provides a broader view of the Martian surface context on the right side of the frame. Distinct colours indicate varying surface altitudes, ranging from lower blues and greens to higher oranges and reds [62].

Scientists believe that Jezero Crater once housed an ancient lake, as indicated by the presence of a dried-up river delta. This area likely had a low salinity environment [63], making it potentially habitable in the past [64]. The proximity of the site to the Martian equator ensures higher temperatures compared to the planet's poles [65], and its low elevation suggests a consistent water supply with minimal evaporation. Additionally, The Nili Fossae region is thought to be one of the locations on Mars with the largest diversity and most extensive exposures of alteration minerals [63] [66].

One of the practical advantages of Jezero Crater is its low dust levels, which reduce risks to the rover and its instruments. The flat terrain of the crater is ideal for both landing and the development of future infrastructure, facilitating easier transportation and construction. The minimal impact of asteroid collisions in this region also makes it a safer choice for a long-term mission [67].

Overall, Jezero Crater offers a promising opportunity to explore Mars' ancient climate and geology, potentially uncovering signs of past life and advancing our understanding of the history of the planet. Therefore, this site was selected not only for its scientific potential but also for its practical advantages in ensuring a successful mission.

1.7.3 Temperature at Jezero Crater

Figure 1.16 below displays the temperatures at Jezero Crater measured by the Perseverance Rover over the course of a Martian day (sol), which can be categorized into four distinct regimes.

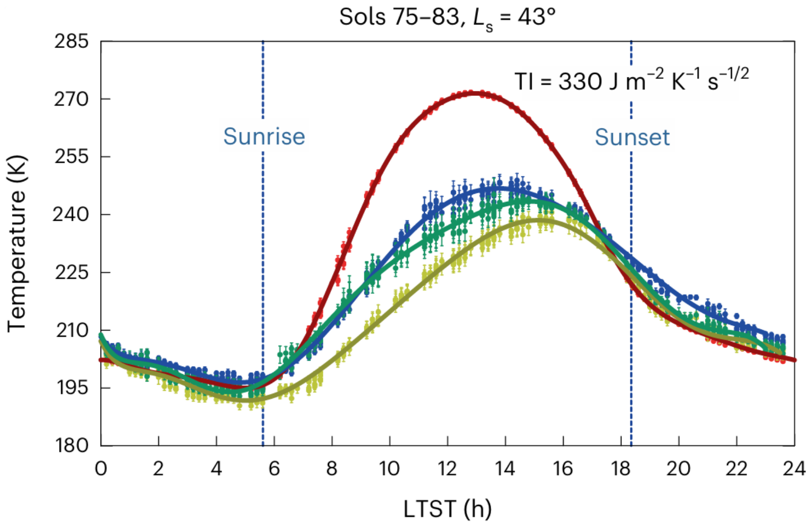

Figure 1. 16: Temperature at the surface (Tsurf = red), at z = 0.85 m (blue), z = 1.45 m (green) and z ≈ 40 m (green, yellow). LTST stands for Local True Solar Time.

First, during the daytime, the Martian surface absorbs sunlight, heating up rapidly due to its low thermal inertia. This leads to convection, where warm air rises and cooler air sinks.

The temperature difference between the surface and higher altitudes can be pronounced during this period (270 K at the surface, only 245 K 0.85 m above).

Secondly, as the Sun sets, the surface begins to cool down. The convective boundary layer, where the upward movement of warm air stops and begins to transition into a stable atmosphere, collapses during this period. Temperatures at different heights start to equalize.

Thirdly, after sunset, Mars experiences a prolonged period of cooling. The surface continues to lose heat, and the atmosphere above becomes more stable. Temperatures at the surface and at different heights tend to decrease steadily during this regime.
Fourthly, before sunrise, the temperature falls to approximately 195 K. The inversion layer, where temperature increases with height, begins to fade as the energy of the Sun starts to reach the surface again. The convective boundary layer begins to develop once more, with warm air rising from the surface. This transition period marks the end of the stable night-time regime and the beginning of daytime convection [68].

1.7.3 Humidity at Jezero Crater

The humidity profile of Jezero Crater during sols 80-250 recorded by the Perseverance Rover is shown in figure 1.17. Humidity change is small in Jezero, it varies from 0% to 30% RH. The highest relative humidity values are in the midnight-pre-dawn period [68].

The low relative humidity could be pointed to several reasons. At night, cooler and drier air moves into the crater. Mars has a very thin and dry atmosphere, so when temperatures drop after sunset, the air near the surface cannot hold much water vapor. This causes any moisture in the air to condense or freeze, resulting in lower humidity levels.

Another factor is that the thin atmosphere of Mars allows water vapor near the surface to escape into the ground or subsurface. Mars has ice and frost patches beneath the surface, and at night, some of the water vapor near the surface may seep downward, further reducing the humidity in the immediate atmosphere.

These processes – cooling air at night and potential water loss to the subsurface – contribute to the consistently low relative humidity observed not only in Jezero Crater but also in other parts of Mars. The unique atmospheric conditions and geological features of the planet play a significant role in shaping these humidity levels [69].

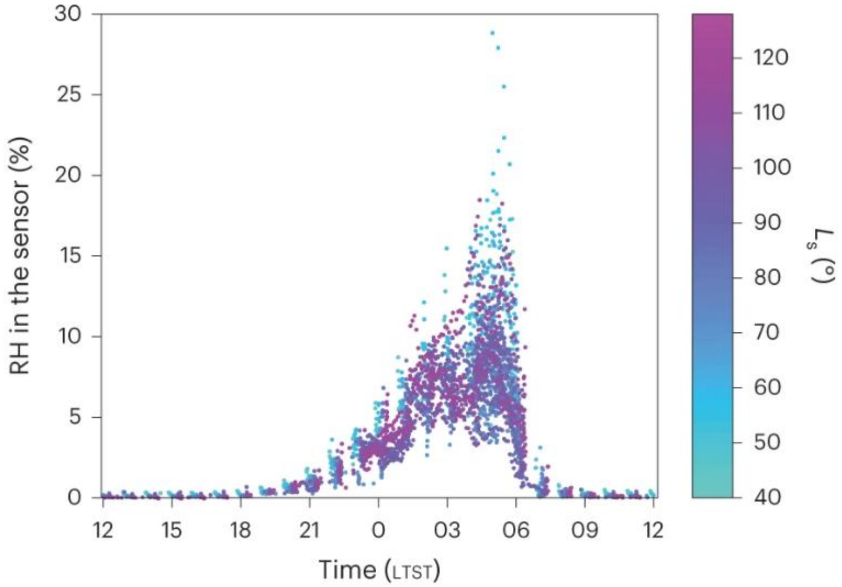

Figure 1. 17: Daily and seasonal evolution of RH in Jezero Crater, during sols 80–250 (Solar longitude of 44–122°).

1.7.4 Optical Depth at Jezero Crater

As mentioned earlier, the number of aerosols (tiny particles) in the atmosphere is characterised by optical depth.

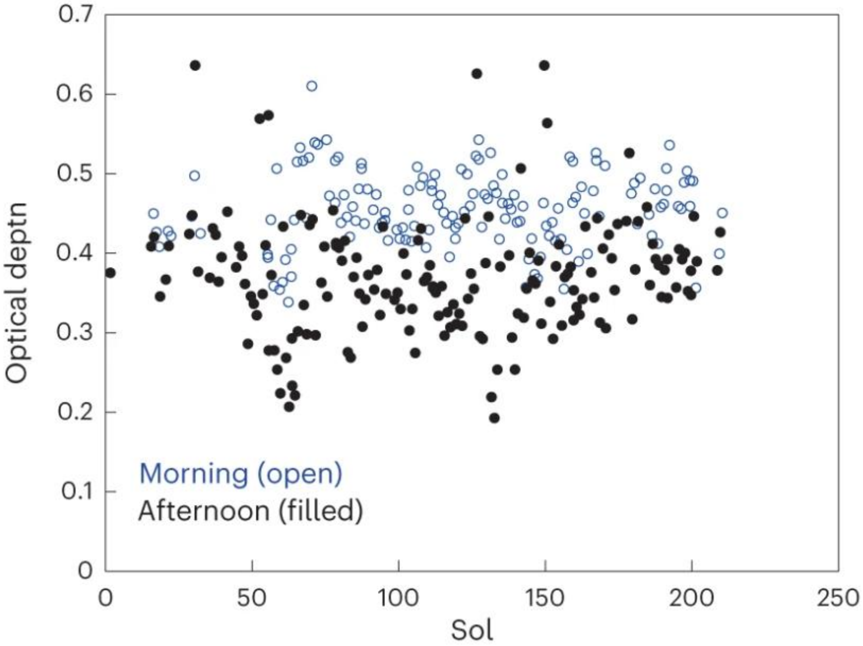

Figure 1. 18: Optical depth at Jezero Crater. Values are observed to be higher in the morning (open symbols) than in the afternoon (filled symbols).

As illustrated in figure 1.18, the optical depth data collection began near the start of Mars' aphelion season, when the planet is farthest from the Sun in its elliptical orbit. This period typically brings cooler temperatures and an increased presence of water-ice clouds. Throughout this time, morning measurements consistently exhibited higher atmospheric opacity ($\tau = 0.5$) compared to the afternoon ($\tau = 0.4$), with the maximum opacity observed between 05:00 and 09:00, and the minimum around 16:00 [70]. The observed morning-to-afternoon variations are likely driven by fluctuations in water-ice cloud cover, which overlay a relatively stable baseline of atmospheric dust. While a clear seasonal trend is present, significant day-to-day variability also occurs, most likely due to changes in the water-ice clouds. During this period, particle sizes observed by the Perseverance Rover instruments ranged between ~1.2 and 1.4 μm [68].

References

1. U.S. Department of Energy. Solar Power Technologies Office: Solar Photovoltaic Research and Development: A Historical Timeline. [Internet]. Available from: https://www1.eere.energy.gov/solar/pdfs/solar_timeline.pdf.

2. Durmaz Z, Husein S, Saive R. Thin silicon interference solar cells for targeted or broadband wavelength absorption enhancement. Optics express. 2021 Feb 1;29(3):4324-37
3. Friedrich J, von Ammon W, Müller G. Czochralski growth of silicon crystals. InHandbook of Crystal Growth 2015 Jan 1 (pp. 45-104). Elsevier
4. Bhattacharya S, John S. Beyond 30% conversion efficiency in silicon solar cells: a numerical demonstration. Scientific reports. 2019 Aug 28;9(1):12482
5. Flood DJ. Space photovoltaics–history, progress and promise. Modern Physics Letters B. 2001 Aug 20;15(17n19):561-70
6. Li J, Aierken A, Liu Y, Zhuang Y, Yang X, Mo JH, Fan RK, Chen QY, Zhang SY, Huang YM, Zhang Q. A brief review of high efficiency III-V solar cells for space application. Frontiers in Physics. 2021 Feb 2;8:631925
7. Verduci R, Romano V, Brunetti G, Yaghoobi Nia N, Di Carlo A, D'Angelo G, Ciminelli C. Solar energy in space applications: review and technology perspectives. Advanced Energy Materials. 2022 Aug;12(29):2200125
8. American Chemical Society. Perovskite. Molecule of the Week Archive. [Internet]. Available from: https://www.acs.org/molecule-of-the-week/archive/p/perovskite.html#:~:text=The%20mineral%20occurs%20as%20orthorhombic,mineralogist%20and%20nobleman%20Lev%20Perovski.
9. Yu Y, Xia J, Liang Y. Basic understanding of perovskite solar cells and passivation mechanism. AIP Advances. 2022 May 1;12(5)
10. Okinawa Institute of Science and Technology. Perovskite crystal structure. [Internet] Available from: https://www.oist.jp/image/perovskite-crystal-structure
11. National Renewable Energy Laboratory (NREL). Interactive Solar Cell Efficiency Chart. [Internet]. Available from: https://www.nrel.gov/pv/interactive-cell-efficiency.html.
12. Zhang W, Eperon GE, Snaith HJ. Metal halide perovskites for energy applications. Nature Energy. 2016 May 9;1(6):1-8
13. Kojima A, Teshima K, Shirai Y, Miyasaka T. Organometal halide perovskites as visible-light sensitizers for photovoltaic cells. Journal of the american chemical society. 2009 May 6;131(17):6050-1
14. Ossila. Perovskites and Perovskite Solar Cells: An Introduction. [Internet]. Available from: https://www.ossila.com/pages/perovskites-and-perovskite-solar-cells-an-introduction.
15. Hu Y, Niu T, Liu Y, Zhou Y, Xia Y, Ran C, Wu Z, Song L, Müller-Buschbaum P, Chen Y, Huang W. Flexible perovskite solar cells with high power-per-weight: progress, application, and perspectives. ACS Energy Letters. 2021 Jul 29;6(8):2917-43
16. Kaltenbrunner M, Adam G, Głowacki ED, Drack M, Schwödiauer R, Leonat L, Apaydin DH, Groiss H, Scharber MC, White MS, Sariciftci NS. Flexible high power-per-weight perovskite solar cells with chromium oxide–metal contacts for improved stability in air. Nature materials. 2015 Oct;14(10):1032-9
17. Miyazawa Y, Ikegami M, Chen HW, Ohshima T, Imaizumi M, Hirose K, Miyasaka T. Tolerance of perovskite solar cell to high-energy particle irradiations in space environment. IScience. 2018 Apr 27;2:148-55

18. Li W, Zhang W, Van Reenen S, Sutton RJ, Fan J, Haghighirad AA, Johnston MB, Wang L, Snaith HJ. Enhanced UV-light stability of planar heterojunction perovskite solar cells with caesium bromide interface modification. Energy & Environmental Science. 2016;9(2):490-8
19. Yang K, Huang K, Li X, Zheng S, Hou P, Wang J, Guo H, Song H, Li B, Li H, Liu B. Radiation tolerance of perovskite solar cells under gamma ray. Organic Electronics. 2019 Aug 1;71:79-84
20. Huan Z, Zheng Y, Wang K, Shen Z, Ni W, Zu J, Shao Y. Advancements in radiation resistance and reinforcement strategies of perovskite solar cells in space applications. Journal of Materials Chemistry A. 2024;12(4):1910-22
21. Miah MH, Khandaker MU, Rahman MB, Nur-E-Alam M, Islam MA. Band gap tuning of perovskite solar cells for enhancing the efficiency and stability: issues and prospects. RSC advances. 2024;14(23):15876-906
22. Beynon D, Parvazian E, Watson T, Hooper K, McGettrick J, Patidar R, Dunlop T, Wei Z, Davies P, Garcia-Rodriguez R, Carnie M, Davies M. All-printed roll-to-roll perovskite photovoltaics enabled by solution-processed carbon electrode. Advanced Materials. 2023 Apr;35(16):2208561
23. Chen W, Yin X, Que M, Xie H, Liu J, Yang C, Guo Y, Wu Y, Que W. A comparative study of planar and mesoporous perovskite solar cells with printable carbon electrodes. Journal of Power Sources. 2019 Feb 1;412:118-24
24. Zhao Y, Nardes AM, Zhu K. Mesoporous perovskite solar cells: material composition, charge-carrier dynamics, and device characteristics. Faraday discussions. 2014;176:301-12
25. Qiu C, Wu Y, Song J, Wang W, Li Z. Efficient planar perovskite solar cells with ZnO electron transport layer. Coatings. 2022 Dec 17;12(12):1981
26. Sherkar T. Device physics of hybrid perovskite solar cells. University of Groningen, 2018
27. Sala J, Heydarian M, Lammar S, Abdulraheem Y, Aernouts T, Hadipour A, Poortmans J. Compositional investigation for bandgap engineering of wide bandgap triple cation perovskite. ACS Applied Energy Materials. 2021 Jul 9;4(7):6377-84
28. Vasilopoulou M, Mohd Yusoff AR, Nazeeruddin MK. Background and Basic Knowledge of Perovskite Solar Cells. Printable Mesoscopic Perovskite Solar Cells. 2023 Aug 28:1-8
29. Hsiao YC, Wu T, Li M, Liu Q, Qin W, Hu B. Fundamental physics behind high-efficiency organo-metal halide perovskite solar cells. Journal of Materials Chemistry A. 2015;3(30):15372-85
30. Nazari-Sharabian M, Aghababaei M, Karakouzian M, Karami M. Water on Mars—a literature review. Galaxies. 2020 May 9;8(2):40
31. Levchenko I, Xu S, Mazouffre S, Keidar M, Bazaka K. Mars colonization: beyond getting there. Terraforming Mars. 2021 Nov 23:73-98
32. Joseph RG, Dass RS, Rizzo V, Cantasano N, Bianciardi G. Evidence of life on Mars. Journal of Astrobiology and Space Science Reviews. 2019;1:40-81
33. Mahaffy PR, Webster CR, Atreya SK, Franz H, Wong M, Conrad PG, Harpold D, Jones JJ, Leshin LA, Manning H, Owen T. Abundance and isotopic composition of

gases in the Martian atmosphere from the Curiosity rover. Science. 2013 Jul 19;341(6143):263-6

34. European Space Agency. Comparing the atmospheres of Mars and Earth [Internet]. Available from: https://www.esa.int/ESA_Multimedia/Images/2018/04/Comparing_the_atmospheres_of_Mars_and_Earth
35. Space.com. What is the temperature of Mars? [Internet]. Available from: https://www.space.com/16907-what-is-the-temperature-of-mars.html
36. NASA Science. Taking Mars' Temperature. Washington, D.C.: National Aeronautics and Space Administration; 2021. [Internet]. Available from: https://science.nasa.gov/resource/taking-mars-temperature/
37. Mischna MA, Piqueux S. The role of atmospheric pressure on Mars surface properties and early Mars climate modeling. Icarus. 2020 May 15;342:113496
38. Harri AM, Genzer M, Kemppinen O, Gomez-Elvira J, Haberle R, Polkko J, Savijärvi H, Rennó N, Rodriguez-Manfredi JA, Schmidt W, Richardson M. Mars Science Laboratory relative humidity observations: Initial results. Journal of Geophysical Research: Planets. 2014 Sep;119(9):2132-47
39. Fischer E, Martínez GM, Rennó NO, Tamppari LK, Zent AP. Relative humidity on Mars: new results from the Phoenix TECP sensor. Journal of Geophysical Research: Planets. 2019 Nov;124(11):2780-92
40. Moroz VI. Chemical composition of the atmosphere of Mars. Advances in Space Research. 1998 Jan 1;22(3):449-57
41. Ho C, Gloshan N, Kliore A. Martian Dust Storms and Their Effects on Propagation. Radio Wave Propagation for Communication on and around Mars. 1999:59-71
42. Landis GA. Solar cell selection for Mars. IEEE Aerospace and Electronic Systems Magazine. 2000 Jan;15(1):17-21
43. Appelbaum J, Landis GA, Sherman I. Solar radiation on Mars—update 1991. Solar Energy. 1993 Jan 1;50(1):35-51
44. Power and Resources. Solar Power is Challenging on Mars [Internet]. Available from: https://www.powerandresources.com/blog/solar-power-is-challenging-on-mars
45. Levine JS, Kraemer DR, Kuhn WR. Solar radiation incident on Mars and the outer planets: Latitudinal, seasonal, and atmospheric effects. Icarus. 1977 May 1;31(1):136-45
46. Hong Kong Observatory. Journey to Mars and Cosmic Radiation [Internet]. Available from: https://www.hko.gov.hk/en/education/space-weather/effects-of-space-weather/00703-Journey-to-Mars-and-Cosmic-Radiation.html
47. Ehresmann B, Hassler DM, Zeitlin C, Guo J, Wimmer-Schweingruber RF, Matthiä D, Lohf H, Burmeister S, Rafkin SC, Berger T, Reitz G. Energetic particle radiation environment observed by RAD on the surface of Mars during the September 2017 event. Geophysical Research Letters. 2018 Jun 16;45(11):5305-11
48. Baraskar A, Yoshimura Y, Nagasaki S, Hanada T. Space solar power satellite for the Moon and Mars mission. Journal of Space Safety Engineering. 2022 Mar 1;9(1):96-105
49. G2V. AM0: What is the Air Mass 0 Spectrum? [Internet]. Available from: https://g2voptics.com/solar-simulation/am0-spectrum/

50. NASA Science. Opportunity [Internet]. NASA. Available from: https://science.nasa.gov/mission/mer-opportunity/
51. Space.com. Opportunity Rover: NASA's Longest Mars Mission. [Internet]. Available from: https://www.space.com/18289-opportunity-rover.html
52. Sun M, Zheng Y, Shi Y, Zhang G, Shao Y. Low-intensity–low-temperature stability assessment of perovskite solar cells operating on simulated Martian surface conditions. Physical Chemistry Chemical Physics. 2022;24(29):17716-22
53. NASA. Mars Internal Resource 788 [Internet]. Available from: https://mars.nasa.gov/internal_resources/788/
54. NASA Jet Propulsion Laboratory. Mars 2020 Mission: Power. [Internet]. Available from: https://www.jpl.nasa.gov/news/press_kits/mars_2020/launch/mission/spacecraft/power/
55. Power Magazine. The Nuclear Battery Aboard Perseverance: The Next-Gen Mars Rover. [Internet]. Available from: https://www.powermag.com/the-nuclear-battery-aboard-perseverance-the-next-gen-mars-rover/
56. NASA. Kilopower: NASA's Nuclear Power Plant for Mars [Internet]. Available from: https://www.nasa.gov/directorates/spacetech/kilopower
57. NASA. Powering Up NASA's Human Reach for the Red Planet. [Internet]. Available from: https://www.nasa.gov/directorates/stmd/game-changing-development-program/powering-up-nasas-human-reach-for-the-red-planet/
58. Sky & Telescope. Jezero Crater Selected as Landing Site for Mars 2020 Rover. [Internet]. Available from: https://skyandtelescope.org/astronomy-news/jezero-crater-selected-as-landing-site-for-mars-2020-rover/.
59. Shahid M, Chambers B, Sankarasubramanian S. Methane and oxygen from energy-efficient, low temperature in situ resource utilization enables missions to Mars. AIChE Journal. 2023 May;69(5):e18010
60. NASA Science. Mars 2020 Perseverance Rover Science Goals. [Internet]. Available from: https://science.nasa.gov/mission/mars-2020-perseverance/science/.
61. NASA Science. Jezero Crater: Mars 2020 Rover Landing Site. [Internet]. Available from: https://science.nasa.gov/resource/jezero-crater-mars-2020-rover-landing-site/.
62. European Space Agency. The Topography of Nili Fossae. Paris: European Space Agency; 2022. [Internet]. Available from: https://sci.esa.int/web/mars-express/-/the-topography-of-nili-fossae
63. Wiens RC, Udry A, Beyssac O, Quantin-Nataf C, Mangold N, Cousin A, Mandon L, Bosak T, Forni O, Mclennan SM, Sautter V. Compositionally and density stratified igneous terrain in Jezero crater, Mars. Science advances. 2022 Aug 25;8(34):eabo3399
64. Mangold N, Gupta S, Gasnault O, Dromart G, Tarnas JD, Sholes SF, Horgan B, Quantin-Nataf C, Brown AJ, Le Mouélic S, Yingst RA. Perseverance rover reveals an ancient delta-lake system and flood deposits at Jezero crater, Mars. Science. 2021 Nov 5;374(6568):711-7
65. Mellon MT, Sizemore HG. The history of ground ice at Jezero Crater Mars and other past, present, and future landing sites. Icarus. 2022 Jan 1;371:114667

66. Goudge TA, Mustard JF, Head JW, Fassett CI, Wiseman SM. Assessing the mineralogy of the watershed and fan deposits of the Jezero crater paleolake system, Mars. Journal of Geophysical Research: Planets. 2015 Apr;120(4):775-808
67. Lagain A, Benedix GK, Servis K, Baratoux D, Doucet LS, Rajšic A, Devillepoix HA, Bland PA, Towner MC, Sansom EK, Miljković K. The Tharsis mantle source of depleted shergottites revealed by 90 million impact craters. Nature Communications. 2021 Nov 3;12(1):6352
68. Rodriguez-Manfredi JA, De la Torre Juárez M, Sanchez-Lavega A, Hueso R, Martínez G, Lemmon MT, Newman CE, Munguira A, Hieta M, Tamppari LK, Polkko J. The diverse meteorology of Jezero crater over the first 250 sols of Perseverance on Mars. Nature Geoscience. 2023 Jan;16(1):19-28.
69. Tamppari LK, Martinez G, Manfredi JA, de la Torre-Juárez M, Hieta M, Polkko J, Jaakonaho I, Genzer M, Harri AM, Mcconnochie TH, Montmessin F. Relative humidity and vapor amount at Jezero Crater. InSeventh International Workshop on the Mars Atmosphere: Modelling and Observations 2022.
70. Smith MD, Martínez GM, Sebastián E, Lemmon MT, Wolff MJ, Apéstigue V, Arruego I, Toledo D, Viúdez-Moreiras D, Rodriguez-Manfredi JA, Juarez MD. Diurnal and seasonal variations of aerosol optical depth observed by MEDA/TIRS at Jezero Crater, Mars. Journal of Geophysical Research: Planets. 2023 Jan;128(1):e2022JE007560

Chapter 2: Experimental Methods

This chapter provides a detailed account of the methodologies for sample preparation and the experimental procedures employed to assess solution-processable solar cells under simulated Martian conditions. It outlines the comprehensive protocols for the fabrication of both methylammonium lead iodide ($MAPbI_3$) and triple cation ($Cs_{0.05}(MA_{0.17}FA_{0.83})_{0.95}Pb(I_{0.17}Br_{0.13})_3$) perovskite devices. Additionally, the chapter offers a thorough overview of the characterization techniques utilized and the experiments conducted to evaluate the performance and stability of these perovskite solar cells in an environment that mimics Martian conditions.

2.1 Perovskite Solar Cell Fabrication

In this study, conventional planar perovskite cells (illustrated in Figure 2.1) were fabricated entirely at low temperatures (<150 °C). These cells comprised five smaller pixels, each with an active area of 0.15 cm², and one larger pixel with an active area of 1 cm².

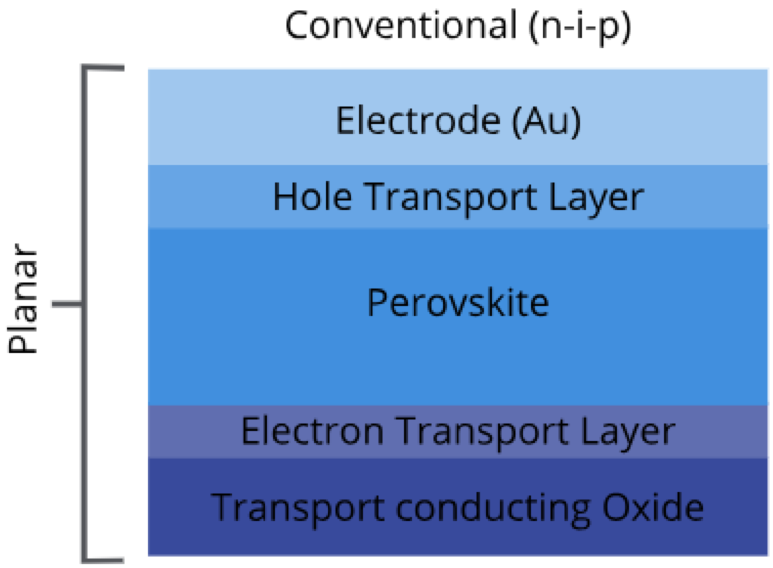

Figure 2. 1: conventional planar structure of a perovskite device. N-i-p stands for n-type layer (ETL), intrinsic layer (perovskite absorber layer), p-type layer (HTL).

SnO_2 nanoparticles were used as an electron transport layer (ETL) instead of TiO_2 as they can be printed and dried at low temperature and were shown to be more transparent and resistant to UV radiations as compared to the TiO_2 ETLs [1]. Additional advantages of SnO_2 include – high electron mobility and good energy-level alignment with perovskite and electrodes [2]. Creating an effective device is complex and requires considerable craftsmanship, with the outcome being influenced by several environmental factors that are currently not well understood and difficult to regulate. These variables contribute to the observed cell-to-cell and batch-to-batch variations reported by many research groups in the field. Additionally, there is a noticeable dependence on the individual constructing the cells, with more skilled experts producing significantly superior cells using identical starting materials. It is important to note that the solar cells measured in this study were not created by an expert with the highest level of craftsmanship, and thus were not record-setting devices.

2.1.1 General ITO/Glass Cleaning

15 Ω^{-1} ITO/glass substrates (Lumtec) were sequentially sonicated in 2% hellmanex and de-ionised water solution, de-ionised water, acetone, and isopropyl alcohol for 5 minutes each, in an ultrasonic bath. The substrates were then blown dry via nitrogen stream and placed into an oxygen plasma cleaner at 50% power for 10 minutes to remove any residual organic compounds after general ITO/glass cleaning. After that, the substrates were UV ozone treated for 20 minutes to remove any residual carbon contaminants and to make the surfaces more hydrophilic.

2.1.2 Electron Transport Layer Fabrication and Deposition

SnO_2 nanoparticles (15% colloidal dispersion in H_2O, Alfa Aesar) were diluted in deionized water in a 1:6.5 (V:V) volume ratio. This solution was deposited onto the ITO/glass via spin coating at a spin speed of 3000 rpm and an acceleration of 3000 rpm for 30 s. This was followed by thermal annealing of the SnO_2/ITO/glass at 150 °C for 30 min. This drying step improves the film quality by enhancing the crystallinity and uniformity of the SnO_2 film. Additionally, it also helps remove any residual solvent, promotes favourable interface formation, and optimizes the optoelectronic properties of the SnO_2 layer. The final thickness of the SnO_2 film is ~25 nm.

2.1.3 Methylammonium Lead Iodide Layer Fabrication and Deposition

$MAPbI_3$ perovskite films were deposited in a nitrogen glovebox (<30 ppm O_2, <0.1 ppm H_2O) to shield the film from oxygen, moisture and other contaminants, using a single-step deposition method from the precursor solution containing MAI (199 mg) and PbI_2 (605 mg), in anhydrous N, N dimethylformamide (DMF) (99.8%, Sigma-Aldrich)/dimethyl sulfoxide (DMSO) (99.7%, Sigma-Aldrich) (8:2 (V:V)). DMF and DMSO were used for their ability to dissolve the precursor materials, by combining these solvents in a specific ratio, the solubility of all components in the solution is optimized, ensuring that each component can dissolve adequately and uniformly mix. These precursors were weighed into a glass vial and then heated up to 60 °C with a magnetic stirrer bar to promote adequate mixing. The solution was then filtered using a 0.2 µm PTFE filter to remove particulate contaminants from the precursor solution which can negatively impact the quality and uniformity of the perovskite film by causing defects or uneven distribution of materials. The filtered $MAPbI_3$ solution was deposited onto the planar SnO_2 films by spin coating at 4000 rpm for 30 s and 300 mL of chlorobenzene (99.9%) antisolvent was dropped on the spinning substrate 15 s prior to the end of the program to promote crystallisation. This was followed by annealing the films at 100 °C for 10 minutes to evaporate away any residual solvent and improve the crystallinity of the film, forming a ~450 nm thick methylammonium lead iodide layer.

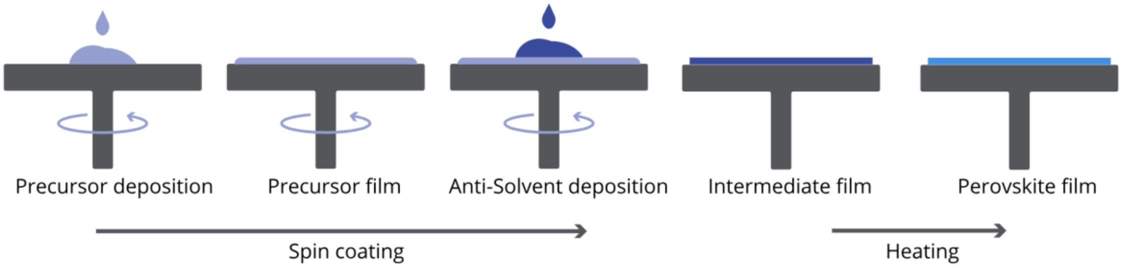

Figure 2. 2 simplified illustration of perovskite spin coating and thermal annealing process [3].

2.1.4 Triple Cation Layer Fabrication and Deposition

Just like $MAPbI_3$, triple cation perovskite films were deposited in a nitrogen glovebox (<30 ppm O_2, <0.1 ppm H_2O) using a single-step deposition method from the precursor solution containing FAI (172 mg) (dyesol), PbI_2 (507 mg) (TCI), MABr (22 mg) (dyesol) and $PbBr_2$ (73 mg) (TCI) in anhydrous N,N-dimethylformamide (99.8%, Sigma-Aldrich)/dimethyl sulfoxide (99.7%, Sigma-Aldrich) (8:2 (V:V)). These precursors were weighed into a glass vial and then heated up to 60 °C with a magnetic stirrer bar to promote adequate mixing. The solution $Cs_{0.05}(MA_{0.17}FA_{0.83})_{0.95}Pb(I_{0.17}Br_{0.13})_3$ was then filtered using a 0.2 μm PTFE filter and deposited via spin coating onto the planar SnO_2 films. Triple cation perovskite solution was deposited in a two-step program at 1000 rpm and 6000 rpm for 10 and 20 s, respectively to precisely control the thickness and uniformity of the layer. During the second step, 300 mL of chlorobenzene (99.9%) antisolvent was dropped on the spinning substrate 5 s prior to the end of the spin coating to promote crystallisation. The difference in drop times between $MAPbI_3$ and the triple cation is due to $MAPbI_3$ typically crystallizing faster compared to mixed halide perovskites due to its simpler chemical composition. This was followed by annealing the films at 100 °C for 1 hour to evaporate away any residual solvent and improve the crystallinity of the film, forming a ~450 nm thick triple cation perovskite layer.

2.1.5 Hole Transport Layer Fabrication and Deposition

2,2',7,7'-tetrakis(N,N-di-*p*-methoxyphenylamine)-9,9-spirobifluorene (spiro-OMeTAD, 90 mg in chlorobenzene) as a hole-transporting layer (HTL) was deposited on the perovskite layer by spin coating 100 μL of the prepared solution at 4000 rpm for 20 s. The spiro-OMeTAD (Sigma-Aldrich) solution was prepared by dissolving 90 mg mL^{-1} spiro-OMeTAD in DMSO and then further doping the solution with bis(trifluoromethane)-sulfonimide lithium salt (99.95%, Sigma-Aldrich) dissolved in acetonitrile (520 mg mL^{-1}), tris(2-(1H-pyrazol-1-yl)-4-tert-butylpyridine)-cobalt(III) tris(bis(trifluoromethylsulfonyl)imide) (FK 209, from Dyenamo) and 4-tert-butylpyridine (96%, Sigma-Aldrich) with concentrations of 34 μL, 10 μL and 19 μL respectively. The entire fabrication process was conducted in a nitrogen-filled glovebox to protect the films from oxygen, moisture, and other contaminants. Following the deposition of the hole transport layer (HTL), the devices were left outside the glovebox overnight to undergo oxidation. This step is critical for the doping process of spiro-OMeTAD, which is believed to enhance the material's conductivity, thereby improving the photovoltaic performance of the devices [4].

2.1.6 Anode Deposition

The final step in device fabrication was anode deposition by thermal evaporation of a gold top contact – using gold wire (99.9%, 1 mm, Kurt J. Lesker). The gold was thermally evaporated onto the HTL to form a ~70 nm gold layer as back contact, with 5 pixels an active area of 0.15 cm^2 and a single pixel with an active area of 1 cm^2 (as shown in figure 2.4 below), using an Edwards 306 thermal evaporator. Only the 0.15 cm^2 pixels were tested, as their smaller size increases the likelihood of uniform material deposition and minimizes defects compared to the larger pixel, resulting in better performance. During this process the chamber was pumped down to a pressure of ~2x10^{-5} bar.

Figure 2. 3: Evaporated gold contacts on the perovskite device.

2.1.7 Polyimide/Epoxy/Glass Encapsulation

To improve the lifetime of the cells, devices were then glass encapsulated. A strip of polyimide tape is stuck over the cell leaving part of the gold contacts uncovered allowing a contact to be made to the cell. UV curable epoxy is then deposited in the centre of the polyimide tape and a thin piece of 20 × 24 mm cover glass is placed on top of the adhesive. Even pressure is applied to the top of the cover glass so that the adhesive spreads covering the pixels. The adhesive is then cured under UV light for 7 minutes, this ensures rapid and controlled polymerization, minimizes heat exposure to sensitive perovskite materials, enhances optical transparency. It was observed that the active materials reacted chemically with the epoxy wherever the polyimide tape was not applied. This reaction caused the perovskite to become visibly transparent after a few I-V measurements or when stored outside the glovebox for an extended period. However, the areas covered with polyimide remained dark, indicating that the perovskite was preserved. This finding demonstrates that polyimide can serve as an effective barrier layer, preventing any chemical reaction between the perovskite layer and the epoxy glue.

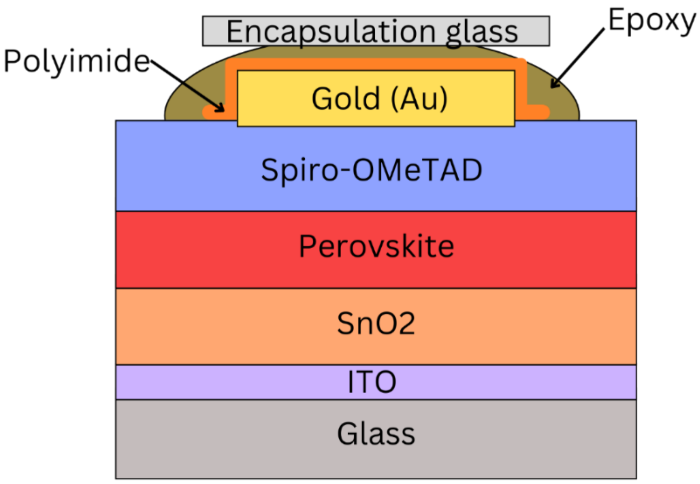

Figure 2. 4: a schematic of the perovskite solar cell architecture with encapsulation.

Table 2. 1: a schematic of the perovskite solar cell architecture with encapsulation.

Encapsulation Glass	1.1 mm
Gold (Au)	70 nm
Spiro-OMeTAD	75 nm
$MAPbI_3$/Triple Cation	450 nm
SnO_2	25 nm
ITO	120-160 nm
Glass Substrate	1.1 mm

2.2 Characterization Techniques

2.2.1 Solar Simulator and Set Up/Calibration to Measure the AM0 Device Performance

A solar simulator equipped with a 450 W Xenon lamp (Sol3A Class AAA, Oriel, USA) was utilized to replicate sunlight at 1 sun AM1.5G within a laboratory setting. To simulate the Martian sunlight spectrum and intensity, the AM1.5G filter was substituted with an AM0 filter and a 0.4 Neutral Density (ND) filter, permitting only 40% light transmission, resulting in 0.4 sun AM0 illumination (~54.7 mW/cm^2) – this was the closest to the sun intensity of Mars (58.9 mW/m^2) we could achieve, using the available resources. The lamp was then calibrated by matching the short-circuit current density (J_{SC}) under the AM0 spectrum with the J_{SC} derived from integrating the measured external quantum efficiency (EQE).

To emulate Martian temperatures, the solar cells were placed in a vacuum electrical chamber (Linkam Scientific – HFS600E-PB4 probe stage), controlled via software that allows temperatures to be regulated from -196 °C to 350 °C. A dewar filled with liquid nitrogen was connected to achieve the lower temperature range. The pressure inside the chamber was reduced to 0.5 mbar using a vacuum pump. Two tungsten probes were attached to the electrical connectors inside the chamber and manually positioned to establish contact at the appropriate points on the devices, as displayed in figure 2.6. The chamber was situated beneath the solar simulator.

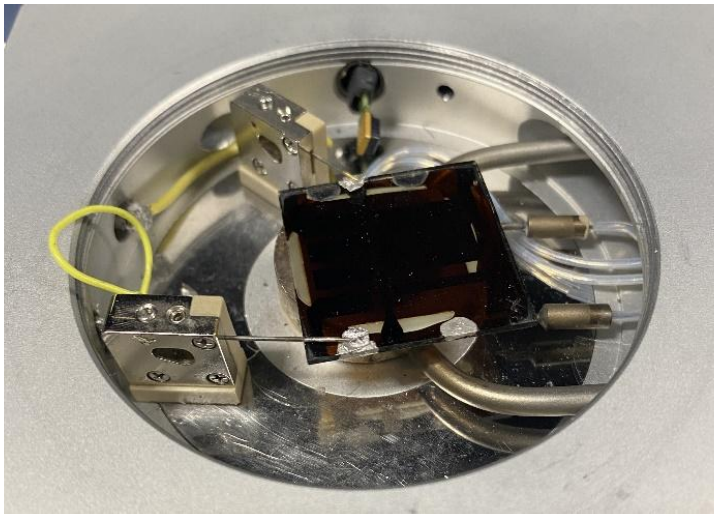

Figure 2. 5: Tungsten probes attached to the electrical connectors inside the chamber and manually positioned to establish contact at the appropriate points on the device.

The current–voltage (J–V) characteristics of the perovskite devices were measured using a digital source meter (Keithley model 2400, USA). Both forward and reverse bias scans were conducted from 1.2 to -0.1 V with a sweep interval of 0.015 V, resulting in 81 data points for each scan. The J–V characterization under 1 sun AM1.5G followed the same experimental setup and measurement parameters as for AM0, except for the filter change and the removal of the 0.4 ND filter. A picture of the setup is shown below (fig. 2.7):

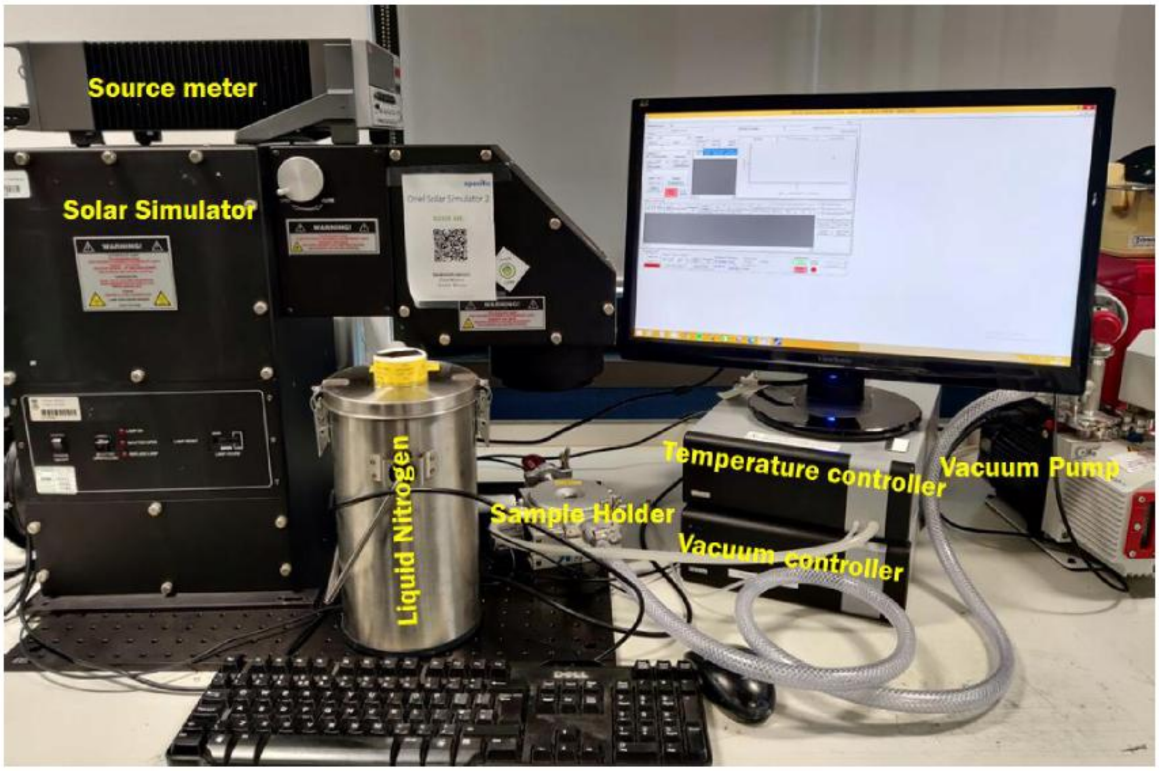

Figure 2. 6: Set up used to measure perovskite solar cells.

To accurately showcase the best performance achievable under the tested conditions, only the highest-performing devices were included in this analysis. Specifically, the data from the best-performing pixel of each device was analysed, as this approach provided a reliable representation of the maximum potential performance of the fabricated devices. Data from devices or pixels with low performance were excluded, as these were considered outliers, likely resulting from defects or inconsistencies in the fabrication process.

2.2.2 EQE

The EQE measurements used a QEX10 Quantum Efficiency Measurement System calibrated with a NIST-certified Si cell from PV Measurements. A xenon-quartz tungsten halogen light source, which contains a broad range of wavelengths, is passed through a monochromator to obtain a range of monochromatic light at different wavelengths. This light beam illuminates the solar cell, and the photocurrent generated is recorded as a function of wavelength. The measurements can be taken under DC mode, or under an AC mode for more sensitive measurements by using a light chopper with a variable frequency.

The EQE measurements performed here were taken using the AC mode with the chopper set to a frequency of 72 Hz and measured between 300-1000 nm.

2.2.3 Thickness Measurements

The thickness measurements were taken prior to the commencement of this work; however, they were taken using the Alpha Step D-500 stylus profilometer (KLA Tencor). For those measurements, the stylus force was set to 5 mg and for each sample, 3 measurements were taken at different locations with the software included with the profilometer automatically calculating the average and standard deviation of the measured thicknesses.

2.2.4 PL Measurements

PL measurements were performed with a Renishaw inVia Raman system (Renishaw plc., Wotton-Under-Edge, UK) in backscattering configuration. A 532-nm laser and 50x objective were used (NA 0.50, spot size ~1 μm). For PL measurements, a laser power of 150 nW and an acquisition time of 1 s were used to measure 180 different points through the glass substrate, which were also averaged. For the open circuit PL (PL_{OC}) measurements, the samples we placed onto a microscope slide and measured.

2.2.5 Humidity Measurements

The humidity experiments were performed using a Linkam RHGen Relative Humidity Controller in tandem with a HFS600E-PB4 probe stage. Two positional tungsten probes were attached to the electrical connectors within the sample chamber and moved manually to make contact at the devices' appropriate points. The electrical humidity stage is operated through a touchscreen and allows for a relative humidity (RH) value between 5%-95%.

2.3 Experiments

2.3.1 Thermal Stepping

All thermal measurements were conducted over a duration of approximately 3–4 hours. Extending the measurement period to better simulate Martian conditions was not feasible due to limitations in the testing setup. Specifically, the software was not automated, requiring each measurement to be taken manually, and daily lab access was restricted. As a result, the tests had to simulate a Martian day at a much faster rate than it would naturally occur. The rapid temperature changes, along with differences in light exposure duration and other environmental factors, could affect the devices in ways that would not accurately reflect real Martian conditions, therefore measurements that accurately simulate a Martian day cycle should be examined in future work. Furthermore, the analysis utilised the average data from two $MAPbI_3$ and triple cation devices, each sourced from different fabrication batches.

Experiment on power conversion efficiency was carried out on PSCs on a solar simulator at Martian environment condition setting, that is: light spectrum of AM0 with intensity of 0.4 sun (54.7 mW/cm^2) with a 0.4 ND filter and constant vacuum of ~0.5 mbar (pressure on Mars is ~6.1 mbar, however, 0.5 mbar was used to avoid ice forming on the devices during the measurements, as discussed in the thermal cycling chapter (section 4.1) with temperature range from 20 °C to -125 °C and back to 20 °C in 10 °C steps, at a ramp rate of 30 °C/min. The devices were held at the measurement temperature for 3 min prior to each measurement to allow for thermal equilibration. This equilibration time is believed to be long enough to make possible effect of scan speed negligible.

2.3.2 PL Measurements

PL measurements were performed with a Renishaw inVia Raman system (Renishaw plc., Wotton-Under-Edge, UK) in backscattering configuration. A 532-nm laser and 50x objective were used (NA 0.50, spot size ~1 μm). For PL measurements, a laser power of 150 nW and an acquisition time of 1 s were used to measure 180 different points through the glass substrate, which were also averaged. For the open-circuit PL (PL_{OC}) measurements, the samples we placed onto a microscope slide and measured. $MAPbI_3$ and triple cation perovskite devices were placed inside the PL machine and experiment on power conversion efficiency was carried out on $MAPbI_3$ and triple cation perovskite devices at Martian environment condition setting, that is: constant vacuum (~0.5 mbar) with temperature range from 20 °C to -125 °C and back to 20 °C in 10 °C steps, with heating/cooling rate of 30 °C min^{-1}. The devices were held at the measurement temperature for 3 min prior to each measurement to allow for thermal equilibration.

2.3.3 Thermal Cycling

Then, experiment on thermal cycling was executed on the same Perovskite devices under the same conditions: $0.4 \times AM0$ intensity and constant vacuum (~0.5 mbar) with temperature cycling from 20 °C to -125 °C back to 20 °C and so on for a total of 16 cycles with heating/cooling rate of 30 °C min^{-1}, devices were then held at the measurement temperature for 3 min prior to the measurement to allow for thermal equilibration. The analysis utilised the average data from two $MAPbI_3$ and triple cation devices, each sourced from different fabrication batches.

2.3.4 Jezero Crater Temperature Profile

A temperature profile measurement was based on the temperature profile of Jezero Crater captured by the Perseverance Rover [5]. As displayed earlier in figure 1.15, the red line (temperature at the surface) was used as the reference, as the surface temperature is the highest during the day, as the Martian surface absorbs solar radiation directly, heating up more than the air above it. This absorbed heat is then conducted to the thin layer of air in direct contact with the surface, raising its temperature more than the air just a short distance above. Therefore, for best performance a solar array would benefit from such configuration.

24 hours of local Mars time was shortened into a 3-hour measurement in the lab for simplicity – meaning that the temperature ramp rate increased by a magnitude of ~10. The measurement was divided into 6 stages for simplicity:

1. 22:00 to 24:00, temperature change in Jezero crater is ~2 °C. That means $\frac{120\ min}{10} =$ 12 min for stage one. $ramp\ rate = \frac{2\ °C}{12} = 0.1667\ °C/min.$
2. 24:00 - 6:00. ΔT = 8 °C. ramp rate = 0.222 °C/min
3. 6:00 - 13:00. ΔT = 75 °C. ramp rate = 1.667 °C/min

4. 13:00 - 18:00. ΔT = 50 °C. ramp rate = 1.667 °C/min
5. 18:00 - 24:00. ΔT = 17 °C. ramp rate = 0.4722 °C/min
6. 24:00 - 2:00. ΔT = 3 °C ramp rate = 0.25 °C/min

The conditions used for these measurements – $0.4 \times AM0$ intensity and constant vacuum (~0.5 mbar) to avoid ice formation on the devices during measurements. Temperature ranges from -70 °C at 00:00 local Mars time (midnight), to -78 °C at 06:00 (shortly before sunrise), -3 °C (the highest temperature) at 13:00, -53 °C at 18:00 (sunset) and finally back to -70 °C at 00:00 (midnight).

2.3.5 Humidity Stepping

Just as with thermal measurement, humidity stepping, cycling and humidity profile measurements were conducted over a duration of approximately 3–4 hours. Extending the measurement period to better simulate Martian conditions was not feasible due to limitations in the testing setup. Specifically, the software was not automated, requiring each measurement to be taken manually, and daily lab access was restricted. As a result, the rate of humidity change during the tests had to be increased. This adjustment may not accurately represent the operational conditions on Mars, as the accelerated humidity change rate would likely affect the solar cells differently. Moreover, only the best performing devices data was used in data analysis to better represent the potential of these PSCs. This means that data of worse performing PSCs was discarded.

J-V measurements were conducted using the humidity-controlled stage under 0.4 sun AM0 illumination and under nitrogen gas environment (0.1 bar at 90% RH, ~1 bar at 10% RH). The difference in pressure at the minimum and maximum RH% is due to the pressure needing to be slowly reduced until its 0.1 bar at 90% RH for the ramp rate to stay consistent because, unlike thermal measurements, it cannot be controlled using the software.

2.3.6 Humidity Cycling

Humidity cycling J-V measurements were performed under the same conditions – 0.4 sun AM0 intensity and in nitrogen gas (0.1 bar at 90% RH, ~1 bar at 10% RH) with humidity cycling from 10% RH to 90% RH back to 10% and so on for a total of 7 cycles and 3 minutes at each step. The difference in pressure at the minimum and maximum RH% is due to the pressure needing to be slowly reduced for the ramp rate to stay consistent, until its 0.1 bar at 90% RH.

2.3.7 90% Humidity Endurance

Devices were left in humidity chamber at 90% RH for a total of 1440 minutes (24 hours) with measurements taken after: 0, 2, 4, 8, 16, 24, 32, 48, 64, 96, 128, 196, 256, 1440 min at 90% RH. J-V measurements were recorded under 0.4 sun AM0 intensity and in nitrogen gas (0.1 bar).

2.3.8 Jezero Crater Humidity Profile

A temperature profile measurement was based on the temperature profile of Jezero Crater captured by the Perseverance Rover, as illustrated earlier in figure 1.16. Same logic of experiment set up was used here as in the Jezero Crater temperature profile: 24 hours of local Mars time, shortened into a 3-hour measurement in the lab – meaning the temperature ramp rate increased by a magnitude of ~10. J-V measurements were recorded under 0.4 sun AM0 intensity and in nitrogen gas (~1 bar). Humidity ranges from 10% at 01:00 local Mars time, to 30% at 06:00 (shortly before sunrise) and back to 10% RH at 08:00 and it remains there until 01:00.

References

1. Barbé J, Pockett A, Stoichkov V, Hughes D, Lee HK, Carnie M, Watson T, Tsoi WC. In situ investigation of perovskite solar cells' efficiency and stability in a mimic stratospheric environment for high-altitude pseudo-satellites. Journal of Materials Chemistry C. 2020;8(5):1715-21
2. Jiang, Q. et al. Enhanced electron extraction using SnO2 for high-efficiency planar-structure HC(NH2)2 PbI3-based perovskite solar cells. Nat. Energy 2, 16177 (2017)
3. Ossila. Perovskites and perovskite solar cells: an introduction [Internet]. Available from: https://www.ossila.com/pages/perovskites-and-perovskite-solar-cells-an-introduction

4. Ouedraogo NA, Odunmbaku GO, Guo B, Chen S, Lin X, Shumilova T, Sun K. Oxidation of spiro-OMeTAD in high-efficiency perovskite solar cells. ACS Applied Materials & Interfaces. 2022 Jul 19;14(30):34303-27.]
5. Rodriguez-Manfredi JA, De la Torre Juárez M, Sanchez-Lavega A, Hueso R, Martínez G, Lemmon MT, Newman CE, Munguira A, Hieta M, Tamppari LK, Polkko J. The diverse meteorology of Jezero crater over the first 250 sols of Perseverance on Mars. Nature Geoscience. 2023 Jan;16(1):19-28

Chapter 3: Thermal Stepping and Photoluminescence Characterisation

This chapter investigates the thermal stability and performance of methylammonium lead iodide ($MAPbI_3$) and triple cation ($Cs_{0.05}(MA_{0.17}FA_{0.83})_{0.95}Pb(I_{0.17}Br_{0.13})_3$) perovskite solar cells under simulated Martian environmental conditions. Thermal stepping part elucidates the effects of temperature variations on critical performance metrics – PCE, V_{OC}, FF and J_{SC}. Meanwhile, the photoluminescence section analyses how temperature variations affect intrinsic material properties, recombination dynamics, transport inefficiencies and load-dependent losses, offering deeper insights into the optoelectronic behaviour of the devices.

Through multiple iterations of both methylammonium lead iodide and triple cation devices, the study reveals differences in thermal stability and performance. Triple cation perovskite solar cells consistently exhibit higher efficiency; however, they display reduced resilience at temperatures below -50 °C, with slightly greater performance degradation compared to $MAPbI_3$ devices. This suggests that while triple cation cells outperform in general conditions, $MAPbI_3$-based cells can potentially offer an advantage in extremely low-temperature environments.

3.1 Thermal Stepping

3.1.1 Thermal Stepping Measurement of $MAPbI_3$-Based Devices

To begin, the most relevant baseline measurements available for this study were conducted at room temperature (~20 °C) under a pressure of approximately 0.5 mbar. While this temperature closely represents standard ambient conditions, the significantly reduced pressure deviates from true ambient atmospheric conditions. Nonetheless, this low-pressure environment does not have an immediate impact on encapsulated devices, as suggested in previous research by Barbé *et al.* [1]. Their findings indicate that both encapsulated and non-encapsulated perovskite solar cells exhibit comparable behaviour when exposed to AM0 illumination at 0 °C and 10 mbar for five hours. This similarity is attributed to the gold electrode, and possibly the Spiro-OMeTAD layer, which can act as a partial barrier, preventing the immediate loss of volatile degradation byproducts. However, it is suggested that over extended periods, vacuum conditions could accelerate the irreversible degradation of non-encapsulated devices, as the gold contact alone does not provide an effective seal [1]. These findings reinforce the importance of robust encapsulation strategies, such as the Polyimide/Epoxy/Glass approach employed in this research, to ensure the long-term stability of perovskite solar cells in low-pressure extraterrestrial environments.

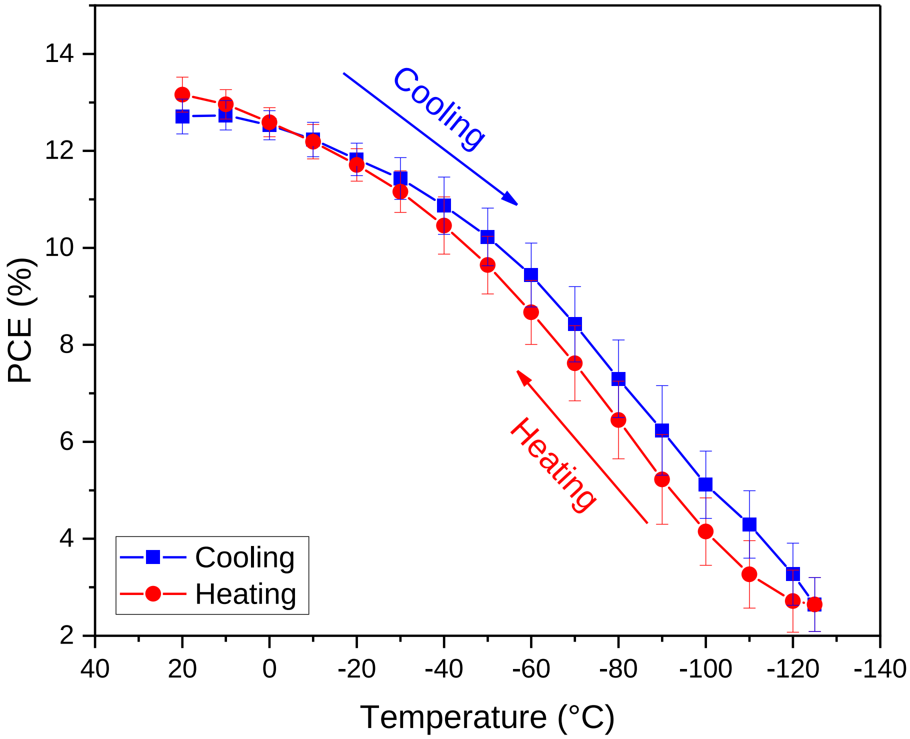

Figure 3. 1: Average 0.4 AM0 intensity PCE versus temperature of the MAPbI$_3$-based devices, including error bars representing the standard deviation. The devices were first cooled from 20 °C to -125 °C, then heated back to 20 °C.

Here, the average of two MAPbI$_3$-based devices are analysed first, as they are like model material which have been well studied. Fig. 3.1 shows the average $0.4 \times$ AM0 (54.7 mW/cm^2) power conversion efficiency versus temperature of the MAPbI$_3$-based devices.

The selected temperature range of 20 °C to -125 °C for the measurements was determined based on the extreme temperature variations experienced in Martian environmental conditions. The chosen temperature range encompasses the full spectrum of temperatures encountered on the Martian surface [2]. The averaged PCE was measured from 20 °C to -125 °C (cooling process), then reheated from -125 °C to 20 °C (heating process). To discern overarching patterns, an average of successful thermal stepping measurements was analysed and graphically represented.

At the ambient temperature of 20 °C, the average PCE is 12.71%. Subsequently, a consistent decline in PCE is observed, having a constant rate of reduction (averaging a reduction of 0.26% per 10 °C drop) until approximately -30 °C. Beyond this point, the rate of PCE decline increases, accelerating to a rate of -0.88% per 10 °C decrease until the final measurement at -125 °C. Consequently, the PCE at -125 °C is 2.65%, representing a 79% reduction in PCE compared with that of the initial room temperature (20 °C) measurement. In other research it has been shown that PCE typically improves at temperatures below 20 °C, primarily due to an increase of V_{OC} [3], however, this does not align with our results, moreover, similar findings have been reported by Sun *et al.* [4], further supporting this discrepancy.

The cooling and heating power conversion efficiencies exhibit notable similarity (refer to fig. 3.1), indicating a regenerative nature in the encountered PCE loss during the cooling phase. Importantly, when $MAPbI_3$-based devices were heated, the PCE at each of the temperatures was similar to the PCE of the corresponding temperatures during the cooling phase. Similarly, the rate of increase in PCE is more pronounced until approximately -50 °C, subsequently exhibiting a deceleration of PCE enhancement at > -50 °C. Ultimately, the heating phase culminates in a restoration of the PCE to 13.16%, 0.45% higher when compared to the initial 12.79% recorded at the outset.

It is noteworthy that the lowest recorded efficiencies occur during the evening or nighttime temperatures on Mars, implying that extremely low temperatures would not profoundly impact the overall capabilities of the solar arrays, given the absence of sunlight.

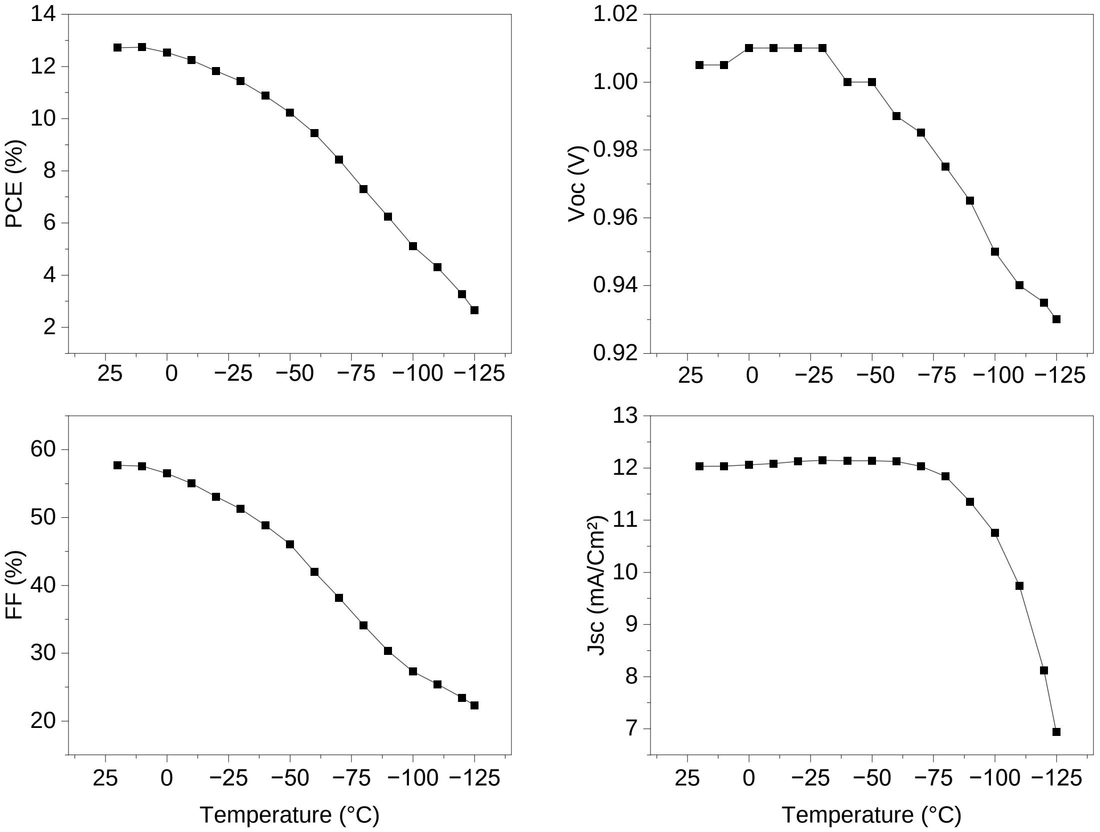

Figure 3. 2: (a) Average 0.4 AM0 intensity PCE versus temperature of the $MAPbI_3$-based devices. The devices were first cooled from 20 °C to -125 °C, then heated back to 20 °C.

To understand which device parameter(s) are causing the reduction of the averaged PCE at lower temperatures, the PCE, V_{OC}, FF and J_{SC} of the $MAPbI_3$-based devices as a function of reducing temperature is shown in Fig. 3.2. As the device parameters at each temperature during heating back to 20 °C are very similar to that of the cooling, the device parameters as a function of increasing temperature are not shown here.

As shown in fig. 3.2, the open-circuit voltage has distinct trends that can be categorised into two sequential stages. Initially, within the temperature range from 20 °C to -30 °C, V_{OC} remains stable, 1.005 V to 1.01 V. Subsequently, a pronounced rapid descent in V_{OC} from 1.01 to 0.93 V is observed from -30 °C to -125 °C. From literature [5], V_{OC} is typically expected to rise until -80 °C [6], this could result from Fermi–Dirac distribution becoming narrower and the quasi-Fermi level moving towards the band edges at low temperature for a fixed charge carrier density [7]. When T < -80 °C, it is expected for the voltage to decrease due to enhanced recombination or a reduced probability for charge carrier generation by exciton dissociation [8] (this also coincides well with the strong J_{SC} decrease around that temperature). Some have theorised that the reason V_{OC} decreases at the lowest temperatures, is due to the charge-selective pin structure, which cannot be maintained due to missing free charges [6]. However, here, the voltage declines from the start with each -10 °C step. However, the exact reason why V_{OC} follows the pattern shown in fig. 3.2 is not understood and should be examined in future work. Many researchers [9] have demonstrated that even minor changes in precursor composition and preparation techniques – such as molar ratios, deposition methods, and annealing processes – can significantly impact the properties of perovskite films. Therefore, it is possible that some fabrication imperfections or inconsistencies could be contributing to the unusual V_{OC} trend observed.

From figure 3.2 it can be seen that the FF has the biggest impact on the declining PCE with falling temperature. The fill factor decreases with reducing temperature, from an initial FF of 57.66% at 20 °C, there is a considerable linear decline to 22.28% at -125 °C. This represents a notable 61% reduction from the initial FF value. The trend in FF across the cooling phase highlights substantial changes in the resistance of the device (particularly series resistance – a big part of it probably has to do with transport resistance within the absorber [10]). The decrease in the FF at lower temperatures can also be caused by limited charge carrier transport and extraction at the interfaces between the absorber and the adjacent ETL and HTL [11], or altered recombination rates, or the S-shaped photocurrent that is impacted by the inefficient charge extraction at defective interfaces and increase of interfacial charge accumulation [5].

The observed J_{SC} also decreases with reducing temperature, which could be described into two stages. Commencing at 12.03 mA/cm² at 20 °C, the J_{SC} slightly increases until -50 °C to 12.14 mA/cm². Afterwards, it remains stable until -80 °C where it is measured to be 11.84 mA/cm². The sudden dive in J_{SC} at $T \leq -80$ °C is interesting, but most likely is correlated with the exponential rise in series resistance, as described later. Other researchers have observed reduced current at ~213 K and attributed this to the trapping of charges [12] which does kind of correlate with the results seen in fig. 3.2, as it is around that temperature range, that the J_{SC} starts falling. Finally, the current density declines rapidly to 6.94 mA/cm² at -125 °C. This reflects a substantial 42% reduction in J_{SC} from the initial value. Although, on one hand, the reduced J_{SC} can be attributed solely to charge transport problems, it is also possible that charge separation (i.e., exciton splitting) affects the current at low temperatures [6]. On the other hand, Wang *et al*. [13] suggested that the observed increase in J_{SC} with temperature is caused by the increase in the mobility of electrons with temperature due to thermally assisted carrier trapping and de-trapping. Similarly, the mobility of holes in spiro-OMeTAD improves through inter-molecular hopping, as a result, the carrier collection efficiency is enhanced.

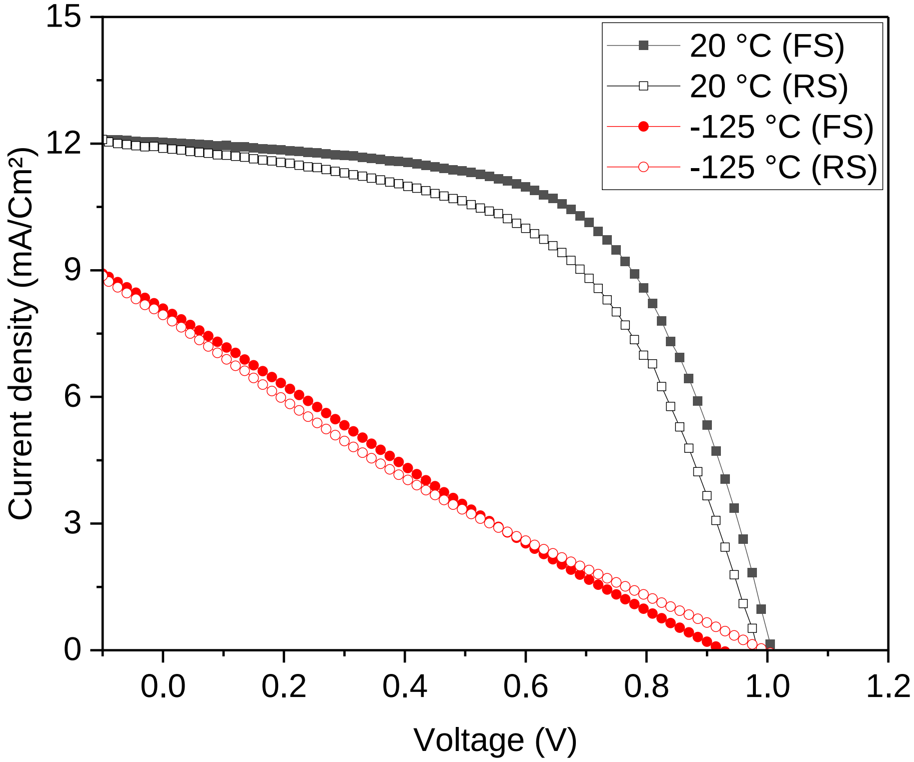

Figure 3. 3: J-V curve of one of the $MAPbI_3$-based devices. Initial (20 °C) and final (-125 °C) forward (FS) and reverse scan (RS) J-V curves.

Mismatch, or a well-known hysteresis, between forward and reverse scans is observed for all the devices (example of a $MAPbI_3$ device shown in fig. 3.3). Exact reason for hysteresis is unknown, but a common theory is that it is caused by ion migration through the perovskite device under bias [14]. The highest performance was observed in forward scans, this behaviour has been credited to polarity driven ionic motion in the perovskite absorber [15], for this reason, forward scan direction is examined in all measurements. S-shaped J-V curves, which indicate hindered charge extraction due to nonoptimal contact properties are observed too. The more temperature decreases, the more J-V curves change from an S-shape to almost straight lines (as seen in figure 3.3, at -125 °C), this reveals highly resistive behaviour [6]. Other groups that have also observed similar shaped J-V curves and have accredited it to the loss in conductivity, which in turn contributes to the increase in series resistance with decreasing temperatures. Colenbrander *et al*. explained that this is caused by the reduction in electrical conductivity, which was explained by a pile-up of electrons and holes at the perovskite and charge transport layer interface [16]. That in turn significantly affects and increases the series resistance [16]. Additionally, it has been discussed that the mobility of charge carriers in the perovskite layer itself might decrease with temperature [6].

To determine the impact of resistance, approximate series resistance (R_S) is extracted from J-V curves measured in the forward direction, by calculating the slope of A/V.

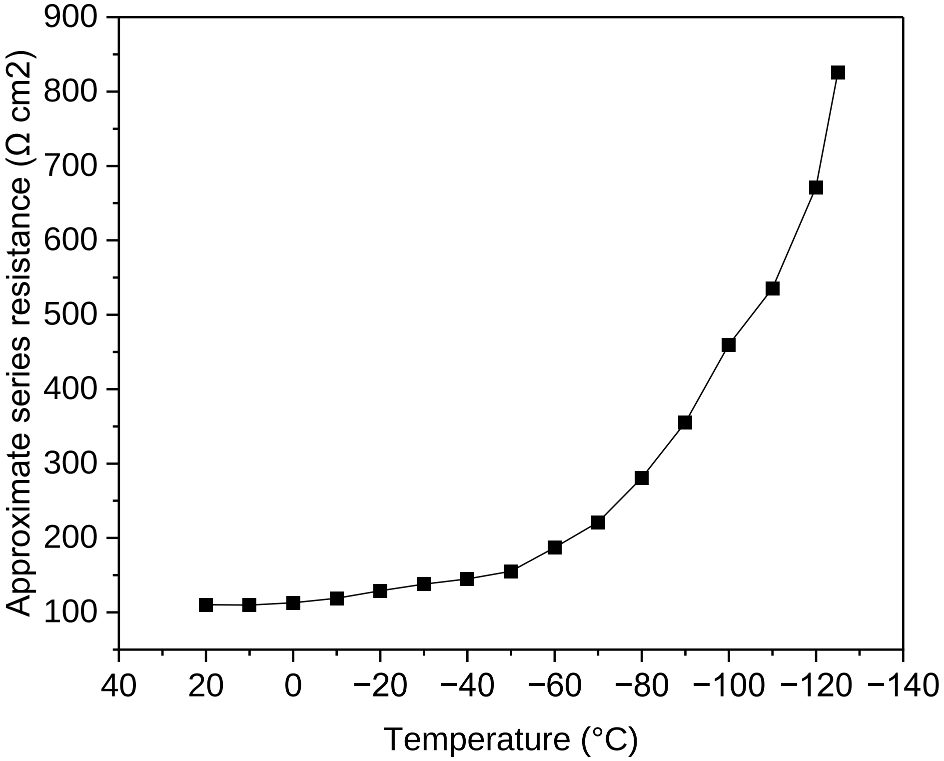

Figure 3. 4: Series resistance of a $MAPbI_3$-based device plotted against temperature.

In figure 3.4 it is illustrated how the series resistance is rising at a slower rate at 20 °C > T > -70 °C and from <-70 °C, the R_S growth becomes exponential, from 110.17 Ω cm^2 at 20 °C, to 220.97 Ω cm^2 at -70 °C, to 825.08 Ω cm^2 at -125 °C. This coincides very well with J_{SC} at the same temperature range. This also aligns well with literature, where it was reported that the conductivity and hole mobility of Spiro-MeOTAD decreases at lower temperatures [6].

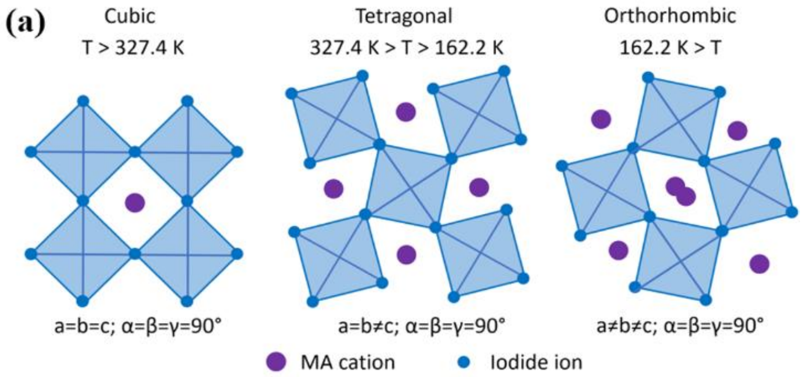

Figure 3. 5: Structural phases of $MAPbI_3$.

To add to that, it has been discovered that the structural phase transition of perovskite materials depends on temperature. As seen in figure 3.5, when T < 162.2 K (−110.95 °C) $MAPbI_3$ is in the orthorhombic phase. Above this temperature, it changes to tetragonal phase until 327.4 K (54.25 °C). Beyond 327.4 K, it becomes the cubic phase. These phase transitions affect the optical properties of the perovskite over a wide temperature range. Specifically, the onset of optical absorption shifts to higher energies as temperature increases in the tetragonal and orthorhombic phases. Additionally, strong excitonic absorption features become more pronounced at lower temperatures [17].

In this work, a phase transition from tetragonal to orthorhombic did not impact the performance parameters in a significant way, but this was also observed by others [7]. One theory is that the devices are already severely degraded, thus the phase transition does not make a substantial impact. Then, it has been theorised that the cubic phase might be described as a macroscopic time average of a range of tetragonal configurations interchanging with each other, Jacobsson *et al*. have observed that this complies with the smooth temperature trend over the phase transition [6]. Nonetheless, the impact on performance of the phase transition on $MAPbI_3$ devices is well studied. Qiu *et al*. concluded that below tetragonal phase transition temperature, the enhanced interfacial defects are caused by the low temperature, which leads to reduced charge carrier mobility and charge carrier extraction efficiency [7]. Then, Shao *et al*. reported that in the temperature range between room temperature and -133 °C, the lower charge carrier mobility within the electron transport layer (PCBM) was the primary cause of PCE losses at lower temperatures, which might apply to some extent to SnO_2 as well [3].

3.1.2 Thermal Stepping Measurement of Triple Cation-Based Devices

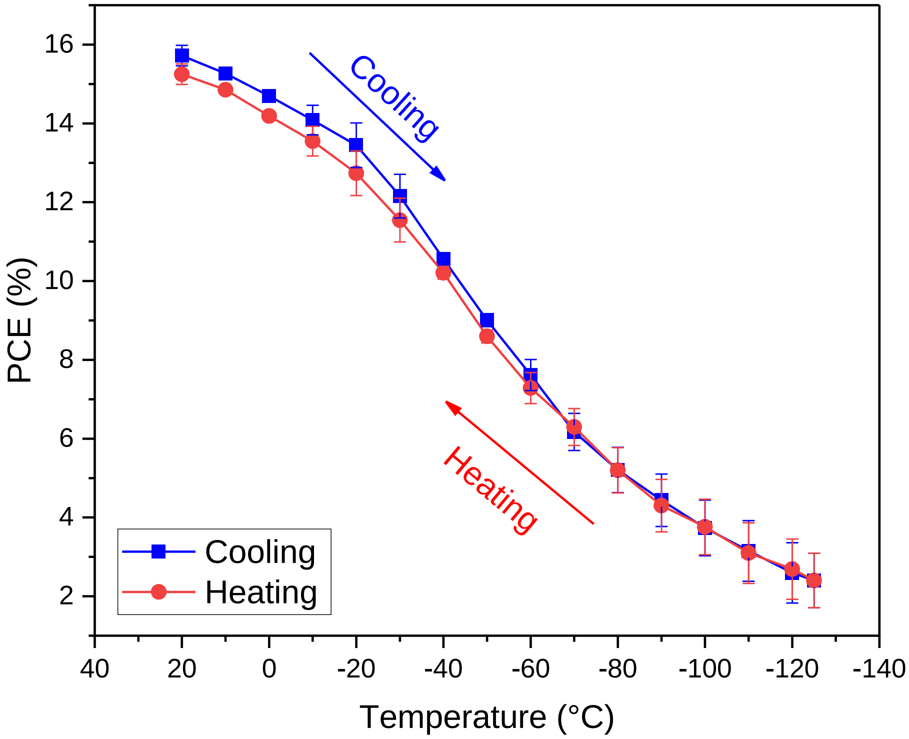

Figure 3. 6: Average 0.4 AM0 intensity PCE versus temperature of two triple cation-based devices, including error bars representing the standard deviation. The devices were first cooled from 20 °C to -125 °C, then heated back to 20 °C.

At a temperature of 20 °C, the average PCE of two devices is 15.72% (fig. 3.6). A subsequent decline in PCE is observed, with a consistent reduction rate of approximately 0.57% per 10 °C decrease until reaching -20 °C. Beyond this temperature, the rate of PCE decline accelerates to 1.37% per 10 °C decrease, continuing until -80 °C. After -80 °C, the PCE stabilizes, with an average reduction rate of 0.56% per 10 °C drop, although at significantly lower efficiency levels. Overall, the PCE drops dramatically from 15.72% at 20 °C to just 2.4% at -125 °C, representing an 85% reduction across this temperature range.

Just like for $MAPbI_3$ devices, the cooling and heating power conversion efficiencies of triple cation devices overlap well throughout the whole temperature range, indicating a regenerative nature in the encountered PCE loss during the cooling phase. The rate of increase in PCE is less pronounced until approximately -80 °C, then faster rate of enhancement of PCE until ~20 °C. Importantly, the heating phase culminates in a restoration of the PCE which is 15.25% at 20 °C, marginal 3% lower when compared with the initial 15.72% recorded at the outset.

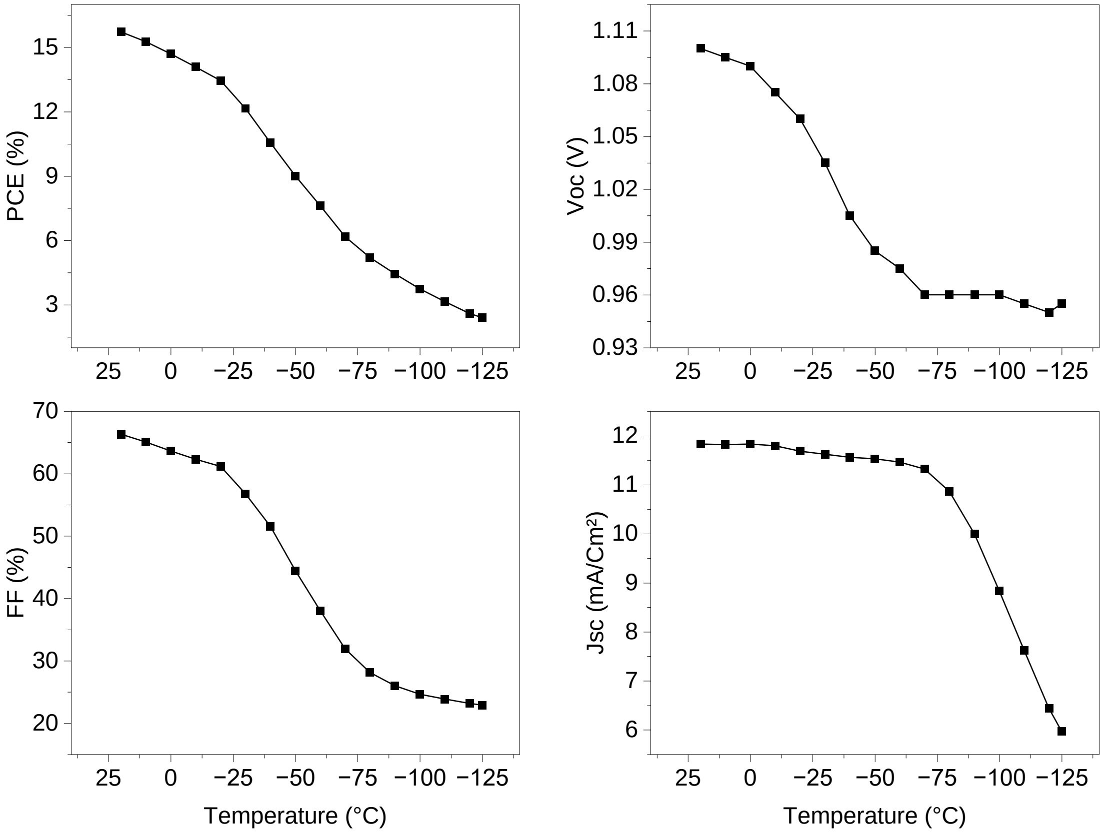

Figure 3. 7: Average 0.4 AM0 intensity PCE, V_{OC}, FF and J_{SC} of triple cation-based devices during the cooling.

As it can be seen in fig. 3.7, the open-circuit voltage has distinct trends that can be categorised into two sequential stages. Initially, within the temperature range from 20 °C to -70 °C, V_{OC} falls sharply, from 1.1 V to 0.96 V. Subsequently, V_{OC} stabilises and only decreases to 0.955 V at -125 °C from 0.96 V at -70 °C. As with $MAPbI_3$ devices, from literature [1], the V_{OC} of triple cation devices is expected to rise with decreasing temperature, but just like with $MAPbI_3$, we get the opposite trend here.

The fill factor shows a substantial linear decrease with lowering temperature, beginning at 66.29% at 20 °C and falling to 22.88% at -125 °C. This decline amounts to a notable 65% reduction from the initial FF. The trend of FF across the cooling phase is similar to $MAPbI_3$ and can be explained using the same reasoning – with falling temperatures, the increased resistance, limited charge carrier transport and extraction, in addition to changes in carrier dynamics [1] – all have significant impact on the FF.

The J_{SC} trend is a slightly different for triple cation compared to $MAPbI_3$ devices. Where the J_{SC} of $MAPbI_3$ increased slightly until around -50 °C and remained stable until -80 °C, the J_{SC} of triple cation falls from the start. At 20 °C, it starts at 11.83 mA/cm^2, then slowly falls to 11.32 mA/cm^2 at -70 °C. After this, it dives to 5.97 mA/cm^2 at -125 °C, which equates to a 50% reduction from the initial value.

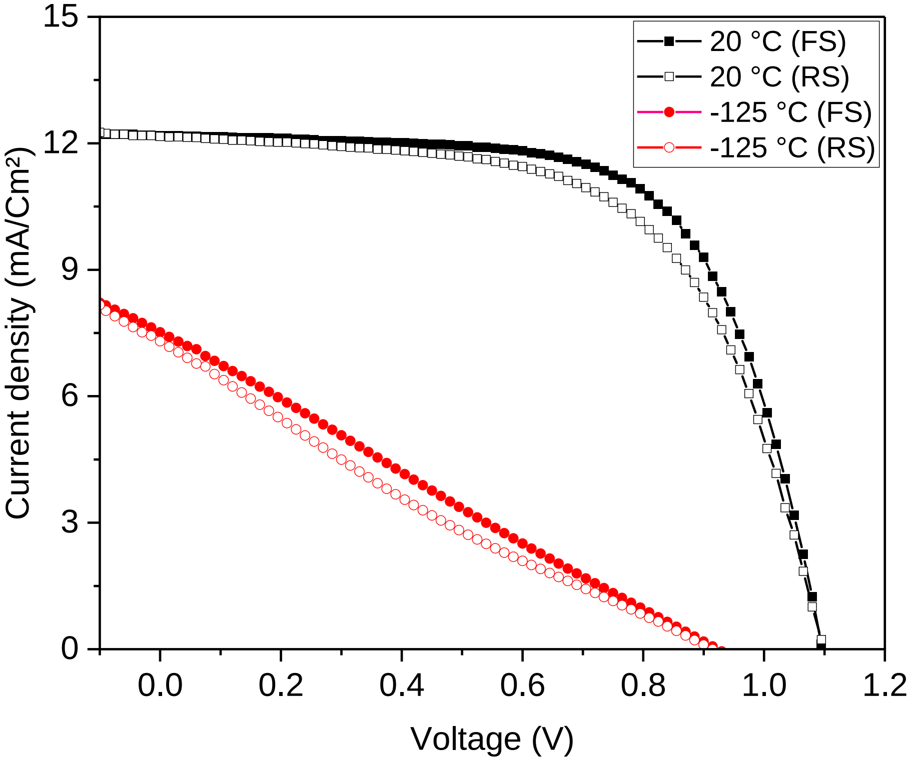

Figure 3. 8: J-V curve of one of the triple cation-based devices. Initial and final (20 °C) and -125 °C forward (FS) and reverse scan (RS) J-V curves.

Hysteresis between forward and reverse scans can be seen in figure 3.8. When compared to $MAPbI_3$, the hysteresis at 20 °C is lesser, besides, at -125 °C the inversion seen in the $MAPbI_3$ device (fig. 3.3) does not occur in triple cation device. The J-V curve shapes also align well with what was seen for the $MAPbI_3$ device. S-shape at 20 °C, but with decreasing temperature it transforms into a straight line, (fig. 3.8) which indicates high resistance.

Just like with $MAPbI_3$, approximate series resistance is extracted from J-V curves measured in the forward direction, by calculating the slope of A/V. Series resistance is plotted and illustrated in figure 3.9 below. Differently to $MAPbI_3$, the R_S begins to increase exponentially around -50 °C. Moreover, the increase is more significant, it rises from 75.51 Ω cm^2 at 20 °C, to 286.49 Ω cm^2 at -50 °C, to 1787.31 Ω cm^2 at -125 °C – 24-fold increase from the first to final measurement.

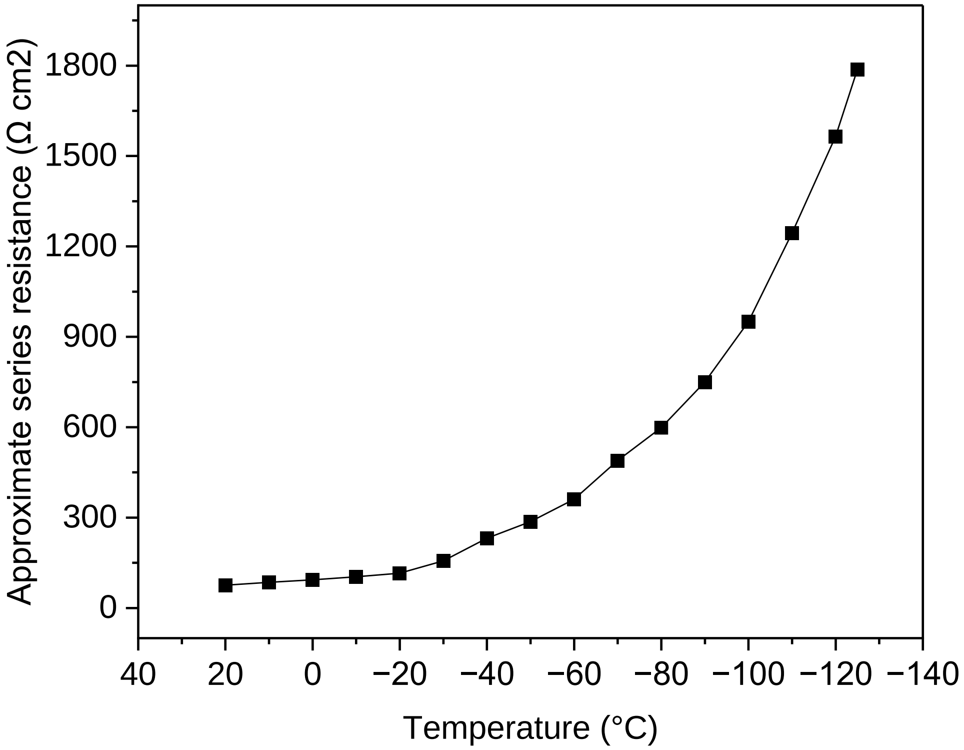

Figure 3. 9: Series resistance of a triple cation-based device plotted against temperature.

Unlike $MAPbI_3$ though, triple cation perovskite shows no evidence of a crystal phase transition in the temperature range of 4.2 – 300 K [16], as it is believed that CsFAMA material remains stable and structurally uniform in the cubic phase at all temperatures [18].

3.1.3 Comparison of Thermal Stepping Results Between $MAPbI_3$ and Triple Cation-Based Devices

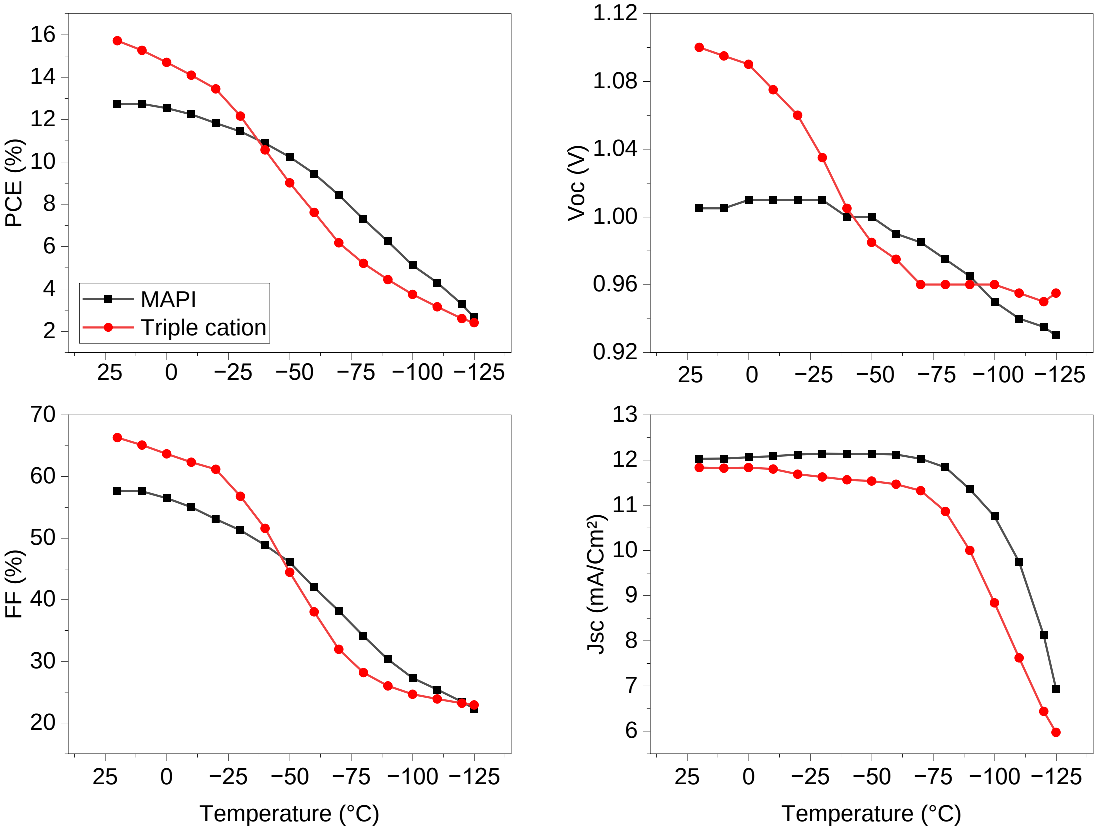

Figure 3. 10: Comparison of the average cooling performance parameters between $MAPbI_3$ and triple cation-based devices.

To begin, as shown in fig. 3.10, at 20 °C, the average cooling PCE of $MAPbI_3$-based solar cells is 12.71% while the average PCE of the triple cation-based devices is 15.72% – a 19% difference between them. On one hand, the PCE of the $MAPbI_3$-based devices decreases from 12.71% at 20 °C to 2.65% at -125 °C, while averaging a 0.67% reduction with each 10 °C step. On the other hand, the PCE of triple cation-based devices reduces from 15.72% at 20 °C to 2.4% at -125 °C, averaging a 0.88% reduction with each 10 °C step.

Secondly, at 20 °C, the average V_{OC} of triple cation-based PSCs is 1.1 V, while for $MAPbI_3$-based PSCs, it is 1.005 V. As temperatures decrease, both exhibit a decline in V_{OC}, though the rate and pattern differ. The V_{OC} of the triple cation-based solar cells decreases steadily from 1.1 V at 20 °C to 0.955 V at -125 °C, averaging a reduction of approximately 0.009 V per 10 °C step. In contrast, the V_{OC} of $MAPbI_3$-based solar cells starts at 1.005 V at 20 °C, declining to 0.93 V at -125 °C, with an average reduction of about 0.006 V per 10 °C step.

Thirdly, at 20 °C, the average FF of triple cation is 66.29%, dropping to 22.88% at -125 °C, with an average reduction of approximately 3.47% per 10 °C. For $MAPbI_3$, the FF starts at 57.66% at 20 °C and decreases to 22.28% at -125 °C, averaging a reduction of about 2.53% per 10 °C. Both types of PSCs show substantial declines in FF as temperatures fall, with triple cation-based cells maintaining a higher FF overall but experiencing a steeper decline.

Fourthly, looking at the J_{SC} data, the average J_{SC} of triple cation starts at 11.83 mA/cm² at 20 °C, slightly fluctuates around 11.8 mA/cm² down to -10 °C, then gradually decreases to 5.97 mA/cm² at -125 °C, averaging a reduction of approximately 0.47 mA/cm² per 10 °C. For $MAPbI_3$-based devices, J_{SC} starts at 12.03 mA/cm² at 20 °C and remains relatively stable until -50 °C, fluctuating around 12.14 mA/cm². It then decreases more rapidly, reaching 6.94 mA/cm² at -125 °C, averaging a reduction of about 0.45 mA/cm² per 10 °C. Both types of PSCs show a decrease in J_{SC} as temperatures fall, with triple cation-based PSCs experiencing a steadier decline compared to $MAPbI_3$-based PSCs. It is suspected that recombination could play a big role in the PSC's performance decrease. For this reason, open-circuit and short-circuit photoluminescence (PL) measurements were conducted.

3.1.4 Open-Circuit Photoluminescence Measurement of The $MAPbI_3$-Based Device

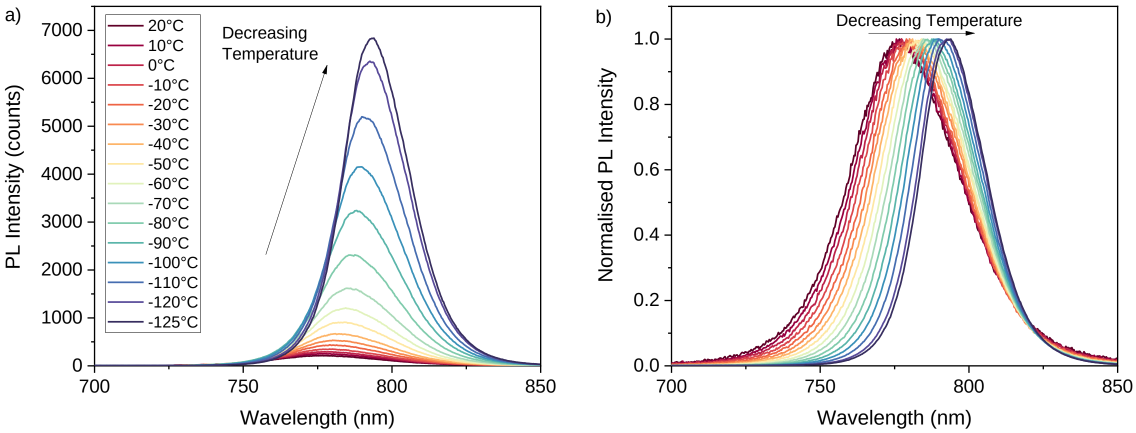

Figure 3. 11: a) PL spectra of $MAPbI_3$-based device measured at different temperatures are shown as a function of wavelength; b) normalized PL spectra of $MAPbI_3$-based device shown as a function of wavelength.

We conducted temperature-dependent photoluminescence spectroscopy under open-circuit conditions to investigate the effect of temperature on charge recombination. In open-circuit conditions, the PSC is not connected to any external circuit, meaning no charge carriers are extracted from the device. The PL spectra were obtained by placing the perovskite film in a liquid-nitrogen-cooled stage and measuring at 10 °C intervals, ranging from 20 °C to -125 °C.

As shown in figure 3.11a, the PL intensity of the $MAPbI_3$ device increases drastically as the temperature decreases. At 20 °C, the PL intensity is 213 counts. This intensity rises to 532 counts at -30 °C, 3239 counts at -90 °C, and reaches 6839 counts at -125 °C. As the temperature increases, the thermal energy within the perovskite material also rises. This additional energy helps to overcome the binding energy (E_B) of excitons, causing them to dissociate into free carriers. Consequently, with more excitons dissociating into free carriers, there are fewer bound electron-hole pairs available for radiative recombination. Radiative recombination occurs when an electron falls from the conduction band to the valence band, releasing energy in the form of light. The reduction in bound excitons leads to a decrease in PL intensity, known as quenching. Radiative recombination can still occur with these free carriers, but it tends to be less efficient than recombination involving bound excitons. At higher temperatures, free carriers recombine more slowly in a radiative manner because they are no longer bound as excitons. This slower recombination rate affects the overall PL efficiency. Conversely, nonradiative recombination processes, which do not emit light, become less significant at lower temperatures due to insufficient thermal energy to create free carriers, resulting in fewer nonradiative recombination events and thus maintaining higher PL efficiency [19]. Moreover, defects, especially shallow trap states, significantly influence the PL behaviour of the material. These shallow states can capture and release charge carriers, allowing them to recombine radiatively. As the temperature decreases, the mobility of charge carriers, or their ability to move through the material, also decreases. With reduced carrier mobility, charge carriers are more likely to be captured by shallow trap states. These trapped carriers have a higher chance of recombining radiatively, resulting in increased light emission. Consequently, the photoluminescence intensity increases at lower temperatures due to the combined effects of decreased carrier mobility and enhanced trapping by shallow states [19].

In figure 3.11b, the intensities are normalized to highlight the shift in emission peaks. A red shift is observed, with the emission peak moving from 778 nm at 20 °C to 795 nm at -125 °C, resulting in a peak shift of 17 nm (figure 3.12). The temperature dependant shift is reversible as temperature is increased. This observed shift aligns well with existing literature, confirming the consistency of our results with previous studies [20]. It should be noted that a red shift in PL does not necessarily indicate an increase in impurities, which typically function as centre for non-radiative recombination (occurs when an electron falls from a higher energy state (conduction band) to a lower energy state (valence band) without emitting light. Instead, the energy is released as heat due to interactions with the lattice of the material). Instead, the red shift is a known feature of $MAPbI_3$ perovskites and does not necessarily indicate any problems with the material [5].

Below 162 K (-111.15°C), a phase transition from the low-temperature orthorhombic phase to the high-temperature tetragonal phase was expected for $MAPbI_3$. This transition usually results in the broadening of peaks and the emergence of a secondary peak around 800 nm. Previous studies have reported the appearance of two distinct excitonic peaks in the PL spectra below 160 K, attributed to the phase change [21]. However, in our observations, the $MAPbI_3$ device did not show significant changes in its properties or a secondary peak, but this has also been observed by others [22]. This lack of noticeable change may be because the phase transition temperature may not be strictly fixed at 162 K. For example, Kong *et al.*, reported the occurrence of this phase transition in the temperature range of 150 to 130 K for $MAPbI_3$ [23], while Wright *et al.*, reported it around the 130-160 K range [24]. The observation of phase transitions in $MAPbI_3$ at varying temperatures can be influenced by several factors. These include the form of the perovskite material (such as powder, single crystal, or thin film), material thickness, and sample preparation methods (e.g., solution processing or vapor deposition). Additionally, the experimental conditions, such as the rate of temperature change and the ambient atmosphere, also play a crucial role in determining the phase transition behaviour [25].

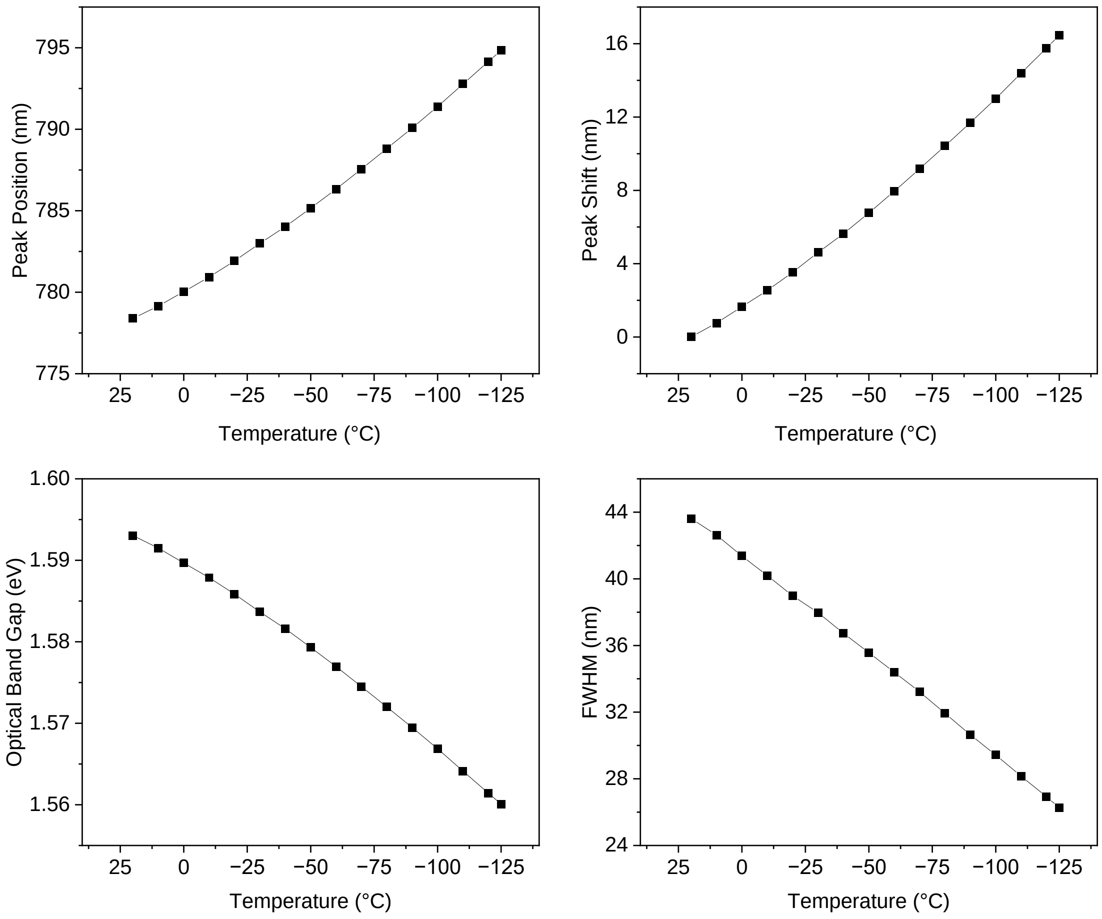

Figure 3. 12: Peak position, peak shift, optical band gap and the FWHM of the $MAPbI_3$-based device.

The variations in peak position, peak shift, optical band gap, and FWHM are more clearly illustrated in figure 3.12. As previously discussed, the peak position exhibits a linear red shift, moving from 778 nm at 20 °C to 795 nm at -125 °C, resulting in a total peak shift of 17 nm.

The optical bandgap (E_g) drops from 1.59 eV at 20 °C to 1.56 eV at -125 °C, which cannot be explained by the commonly used Varshni’s model, which is often used for describing the typical red shift of the PL emission with increasing temperature in standard tetrahedral semiconductors, like Si, GaAs, InP and others. Varshni behaviour refers to the empirical relationship described by Varshni's equation, which explains how the E_g of a semiconductor changes with temperature [26]. This behaviour of perovskite films is linked to the unique material properties and interactions within the perovskite structure, such as unusual electron-phonon coupling, changes in their crystal structure with temperature and phase transitions [20]. At higher temperatures, lattice expansion typically alters electronic energy levels in many materials, leading to a reduction in the band gap. However, in $MAPbI_3$ PSCs, lattice expansion due to increasing temperature usually causes the band gap to increase. This increase occurs because atomic orbitals overlap less, reducing the energy overlap between the conduction and valence bands. Simultaneously, higher temperatures enhance phonon activity, resulting in increased electron-phonon coupling, which can lower the energy required for electrons to transition between bands, thereby decreasing the band gap [27]. Conversely, at lower temperatures, lattice contraction and decreased electron-phonon coupling occur due to reduced phonon interactions [28]. Consequently, these two effects compete: thermal expansion tends to increase the band gap, while electron-phonon coupling tends to decrease it, which can be referred to as temperature-induced renormalization of the band gap [25].

The full width at half maximum or FWHM of the PL peak shows a similar trend with the temperature, decreasing significantly from 44 nm at 20 °C to 26 nm at -125 °C. The FWHM results are well in accordance with the literature [26]. As temperature increases, the thermal energy enables charge carriers to occupy higher energy states, resulting in a blue shift of the photoluminescence peak and a broadening of the FWHM due to the wider range of involved energies. Conversely, at lower temperatures, the reduced thermal energy limits carrier movement, leading to a narrowing of the FWHM and producing sharper spectral lines [20].

3.2.2 Open-Circuit Photoluminescence Measurement of The Triple Cation-Based Device

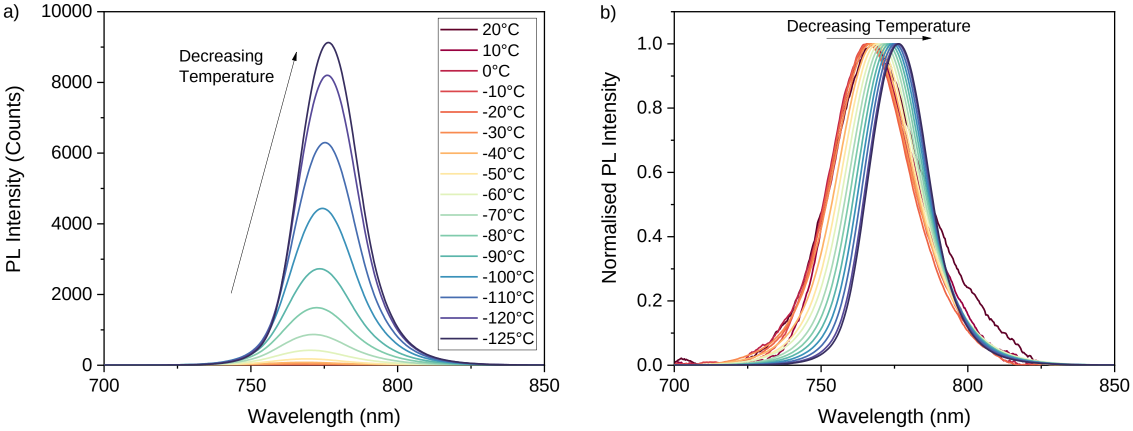

Figure 3. 13: a) PL spectra of triple cation-based device measured at different temperatures are shown as a function of wavelength; b) normalized PL spectra of triple cation-based device shown as a function of wavelength.

As shown in figure 3.13, the qualitative observation of experimental results for the triple cation-based device shows several notable features. Initially, the PL emission peak undergoes a blue shift from 769 nm to 767 nm with temperature decreasing from 20 °C to -40 °C which is not well understood. Beyond this temperature, the PL peak begins to linearly red shift. Overall, the peak position starts at 769 nm at 20 °C and shifts to 777 nm at -125 °C, resulting in a total peak shift of 8 nm, which is reversible when temperature is increased. The red shift observed in CsFAMA perovskite is generally attributed to lattice expansion, which can be induced by external factors such as temperature, pressure, or illumination. This slight lattice expansion alters the spacing between atoms, reducing the effectiveness of defects (trap states) in capturing charge carriers. Consequently, the number of trap states decreases, leading to reduced non-radiative recombination. With fewer traps, a greater proportion of charge carriers can recombine radiatively, emitting light rather than dissipating energy as heat, thereby increasing the PL intensity [29].

The optical band gap remains constant at 1.61 eV from 20 °C to 10 °C. It then increases to 1.62 eV, which is maintained until -30 °C. Below this temperature, the band gap decreases back to 1.61 eV and stays at this value until -80 °C. Between -80 °C and -125 °C, the band gap further decreases to 1.60 eV.

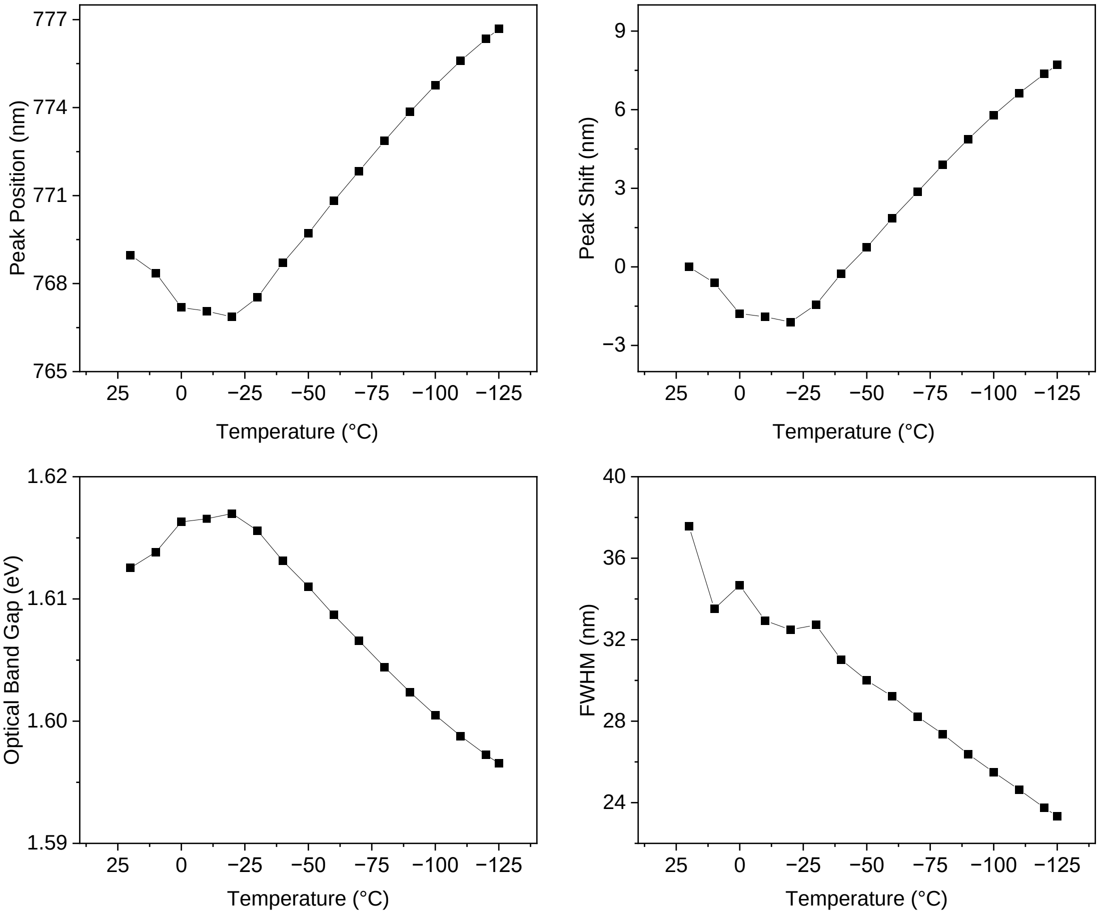

Figure 3. 14: Peak position, peak shift, optical band gap and the FWHM of the triple cation-based device.

The FWHM generally decreases with decreasing temperature. However, there are two notable exceptions: at 0 °C and -30 °C, where the FWHM shows a slight increase, interrupting the overall trend. Specifically, the FWHM at 10 °C is 34 nm, increasing to 35 nm at 0 °C. Similarly, at -20 °C, the FWHM is 32 nm, but it widens to 33 nm at -30 °C. Overall, the FWHM decreases from 38 nm at 20 °C to 23 nm at -125 °C, indicating a total narrowing of 15 nm (fig. 3.14).

3.2.3 Comparison of The Open-Circuit Photoluminescence Results Between $MAPbI_3$ and Triple Cation-Based Devices

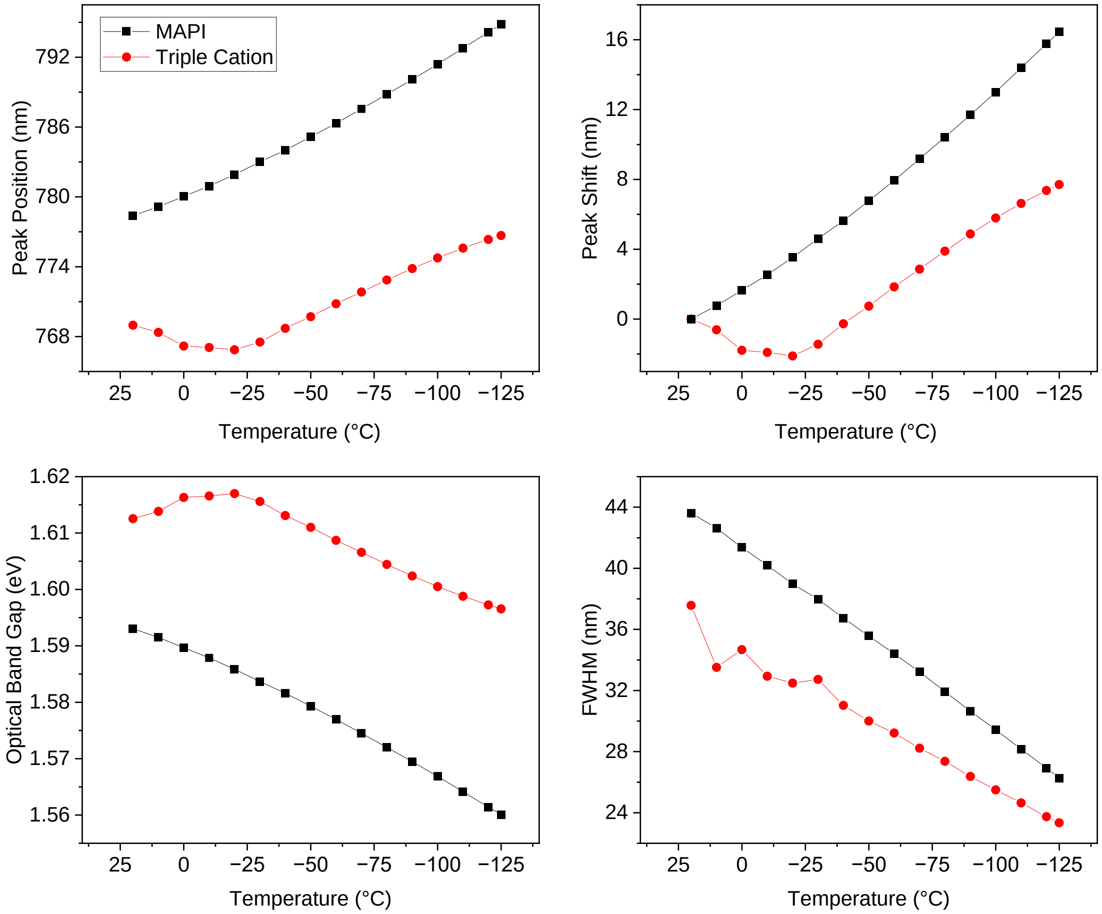

Figure 3. 15: comparison of the peak position, peak shift, optical band gap and the FWHM of the $MAPbI_3$ (black line) and triple cation-based (red line) devices.

When comparing the open-circuit PL results of MAPI and triple cation-based devices, several key differences and similarities are evident. The MAPI device exhibits a red shift in PL emission from 778 nm at 20 °C to 795 nm at -125 °C, resulting in a total shift of 17 nm. Conversely, the triple cation-based device initially blue shift, from 769 nm to 767 nm with temperature decreasing from 20 °C to -40 °C, before transitioning to a red shift. Overall, the PL peak of triple cation shifts from 769 nm at 20 °C to 777 nm at -125 °C, a total shift of 8 nm, which is notably smaller than that of MAPI (fig. 3.15). This difference in behaviour can be attributed to the enhanced thermal and structural stability of triple cation perovskites compared to single cation $MAPbI_3$ [30]. The larger shift and more substantial narrowing effect observed with temperature change in the MAPI device, compared to the triple cation device, are likely due to several factors. These factors include more significant lattice contraction, stronger electron−phonon coupling [31] and a more dynamic band structure with higher defect density, which makes the high-energy states more responsive to temperature variations [32].

For the optical band gap, MAPI exhibits a decrease from 1.59 eV at 20 °C to 1.56 eV at -125 °C. In contrast, the triple cation device demonstrates a higher band gap, starting at 1.61 eV at 20 °C and ending at 1.60 eV at -125 °C. Thus, the optical band gap of the triple cation device remains higher at each temperature step, which aligns with the typical values reported for triple cation perovskites ($E_g \sim 1.6$ eV) as documented by Ma *et al.* [33], compared to MAPI ($E_g \sim 1.56$ eV) as noted by Miah *et al.* [34].

Regarding the full width at half maximum of the photoluminescence peak, MAPI shows a significant decrease with temperature, from 44 nm at 20 °C to 26 nm at -125 °C, resulting in an 18 nm narrowing. In comparison, the triple cation PSC maintains a narrower FWHM throughout the entire temperature range, starting at 38 nm at 20 °C and reducing to 23 nm at -125 °C, resulting in a 15 nm narrowing. This indicates that while both materials exhibit a narrowing of the FWHM with decreasing temperature, MAPI experiences a more pronounced change.

3.2.4 Comparison of Short-Circuit Photoluminescence Results Between $MAPbI_3$ and Triple Cation-Based Devices

We conducted temperature-dependent photoluminescence spectroscopy under short-circuit (SC) conditions. In open-circuit conditions, the charge carriers cannot be extracted because there is no external path for them to move towards the electrodes, therefore all carriers must recombine within the device. As a result, the PL intensity in open-circuit conditions reflects the number of carriers that recombine radiatively but does not indicate how many carriers are available for actual device operation. On the other hand, in SC conditions, carriers are extracted from the device, which means fewer carriers are available to recombine radiatively.

By applying a short-circuit condition, we force the charge carriers generated in the perovskite layer by light absorption to move towards the electrodes. This allows us to study how efficiently these carriers are extracted from the perovskite layer. Since carriers are actively extracted during PL_{SC} measurements, we can infer the lifetime of these carriers (how long they exist before recombining) and their transport properties (how well they move through the perovskite material) [35].

Devices were connected to a lock-in amplifier to allow for charge extraction. To capture the PL spectra of a perovskite film at extreme Martian temperatures, the sample was kept in a liquid-nitrogen-cooled stage with measurements taken just like in thermal stepping – 10 °C intervals at a temperature range of 20 to -125 °C.

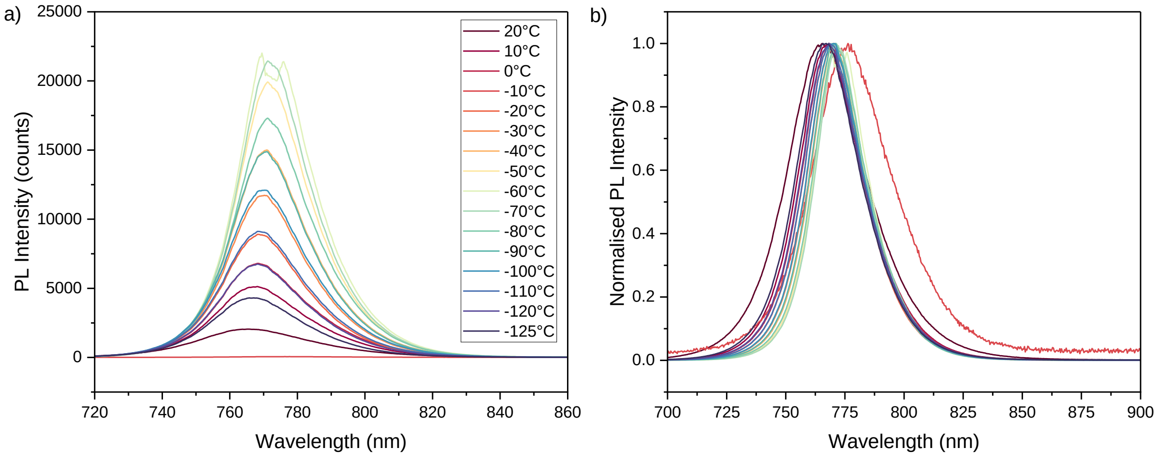

Figure 3. 16*:* a) PL peaks of MAPI-based device; b) normalized PL peaks of $MAPbI_3$-based device.

The PL peak position of the $MAPbI_3$-based device shows notable variations with temperature changes, as depicted in figure 3.16a. At 20 °C, the PL peak is initially positioned at 765.5 nm. As the temperature decreases, the PL peak undergoes a red shift, reaching 771.2 nm at -80 °C, but at -60 °C, there is a slight blue shift to 769.5 nm, which can be attributed to signal saturation, evidenced by the presence of multiple peaks. Beyond

-80 °C, the PL peak begins to blue shift, resulting in a peak position of 767.2 nm at -125 °C, as shown in fig. 3.16b. This blue shift observed at temperatures below -80 °C is only guessed to have occured due to the structural transition of $MAPbI_3$ from the tetragonal to the orthorhombic phase, known to occur around 162 K (approximately -111.15 °C), despite the shift beginning slightly before this transition temperature. Interestingly, we did not observe such behaviour during PL_{OC} measurement, which could be caused by using a $MAPbI_3$ device from a different batch. It is important to note that anomalous measurements were recorded at -10 °C and -60 °C, and these data points should be excluded from the analysis due to their inconsistency.

In contrast, the PL peak of the triple cation perovskite device starts at 765.5 nm at 20 °C and red shifts continuously to 771.2 nm at -120 °C, as illustrated in figure 3.17b. However, at -10 °C, 20 °C, and -125 °C, there are minor blue shifts, possibly due to faulty readings. Like $MAPbI_3$ at -60 °C, the triple cation device experiences signal saturation at -125 °C (fig. 3.17a). Campanari *et al.* [35] discussed that with time, fewer carriers are extracted from the device, resulting in an increase in PL intensity. This happens because more carriers end up recombining inside the device instead of being extracted. The reduced efficiency in carrier extraction over time can be attributed to the buildup of ions at the interfaces between the perovskite layer and the transport layers. These accumulated ions create an electric potential that opposes the extraction of carriers, thereby hindering the process [35].

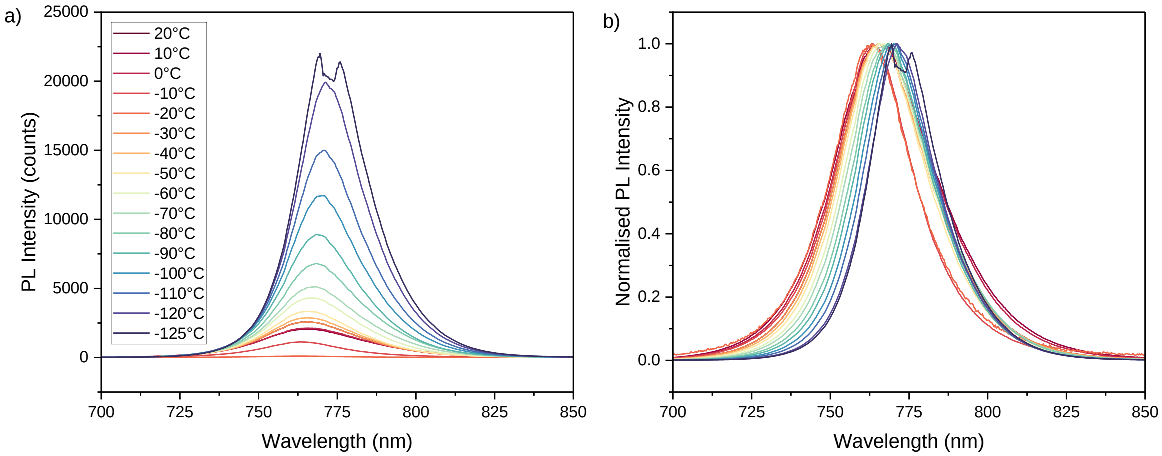

Figure 3. 17: a) PL peaks of triple cation-based device; b) normalized PL peaks of triple cation-based device.

The optical band gap of the $MAPbI_3$ device remains remarkably stable across the temperature range, varying slightly from 1.62 eV at -20 °C to 1.616 eV at -125 °C (or 1.597 eV including the measurement at -10 °C). For the triple cation device, the band gap also demonstrates stability, ranging from 1.619 eV at 20 °C to 1.611 eV at -125 °C, with a slight overall decrease as temperature decreases. These values are detailed in figure 3.18.

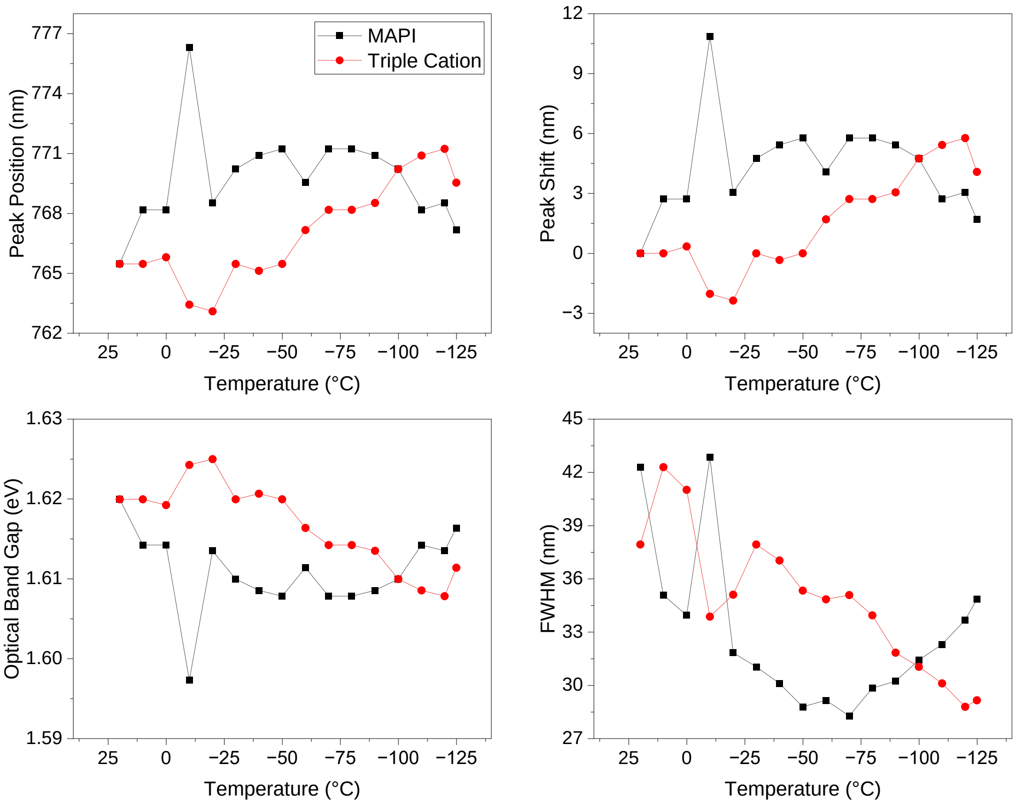

Figure 3. 18: Peak position, peak shift, optical band gap and the FWHM of $MAPbI_3$ and triple cation-based devices.

The FWHM of the $MAPbI_3$ PL peak decreases from 42 nm at 20 °C to 28 nm at -70 °C, before increasing to 35 nm at -125 °C. Conversely, the triple cation device shows slightly more volatility in FWHM. Starting at 38 nm at 20 °C, it rises to 42 nm at 10 °C, then sharply falls to 34 nm at -10 °C. This is followed by an increase to 38 nm at -30 °C, and a steadier decline to 29 nm at -125 °C.

$MAPbI_3$ devices show notable red and blue shifts in PL peak positions, which might be correlated with structural transitions and potential measurement anomalies. The optical band gaps of both devices exhibit stability across the temperature range, although the triple cation device shows a slight overall decrease. The FWHM analysis indicates a more consistent narrowing for $MAPbI_3$, whereas the triple cation device displays greater volatility.

Conclusion

In summary, triple cation-based devices outperform the $MAPbI_3$-based devices in the temperature range of 20 °C to -50 °C in PCE, V_{OC}, FF, and J_{SC} under the Martian thermal conditions (0.4 sun AM0, 0.5 mbar vacuum), however, at temperatures below -50 °C, $MAPbI_3$ devices exhibit superior performance, with lower degradation rates, indicating enhanced stability in extreme cold environments.

Both $MAPbI_3$ and triple cation devices display temperature-dependent shifts in photoluminescence emission and optical band gap, with $MAPbI_3$ showing a more pronounced red shift and a greater reduction in full width at half maximum, suggesting increased charge recombination. In contrast, triple cation devices maintain a more stable band gap, which may confer advantages in thermal stability and efficiency under varying thermal conditions. These results underscore the considerable influence of material composition on the optical and electronic properties of perovskite devices.

Whilst, due to the inconsistencies of short-circuit photoluminescence results, limited measurements, and the scarcity of related literature, a conclusive explanation cannot be drawn.

Further research is essential to better understand the mechanisms underlying the observed stability differences under Martian environmental conditions, particularly at lower temperatures. Additionally, optimizing perovskite-interlayer interfaces and adding interlayers could potentially further enhance device performance for Martian and deep-space applications. Moreover, the decrease in open-circuit voltage with temperature should be investigated, as it opposes other research results.

References

1. Barbé J, Pockett A, Stoichkov V, Hughes D, Lee HK, Carnie M, Watson T, Tsoi WC. In situ investigation of perovskite solar cells' efficiency and stability in a mimic stratospheric environment for high-altitude pseudo-satellites. Journal of Materials Chemistry C. 2020;8(5):1715-21
2. Sharp T, Gordon J. What is the temperature on Mars? Space.com. 2022 Feb 25. [Internet]. Available from: https://www.space.com/16907-what-is-the-temperature-of-mars.html
3. Shao S, Liu J, Fang HH, Qiu L, ten Brink GH, Hummelen JC, Koster LJ, Loi MA. Efficient perovskite solar cells over a broad temperature window: the role of the charge carrier extraction. Advanced Energy Materials. 2017 Nov;7(22):1701305.
4. Sun M, Zheng Y, Shi Y, Zhang G, Shao Y. Low-intensity–low-temperature stability assessment of perovskite solar cells operating on simulated Martian surface conditions. Physical Chemistry Chemical Physics. 2022;24(29):17716-22
5. Zhou Q, Wang B, Meng R, Zhou J, Xie S, Zhang X, Wang J, Yue S, Qin B, Zhou H, Zhang Y. Understanding temperature-dependent charge extraction and trapping in perovskite solar cells. Advanced Functional Materials. 2020 May;30(22):2000550.
6. Jacobsson TJ, Tress W, Correa-Baena JP, Edvinsson T, Hagfeldt A. Room temperature as a goldilocks environment for CH3NH3PbI3 perovskite solar cells: the importance of temperature on device performance. The Journal of Physical Chemistry C. 2016 Jun 2;120(21):11382-93.
7. Qiu W, Wu Y, Wang Y, Yang Z, Yang R, Zhang C, Hao Y, Hao Y. Low-temperature robust MAPbI3 perovskite solar cells with power conversion efficiency exceeding 22.4%. Chemical Engineering Journal. 2023 Jul 15;468:143656.
8. Gao F, Tress W, Wang J, Inganäs O. Temperature dependence of charge carrier generation in organic photovoltaics. Physical review letters. 2015 Mar 27;114(12):128701.
9. Chen B, Peng J, Shen H, Duong T, Walter D, Johnston S, Al-Jassim MM, Weber KJ, White TP, Catchpole KR, Macdonald D. Imaging spatial variations of optical bandgaps in perovskite solar cells. Advanced Energy Materials. 2019 Feb;9(7):1802790.
10. Wu N, Wu Y, Walter D, Shen H, Duong T, Grant D, Barugkin C, Fu X, Peng J, White T, Catchpole K. Identifying the cause of voltage and fill factor losses in perovskite solar cells by using luminescence measurements. Energy Technology. 2017 Oct;5(10):1827-35
11. Hoang MT, Yang Y, Tuten B, Wang H. Are metal halide perovskite solar cells ready for space applications? The journal of physical chemistry letters. 2022 Mar 25;13(13):2908-20
12. Qin C, Matsushima T, Fujihara T, Potscavage Jr WJ, Adachi C. Degradation mechanisms of solution-processed planar perovskite solar cells: thermally

stimulated current measurement for analysis of carrier traps. Advanced Materials. 2016 Jan;28(3):466-71

13. Zhang H, Qiao X, Shen Y, Moehl T, Zakeeruddin SM, Grätzel M, Wang M. Photovoltaic behaviour of lead methylammonium triiodide perovskite solar cells down to 80 K. Journal of Materials Chemistry A. 2015;3(22):11762-7
14. O'Kane M. Interpreting J-V Curves: Insights into Solar Cell Performance [Internet]. Ossila. Available from: https://www.ossila.com/pages/troubleshooting-solar-cell-iv-curves
15. Habisreutinger SN, Noel NK, Snaith HJ. Hysteresis index: A figure without merit for quantifying hysteresis in perovskite solar cells. ACS Energy Letters. 2018 Sep 19;3(10):2472-6
16. Colenbrander T, Peng J, Wu Y, Kelzenberg M, Huang JS, MacFarland C, Thorbourn D, Kowalczyk R, Kim W, Brophy J, Bui AD. Low-intensity low-temperature analysis of perovskite solar cells for deep space applications. Energy Advances. 2023;2(2):298-307
17. Tu Y, Wu J, Xu G, Yang X, Cai R, Gong Q, Zhu R, Huang W. Perovskite solar cells for space applications: progress and challenges. Advanced Materials. 2021 May;33(21):2006545
18. Brown CR, Eperon GE, Whiteside VR, Sellers IR. An Assessment of Perovskite Solar Cells for Low-Intensity-Low-Temperature (LILT) Space Missions. In2019 IEEE 46th Photovoltaic Specialists Conference (PVSC) 2019 Jun 16 (pp. 2374-2376)
19. Liu Y, Lu H, Niu J, Zhang H, Lou S, Gao C, Zhan Y, Zhang X, Jin Q, Zheng L. Temperature-dependent photoluminescence spectra and decay dynamics of MAPbBr3 and MAPbI3 thin films. AIP Advances. 2018 Sep 1;8(9).
20. Naghadeh SB, Sarang S, Brewer A, Allen AL, Chiu YH, Hsu YJ, Wu JY, Ghosh S, Zhang JZ. Size and temperature dependence of photoluminescence of hybrid perovskite nanocrystals. The Journal of Chemical Physics. 2019 Oct 21;151(15)
21. Barugkin C, Cong J, Duong T, Rahman S, Nguyen HT, Macdonald D, White TP, Catchpole KR. Ultralow absorption coefficient and temperature dependence of radiative recombination of CH3NH3PbI3 perovskite from photoluminescence. The journal of physical chemistry letters. 2015 Mar 5;6(5):767-72
22. Tombe S, Adam G, Heilbrunner H, Apaydin DH, Ulbricht C, Sariciftci NS, Arendse CJ, Iwuoha E, Scharber MC. Optical and electronic properties of mixed halide (X= I, Cl, Br) methylammonium lead perovskite solar cells. Journal of Materials Chemistry C. 2017;5(7):1714-23
23. Kong W, Ye Z, Qi Z, Zhang B, Wang M, Rahimi-Iman A, Wu H. Characterization of an abnormal photoluminescence behavior upon crystal-phase transition of perovskite CH 3 NH 3 PbI 3. Physical Chemistry Chemical Physics. 2015;17(25):16405-11
24. Wright AD, Verdi C, Milot RL, Eperon GE, Pérez-Osorio MA, Snaith HJ, Giustino F, Johnston MB, Herz LM. Electron–phonon coupling in hybrid lead halide perovskites. Nature communications. 2016 May 26;7(1):11755
25. Shao Z, You S, Guo X, Xiao J, Liu J, Song F, Xie H, Sun J, Huang H. Temperature-dependent photoluminescence of Co-evaporated MAPbI3 ultrathin films. Results in Physics. 2022 Mar 1;34:105326

26. Dar MI, Jacopin G, Meloni S, Mattoni A, Arora N, Boziki A, Zakeeruddin SM, Rothlisberger U, Grätzel M. Origin of unusual bandgap shift and dual emission in organic-inorganic lead halide perovskites. Science advances. 2016 Oct 28;2(10):e1601156
27. Francisco-López A, Charles B, Weber OJ, Alonso MI, Garriga M, Campoy-Quiles M, Weller MT, Goñi AR. Equal footing of thermal expansion and electron–phonon interaction in the temperature dependence of lead halide perovskite band gaps. The Journal of Physical Chemistry Letters. 2019 May 15;10(11):2971-7
28. Wei K, Xu Z, Chen R, Zheng X, Cheng X, Jiang T. Temperature-dependent excitonic photoluminescence excited by two-photon absorption in perovskite CsPbBr 3 quantum dots. Optics letters. 2016 Aug 15;41(16):3821-4
29. Afshord AZ, Uzuner BE, Soltanpoor W, Sedani SH, Aernouts T, Gunbas G, Kuang Y, Yerci S. Efficient and Stable Inverted Wide-Bandgap Perovskite Solar Cells and Modules Enabled by Hybrid Evaporation-Solution Method. Advanced Functional Materials. 2023 Aug;33(31):2301695
30. Kranthiraja K, Parashar M, Mehta RK, Aryal S, Temsal M, Kaul AB. Stability and degradation in triple cation and methyl ammonium lead iodide perovskite solar cells mediated via Au and Ag electrodes. Scientific Reports. 2022 Nov 3;12(1):18574
31. Saidi WA, Poncé S, Monserrat B. Temperature dependence of the energy levels of methylammonium lead iodide perovskite from first-principles. The Journal of Physical Chemistry Letters. 2016 Dec 15;7(24):5247-52
32. Panzer F, Li C, Meier T, Köhler A, Huettner S. Impact of structural dynamics on the optical properties of methylammonium lead iodide perovskites. Advanced Energy Materials. 2017 Aug;7(16):1700286
33. Ma K, Atapattu HR, Zhao Q, Gao Y, Finkenauer BP, Wang K, Chen K, Park SM, Coffey AH, Zhu C, Huang L. Multifunctional conjugated ligand engineering for stable and efficient perovskite solar cells. Advanced materials. 2021 Aug;33(32):2100791
34. Miah MH, Khandaker MU, Rahman MB, Nur-E-Alam M, Islam MA. Band gap tuning of perovskite solar cells for enhancing the efficiency and stability: issues and prospects. RSC advances. 2024;14(23):15876-906
35. Campanari V, Martelli F, Agresti A, Pescetelli S, Nia NY, Di Giacomo F, Catone D, O'Keeffe P, Turchini S, Yang B, Suo J. Reevaluation of photoluminescence intensity as an indicator of efficiency in perovskite solar cells. Solar RRL. 2022 Aug;6(8):2200049

Chapter 4: Cyclic Temperature Stability and Jezero Crater Thermal Profile Matching

This chapter investigates the performance and stability of methylammonium lead iodide ($MAPbI_3$) and triple cation ($Cs_{0.05}(MA_{0.17}FA_{0.83})_{0.95}Pb(I_{0.17}Br_{0.13})_3$) perovskite solar cells under conditions simulating extreme Martian thermal cycling and the day-night temperature variations of Jezero Crater. The thermal cycling section examines how repeated temperature changes from 20 °C to -125 °C affect key performance metrics, while the Jezero Crater profile analyses the performance of $MAPbI_3$ and triple cation solar cells over a simulated 24-hour Martian day.

The results demonstrate that triple cation perovskite solar cells consistently outperform $MAPbI_3$ cells in both efficiency and stability across the tested conditions. During thermal cycling from 20 °C to -125 °C, $MAPbI_3$-based devices exhibit greater degradation, particularly in fill factor, compared to the more stable triple cation cells. Likewise, during the simulated Jezero Crater day-night cycle, triple cation devices maintain superior performance, though both device types experience substantial degradation – significantly higher than that observed in previous thermal stepping experiments.

4.1 Thermal Cycling

4.1.1 Ice Formation During Thermal Cycling

Initial measurements were to be conducted under 0.4 AM0 intensity and a 6.1 mbar vacuum to simulate the extreme temperatures and pressure of the Martian environment. However, it was soon observed that maintaining a 6.1 mbar vacuum at extremely low temperatures led to ice formation on the devices within the environment chamber. An example of this phenomenon during thermal cycling on a $MAPbI_3$ device is illustrated in figure 4.1. The figure presents a series of images illustrating the condition of the perovskite solar cell after exposure to thermal cycling, specifically focusing on ice formation and its subsequent dissipation at room temperature. Firstly, in figure 4.1a, the device is depicted immediately after removal from the environmental chamber, showing significant ice coverage on the surface. This ice coverage is a direct consequence of the exposure to temperatures cycling between 20 °C and -125 °C, which leads to condensation and freezing of moisture on the devices. Secondly, in figure 4.1b, the device is shown after being at room temperature for 5 minutes. The image reveals a partial reduction in ice coverage, indicating the beginning of the melting process as the device adjusts to the ambient temperature. Thirdly, in figure 4.1c, taken after 10 minutes at room temperature, the ice has completely melted, and the device surface appears free of ice or water.

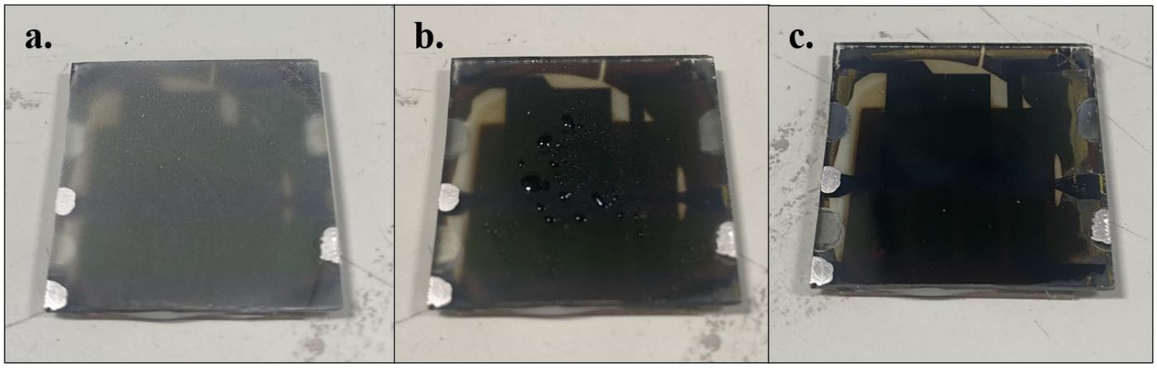

Figure 4. 1: a) device exhibiting ice coverage immediately upon removal from the environmental chamber; b) device after 5 minutes at room temperature; c) device after 10 minutes at room temperature.

As illustrated in fig. 4.2, initially, the PCE was measured at 12.97%. After 2 cycles of thermal cycling, it decreased to 11.53%. After 4 cycles, a substantial drop to 3.77% was noted, indicating severe degradation. The PCE further decreased to 2.24% after 7 cycles and slightly recovered to 2.45% after 11 cycles. This represents an 81% reduction in PCE compared to the initial measurement.

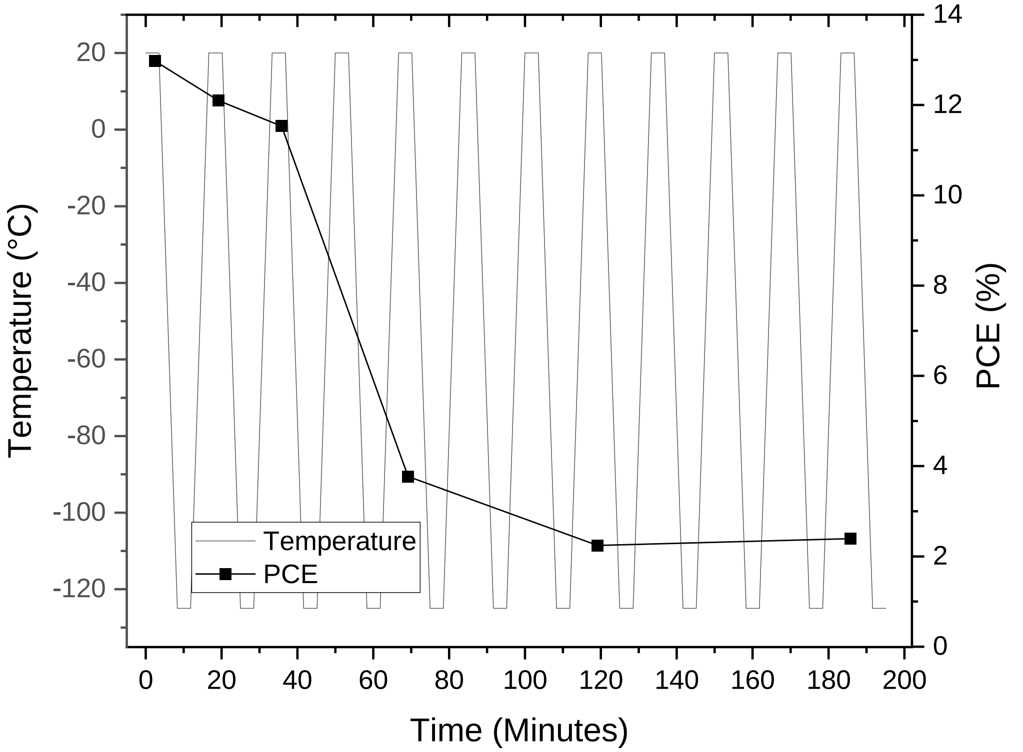

Figure 4. 2: PCE as a function of thermal cycle of $MAPbI_3$-based device subjected to ice formation at 6.1 mbar.

The FF decreased from an initial 66.08% to 43.60% after 11 cycles, corresponding to a 35% reduction in FF (fig. 4.3). J_{SC} decreased from 11.89 mA/cm² initially to 2.39 mA/cm² after 11 cycles. V_{OC} remained relatively stable throughout the cycling, decreasing only slightly from 1.04 V initially to 1.02 V after 11 cycles (a decrease of 1.92%). This minor change indicates that the ability of the device to maintain V_{OC} was less affected compared to PCE, FF, and J_{SC}, which are more sensitive to ice formation. These results are all attributed to ice formation on the device surface during exposure to low temperatures and were most likely caused by a combination of compromised charge carrier collection, decreased transport efficiency, reduced light absorption or hindered charge extraction.

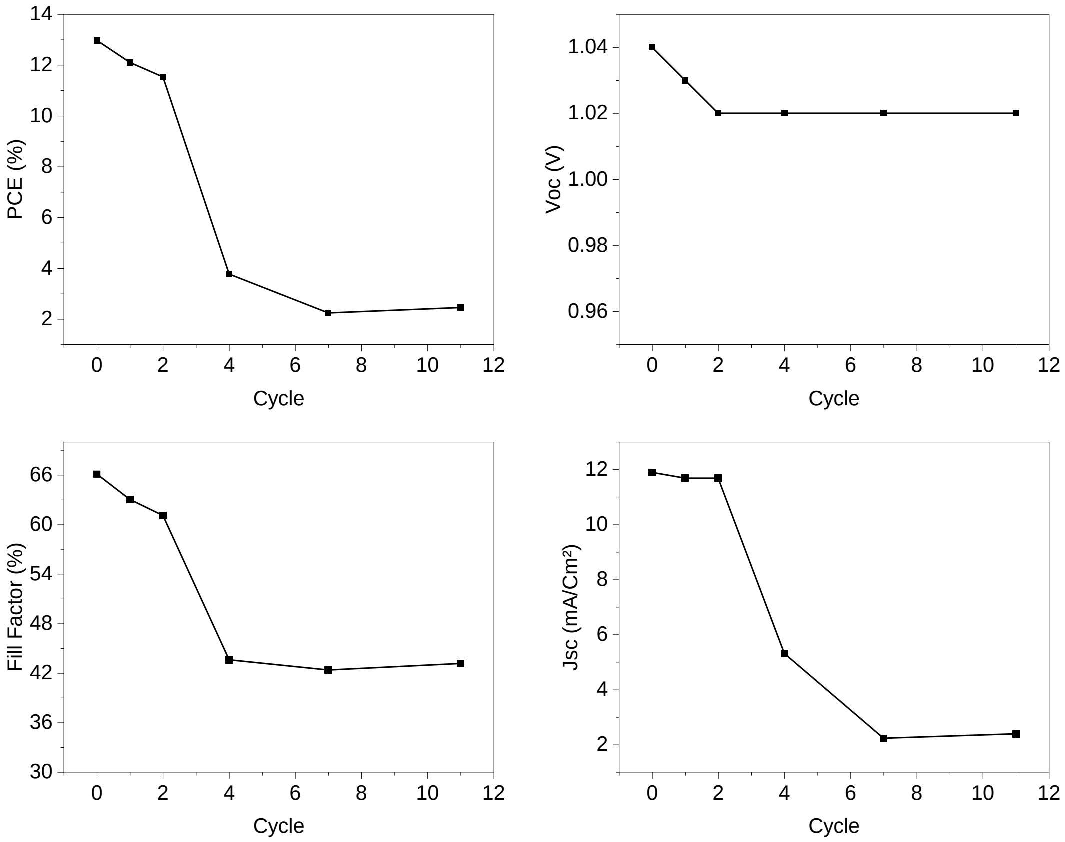

Figure 4. 3: PCE, V_{OC}, FF, J_{SC}, as a function of thermal cycle of the $MAPbI_3$-based device subjected to ice formation at 6.1 mbar.

Consequently, all subsequent thermal measurements, including thermal cycling, thermal stepping, and temperature profiling, were conducted at a reduced vacuum pressure of 0.5 mbar to mitigate ice formation. While the possibility of ice formation on solar cells on Mars exists due to the low temperatures, data from the Curiosity and Opportunity rovers indicate that dust accumulation has been a more prominent issue, with no significant ice-related problems reported. The extremely low humidity and atmospheric pressure on Mars reduce the likelihood of substantial ice formation. Nevertheless, to maintain the long-term efficiency of solar cells, it could be beneficial to implement strategies to suppress the effect of ice and dust, such as surface coatings, heating elements, and mechanical cleaning systems.

4.1.2 Comparison of Thermal Cycling Results Between MAPbI$_3$ and Triple Cation-Based Devices

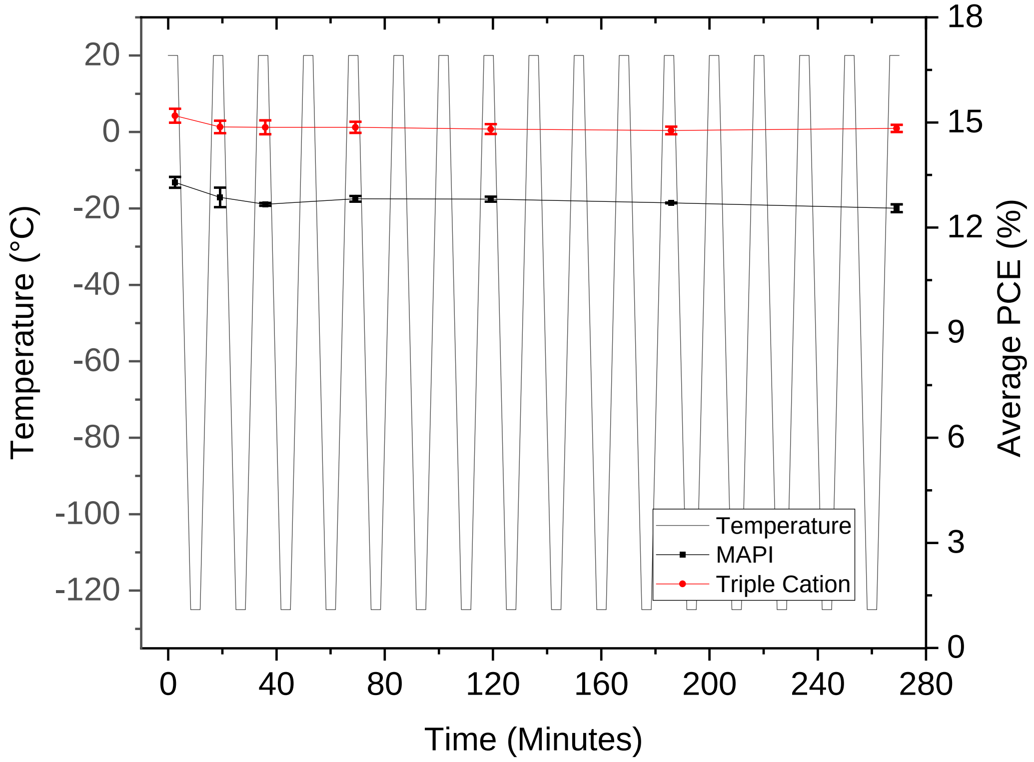

Figure 4. 4: Average power conversion efficiency as a function of thermal cycles for two MAPbI$_3$-based devices and two triple cation-based devices, including error bars representing the standard deviation.

As seen in figure 4.4, for MAPbI$_3$-based devices (to discern overarching patterns, an average of successful thermal cycling measurements was analysed and graphically represented), the initial PCE is 13.29%. With each thermal cycle the PCE decreases at a small rate and after the 16 cycles with a final PCE of 12.55%. The triple cation-based cells exhibit a significantly higher initial PCE of 15.19%. Similarly, it also has a slow PCE decrease rate – after 16 cycles the final PCE is 14.83%. MAPbI$_3$ PSCs maintain 94.4% of its initial PCE after 16 cycles. The triple cation-based devices maintain slightly more – 97.7% of its initial PCE after the same number of cycles. The results show that both MAPbI$_3$ and triple cation-based devices have good stability under extreme temperature cycling, though there is slight degradation. It provides further significant support that the large reduction in PCE at lower temperatures is not due to permanent chemical degradation, and likely due to structural/physical change which is reversible after heating back to 20 °C. McGehee *et al*. [1] demonstrated that an encapsulant with a low elastic modulus enables dissipation of strain more efficiently and results in much higher mechanical stability than encapsulants with stiffer ionomers, like Surlyn for example. Similarly, it is thought that the polyimide tape used here between the perovskite cell and the epoxy can release strain during temperature variations and improves the operational stability of the cell.

A perovskite solar cell stack has multiple interfaces that could lead to mechanical failure during temperature cycling because of the different thermal expansion coefficients of the layers [2]. The slight PCE reduction may be due to the thermally induced mechanical degradation after several cycles. Particularly, it has been emphasized by other researchers [3] that the mismatched thermal expansion coefficients of the different layers and low fracture energy of PSCs can cause interfacial defects responsible for the deterioration in the photovoltaic performance. On top of that, Yang *et al*. proposed that when the thermal expansion coefficients of neighbouring layers in PSCs are mismatched, thermal stressing can result in cracking, which significantly affects the performance of the solar cells [3].

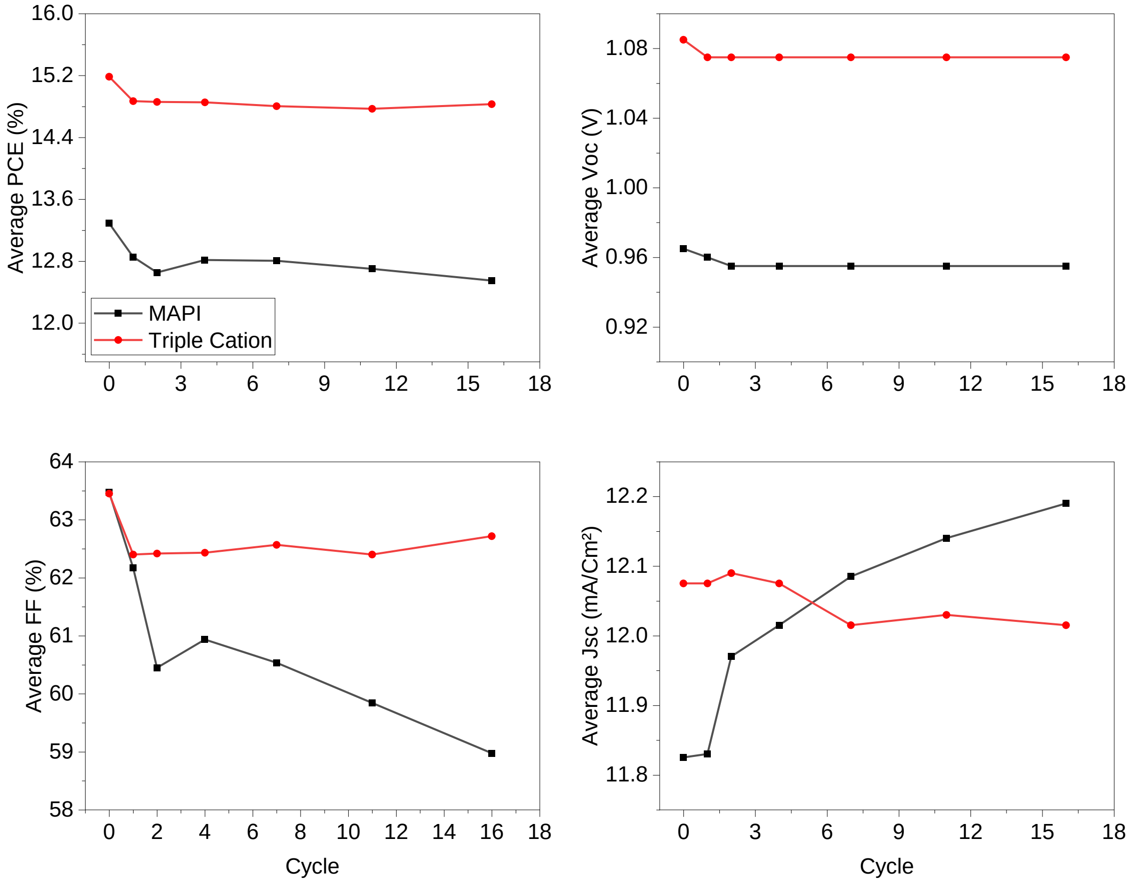

Figure 4. 5: Average PCE, V_{OC}, FF, J_{SC}, as a function of thermal cycle of the $MAPbI_3$-based devices and the triple cation-based devices.

Figure 4.5 illustrates PCE, V_{OC}, FF, and J_{SC} as a function of thermal cycling for $MAPbI_3$-based devices and triple cation-based devices. The V_{OC} of $MAPbI_3$ cells decreased slightly from 0.965 V at the initial measurement to 0.955 V after 16 cycles – a percentage change of -1.04% in that period. The triple cation cells exhibited a similar small decrease in V_{OC} from 1.09 V to 1.08 V, corresponding to a percentage change of -0.92%. Both PSC types show a slight decrease in V_{OC}, but on average, triple cation devices demonstrated marginally better stability.

The fill factor is the primary parameter responsible for the slight degradation in the PCE of $MAPbI_3$ and triple cation-based devices under thermal cycling. The FF of $MAPbI_3$ PSCs declined from 63.48% to 58.98%, retaining ~93% of the initial value. In contrast, the initial

FF of triple cation-based PSCs is 0.025% lower than $MAPbI_3$, at 63.45%, with a significantly less pronounced reduction to 62.72% after 16 cycles, maintaining 98.8% of the initial value. This suggests that the FF of triple cation PSCs is significantly more stable compared to $MAPbI_3$ PSCs. FF is known to be particularly sensitive to parasitic loss mechanisms, such as charge transport losses and current leakage [4], which might have led to a reduced FF.

For J_{SC}, $MAPbI_3$-based devices exhibit an initial J_{SC} of 11.83 mA/cm^2, which, interestingly, increases slightly to 12.19 mA/cm^2 after 16 cycles, a 3% increase. Triple cation-based cells demonstrate a higher initial J_{SC} of 12.08 mA/cm^2, however, with a small overall decrease to 12.02 mA/cm^2 after thermal cycling – a percentage change of -0.5%. Like V_{OC}, this suggests that the reduction in PCE over 16 cycles is not due to changes in the J_{SC}.

Looking at the J-V curves (fig. 4.6), a mismatch, mostly caused by the increased J_{SC}, between initial and final (16th cycle) is clearly visible for $MAPbI_3$. Triple cation J-V curves on the other hand have barely changed. The approximate series resistance values from the J-V curve were calculated by taking the inverse of the A/V slope. $MAPbI_3$ series resistance increases from 86.37 Ω cm^2 after the initial measurement to 93.65 Ω cm^2 following the 16th cycle, marginal increase of 7.8%. Triple cation series resistance rises from 92.77 Ω cm^2 to 98.79 Ω cm^2 – a 6.6% increase. Therefore, it shows that series resistance contributes to the decrease of the performance after 16 cycles.

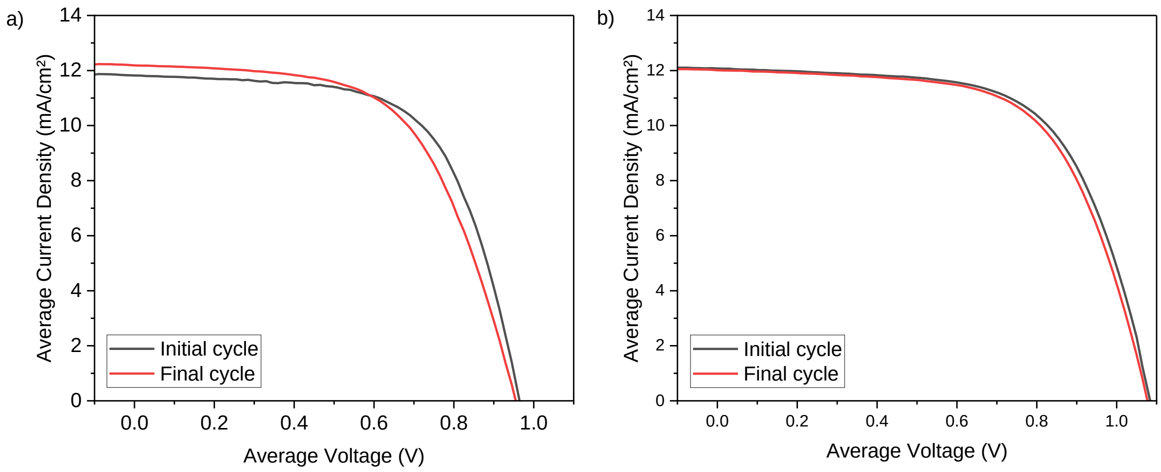

Figure 4. 6: the average of the J-V curves for (a) $MAPbI_3$-based devices; (b) Triple cation-based devices.

Huang *et al*. [5] discovered that with each illumination/dark cycle, the decrease in the recovery rate with successive cycles was harder and harder to achieve. Same results were reported by Sheikh *et al*. [6] – in their research, the slowdown in PCE recovery became particularly pronounced with an increase in the number of day/night cycles, indicating a direct correlation between cycle frequency and the degradation of the PSCs. Additionally, this effect was highly dependent on charge accumulation in the charge transfer layers. This kind of fatigue can also arise from thermal stresses caused by thermal cycling, during which the decay of the mechanical integrity is the main cause of the performance degradation, which remains poorly understood [7]. In figures 4.4 and 4.5, we observe that the PCE degrades minimally between cycles. However, thermal stepping measurements indicate that the PCE decreases by approximately 90% at -125 °C from its initial value, but, upon reheating, the PCE fully recovers or even exceeds its initial value. This suggests that the incomplete recovery of PCE observed in thermal cycling measurements may be due to thermal fatigue. Extending the ramp rate and prolonging the time at 20 °C could potentially enhance the recovery of the initial PCE.

Irreversible degradation mechanisms may involve the degradation of the perovskite photoactive layer, transport layers, and contacts, particularly due to interlayer ion diffusion. Temperature is a well-documented factor that contributes to the irreversible degradation of the perovskite layer. Photochemical decomposition of perovskite generally results in the formation of PbI_2 and a change in the sample colour to yellow [8]. Although we did not observe this yellowing after thermal cycling, slight yellowing was noted in the samples following thermal stepping.

4.2 Jezero Crater Temperature Profile

4.2.1 Jezero Crater Temperature Profile Measurement of The $MAPbI_3$-Based Device

Here we explore the performance of MAPI solar cells under simulated Martian day-night cycles at Jezero Crater. The experimental conditions were divided into four distinct phases for simplicity: night (00:00 - 06:00), sunrise to peak temperature (06:00 - 13:00), peak temperature to sunset (13:00 - 18:00), and evening (18:00 - 24:00). Temperature profile was mimicked using the data captured by NASA's Perseverance rover at Jezero Crater [9].

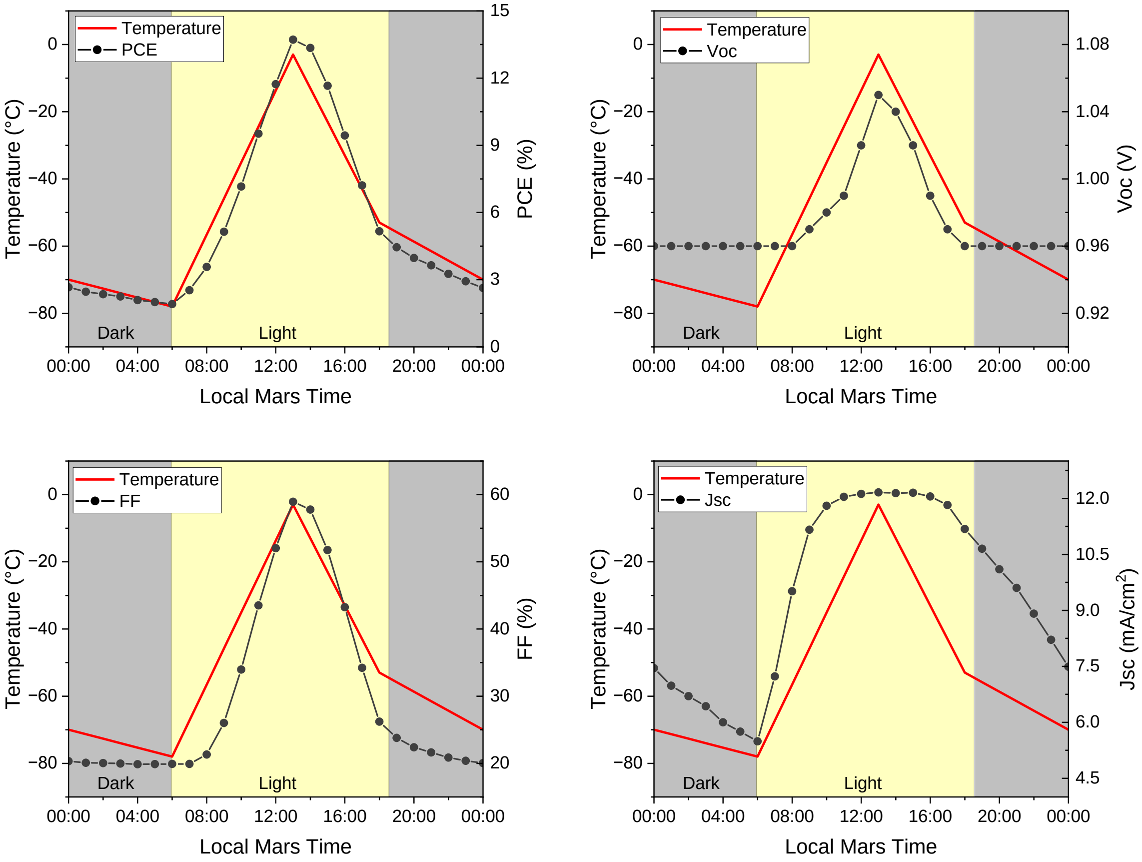

Figure 4. 7: PCE, V_{OC}, FF and J_{SC} of the $MAPbI_3$-based device during a simulated Martian day.

Figure 4.7 presents the PCE, V_{OC}, FF, and J_{SC} of a MAPI device, measured hourly from 00:00 to 24:00 during a simulated Martian day at Jezero Crater. These measurements are divided into four distinct stages (temperature change can be seen in supporting files – table S4.7 for $MAPbI_3$ and table S4.9 for triple cation):

1. 00:00 – 06:00: Night, no light, with temperature linearly decreasing from 70 °C to -78 °C.
2. 06:00 – 13:00: Sunrise to peak daily temperature, constant light, with temperature increasing linearly from -78 °C to -3 °C.
3. 13:00 – 18:00: Afternoon, constant light, with temperature linearly decreasing from -3 °C to -53 °C.

4. 18:00 – 24:00: Evening, sunset, no light, with temperature linearly decreasing from -53 °C to -70 °C.

It is important to note that at Jezero Crater on Mars, the periods from 00:00 to 06:00 and 18:00 to 24:00 represent the Martian night, during which solar irradiation is absent, resulting in zero power output from photovoltaic devices. Consequently, data collected during these simulated nighttime periods should be disregarded when analysing power generation. To approximate Martian night conditions, the testing chamber was covered during these intervals. However, the cover was removed during measurements to assess the performance of perovskite solar cells under low-temperature conditions and reduced temperature change rates.

At approximately 06:00, the simulated sunrise occurs, and the lamp is turned on until the simulated sunset at 18:00. During this period, the temperature increases, and the performance parameters significantly improve. The PCE rose from 1.91% to 13.72% at the peak temperature (13:00, -3 °C), marking a 618.2% increase. The V_{OC} increased from 0.96 V to 1.05 V, the FF tripled from 19.91% to 58.93%, and the J_{SC} increased from 5.49 to 12.16 mA/cm². This significant rise in performance parameters indicates the strong dependence of device efficiency on light exposure and favourable thermal conditions.

In the afternoon, as the temperature began to decline with the setting sun, the performance parameters also decreased. The PCE dropped from 13.72% to 5.16%, a percentage change of -62.4%. The V_{OC} returned to 0.96 V from 1.05 V, the FF nearly halved from 58.93% to 26.2%, and the J_{SC} slightly decreased from 12.16 to 11.18 mA/cm². This decline demonstrates the immediate effect of cooling on the performance of the solar cell, most likely caused by increased resistance, decreased charge carrier transport and extraction, change in recombination rates, just like during the thermal stepping measurements [10] [4] [11].

After the thermal stepping measurements, we anticipated an average percentage change of approximately 48% between 10 °C (average PCE = 12.43%) and -80 °C (average PCE =

6.5%). This discrepancy could be due to the slower temperature change rate during the temperature profile measurements (30 °C/min for stepping, as low as 0.1667 °C/min for temperature profile measurements), extended time at negative temperatures, bad device batch or other unknown factors. Consequently, further analysis is necessary to fully understand the behaviour of MAPI devices under Martian conditions.

The J-V curves measured the key times (midnight, sunrise, peak temperature and sunset) are shown in figure 4.8. Here it can be seen how different parameters determine the performance of the $MAPbI_3$ device during the hours. To begin, 00:00 and 24:00 J-V curves sit on top of each other, highlighting the overall long-term stability of this device – it returns basically exactly to where it started off, after the whole temperature variation and illumination. Just before sunrise, the coldest temperature is recorded ant the effects of it are seen in the decrease of J_{SC} mainly. From there, at 13:00 when the highest daily temperature is set, the J-V curve starts forming an S-shape, due to both, the increase in V_{OC} and J_{SC}. At sunset, the decreased temperature effects unveil themselves in a form of V_{OC} and slight J_{SC} decrease. From the curves, series and shunt resistances most likely had a significant impact on this behaviour.

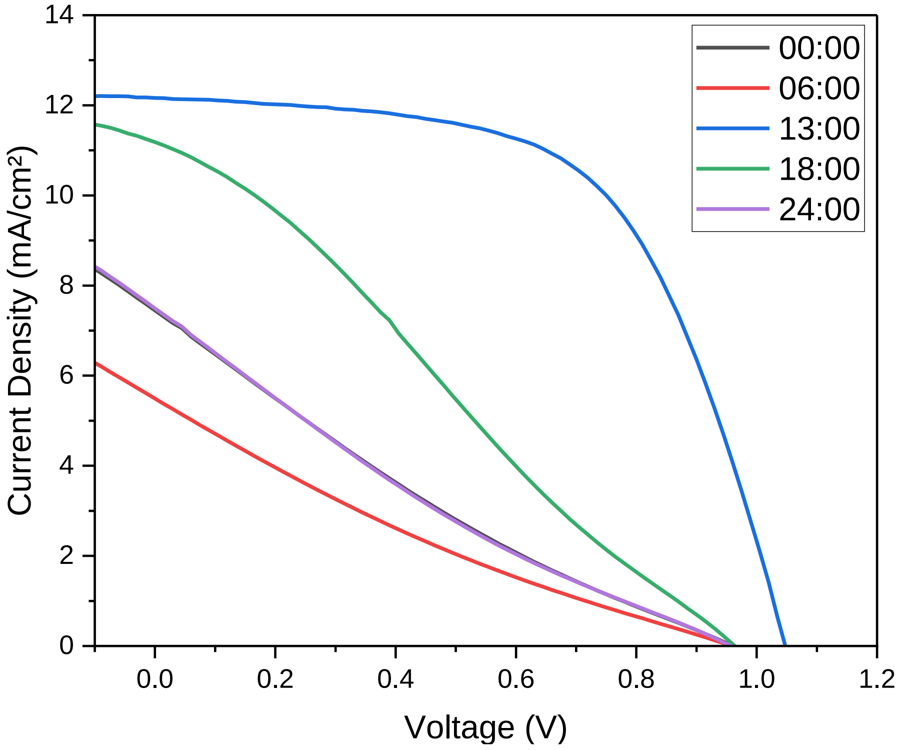

Figure 4. 8: J-V curves of the $MAPbI_3$-based device measured at 00:00, 6:00, 13:00, 18:00 and 24:00 during simulated Martian day.

These measurements illustrate the significant impact of temperature. It is important to note that these measurements were performed at 0.5 mbar instead of 6.1 mbar, with no dust present, and at an accelerated rate (3 hours instead of a full Martian day, which is approximately 24 hours and 40 minutes [12]). Therefore, further measurements that mimic the Martian day under more accurate conditions are required to fully understand the impact of these variables on the performance of the devices.

4.2.2 Jezero Crater Temperature Profile Measurement of The Triple Cation-Based Device

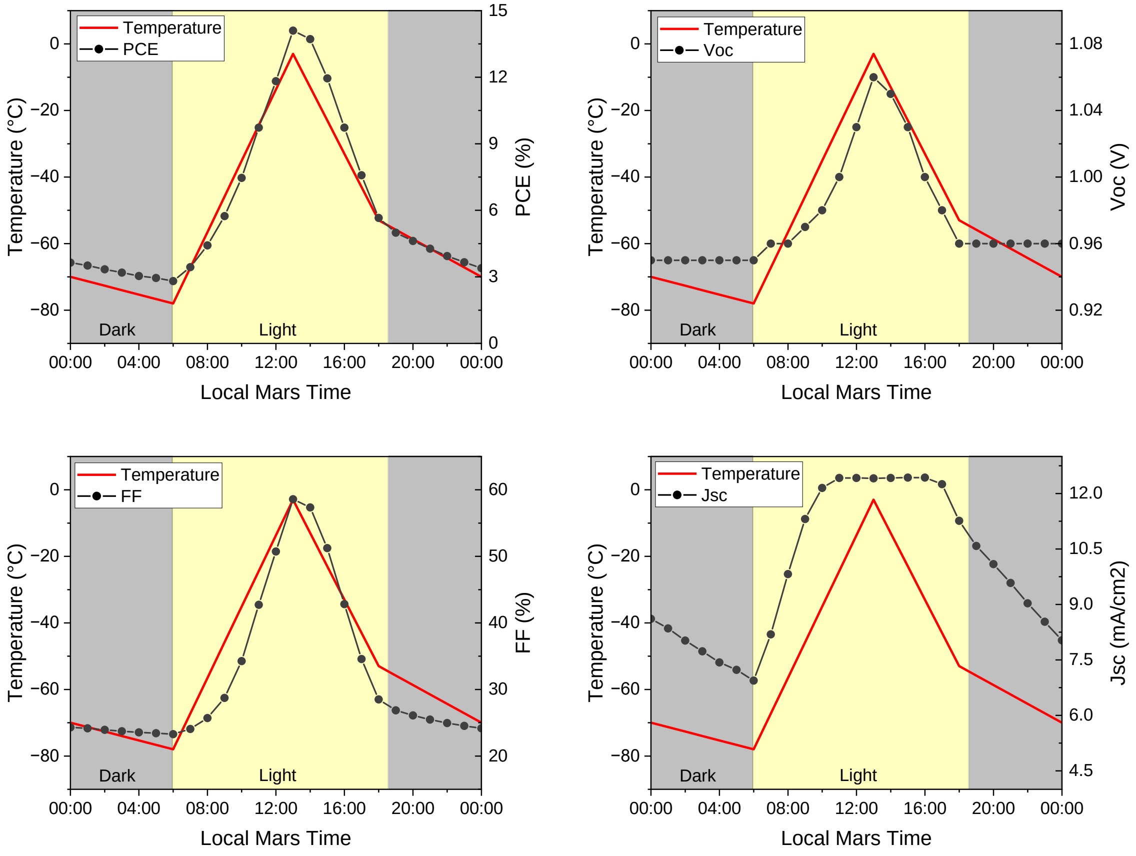

Figure 4. 9: PCE, V_{OC}, FF and J_{SC} of the triple cation-based device during a simulated Martian day.

Just like with $MAPbI_3$ PSCs, measurements obtained between 00:00 and 06:00, and between 18:00 and 24:00, should be disregarded.

Following the simulated sunrise at 06:00 (fig. 4.9), as the temperature increased, the performance parameters skyrocketed. The PCE rose from 2.81% to 14.1% at the peak temperature (-3°C at 13:00), an impressive increase of 401.4%. The V_{OC} increased from 0.95 V to 1.06 V, the FF surged from 23.27% to 58.58%, and the J_{SC} jumped from 6.94 to 12.41 mA/cm².

During the simulated afternoon (13:00 to 18:00), as the temperature began to decline with the setting sun, the performance parameters also decreased. The PCE dropped from 14.1% to 5.66%, a significant decrease of 59.9%. The V_{OC} fell from 1.06 V to 0.96 V, the FF diminished from 58.58% to 28.5%, and the J_{SC} slightly decreased from 12.41 to 11.26 mA/cm².

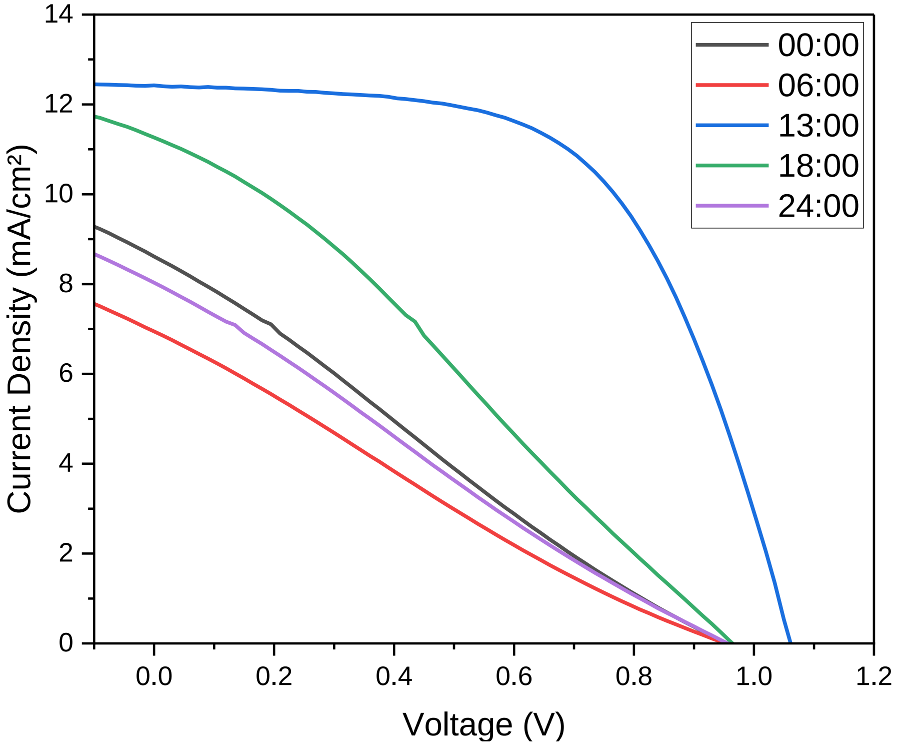

Figure 4. 10: J-V curves of the triple cation-based device measured at 00:00, 6:00, 13:00, 18:00 and 24:00 during simulated Martian day.

Figure 4.10 presents the J-V curves of the triple cation perovskite device, which closely resemble those of MAPI. However, unlike MAPI, a notable difference is observed between the two midnight J-V curves: the final curve at 24:00 sits below the initial curve at 00:00. This suggests a worse performance recovery for the triple cation device after one simulated Martian day cycle. In general, the J-V curves follow the same pattern as those of MAPI, with an S-shaped curve at peak temperature, indicated by the blue line, while the curves at lower temperatures appear more linear, reflecting the impact of reduced temperatures.

Just like MAPI, the performance parameters of the triple cation-based device during this measurement do not align well with the results of the thermal stepping measurements. This discrepancy highlights the need for further experiments and analysis to better understand these results.

4.2.3 Comparison of Jezero Crater Temperature Profile Results Between $MAPbI_3$ and Triple Cation-Based Devices

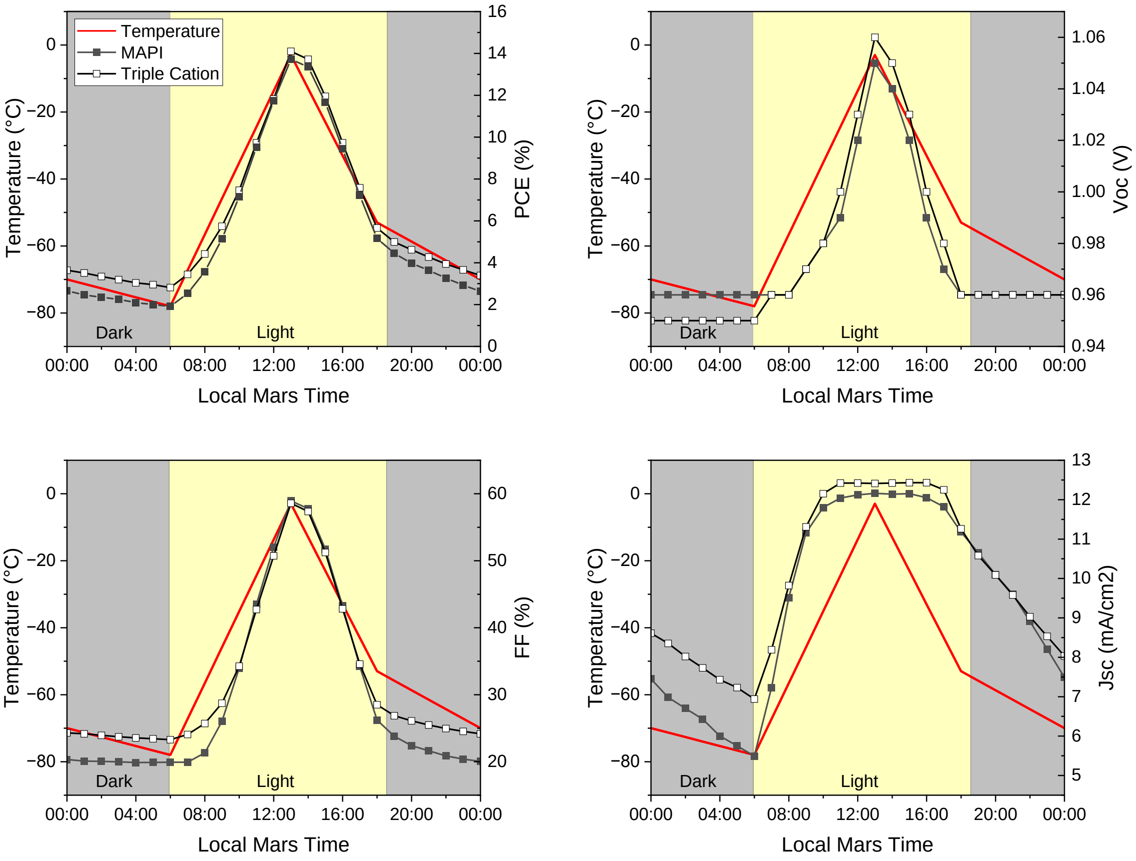

Figure 4. 11: Comparison of the PCE, V_{OC}, FF and J_{SC} of the $MAPbI_3$ and triple cation-based devices during a simulated Martian day.

During the night phase (00:00 (-70 °C) to 06:00 (-78 °C)), characterized by darkness and decreasing temperatures, both devices experience a reduction in PCE, indicative of the impact of thermal stress without illumination. The MAPI device starts with a PCE of 2.66%, which is slightly lower than the initial PCE of 3.64% for triple cation. However, MAPI device experiences a sharper decline to 1.91%, representing a decrease of 28.2%, while the PCE of triple cation decreases to 2.81%, a reduction of 22.8%. This is primarily attributed to the drop in J_{SC} for both devices: J_{SC} of MAPI falls from 7.45 mA/cm² at 00:00 to 5.49 mA/cm² at 06:00, while the J_{SC} of triple cation decreases from 8.61 mA/cm² to 6.94 mA/cm². In contrast, the V_{OC} remains constant for both devices, and the decrease in FF is minimal, from 20.32% to 19.91% for MAPI and from 24.29% to 23.27% for the triple cation. Interestingly, from figure 4.11 it is clear that the V_{OC} of MAPI is higher than that of triple cation from 00:00 to 06:00, with values of 0.96 V compared to 0.95 V, but after 06:00, the V_{OC} of triple cation matches or exceeds that of MAPI.

At sunrise and under constant light conditions (06:00 (-78 °C) to 13:00 (-3 °C)), as temperatures rise to a peak of -3 °C, both devices exhibit significant performance boost. However, triple cation perovskite outperforms MAPI in terms of PCE, achieving 14.1% compared to MAPI's 13.72%, but MAPI outperforms the triple cation in terms of PCE change (618% compared to 401%).

In the afternoon (13:00 (-3 °C) to 18:00 (-53 °C)), as temperatures gradually decrease, both devices experience a decline in PCE. The triple cation PSC exhibits a more substantial decrease from 14.1% to 5.66%, representing a reduction of 59.9%, compared to the drop of MAPI from 13.72% to 5.16%, a reduction of 62.4%.

During the evening and post-sunset phase (18:00 (-53 °C) to 24:00 (-70 °C)), the performance of both devices keeps falling. Triple cation PSC shows a more gradual decline in PCE from 5.66% to 3.39%, representing a reduction of 40.1%, compared to the drop of MAPI from 5.16% to 2.63%, a reduction of 49%. This reflects potentially enhanced stability of the triple cation under decreasing light and temperature conditions.

Figure 4.11 shows that the FF and J_{SC} follow the same trajectory as PCE. The triple cation device generally has better performance during no illumination hours; however, from around 10:00 (-35 °C) to 16:00 (-33 °C), the lines converge, indicating that MAPI can match the performance of the triple cation during the late morning and afternoon on Mars.

However, MAPI is less stable at the low temperatures that occur before sunrise and after sunset, specifically below -34 °C, due to the higher fluctuations in PCE, FF, and J_{SC}. This comes as a surprise though, as thermal stepping measurements previously indicated that MAPI performs better at temperatures ≤-50 °C, while the triple cation outperforms MAPI at temperatures ≥-50 °C. Interestingly, the V_{OC} behaves differently: from 11:00 (-24 °C) to 17:00 (-43 °C), normalised V_{OC} of MAPI outperforms that of the triple cation. Furthermore, from 11:00 (-24 °C) to 16:00 (-33 °C), the J_{SC} of both devices is stable and fluctuates by only 1% from the peak values, similar to what we saw in thermal stepping measurements, where the J_{SC} remained stable from 20 °C to approximately -80 °C for MAPI and -60 °C for the triple cation.

Conclusion

In conclusion, both $MAPbI_3$ and triple cation perovskite solar cells exhibit strong stability under extreme thermal cycling from 20 °C to -125 °C, showing only minimal degradation in power conversion efficiency. $MAPbI_3$-based devices, however, experienced a more significant reduction in fill factor, resulting in a sharper decline in PCE compared to triple cation cells. Despite these variations, the overall degradation in both device types remains minimal, indicating no permanent chemical or structural damage.

Furthermore, while both devices are sensitive to the temperature variations and light exposure typical of Martian day-night cycles, triple cation perovskite solar cells demonstrate superior performance during peak light conditions and greater stability during simulated Martian night conditions. The discrepancies observed, particularly in the degradation rates of $MAPbI_3$ and triple cation devices between thermal stepping and temperature profile measurements, highlight the need for further investigation to fully understand and optimize the performance of perovskite solar cells under the unique environmental conditions on Mars.

References

1. Cheacharoen R, Rolston N, Harwood D, Bush KA, Dauskardt RH, McGehee MD. Design and understanding of encapsulated perovskite solar cells to withstand temperature cycling. Energy & Environmental Science. 2018;11(1):144-50
2. Barbé J, Pockett A, Stoichkov V, Hughes D, Lee HK, Carnie M, Watson T, Tsoi WC. In situ investigation of perovskite solar cells' efficiency and stability in a mimic stratospheric environment for high-altitude pseudo-satellites. Journal of Materials Chemistry C. 2020;8(5):1715-21
3. Yang W, Zhong D, Shi M, Qu S, Chen H. Toward highly thermal stable perovskite solar cells by rational design of interfacial layer. Iscience. 2019 Dec 20;22:534-43
4. Wu N, Wu Y, Walter D, Shen H, Duong T, Grant D, Barugkin C, Fu X, Peng J, White T, Catchpole K. Identifying the cause of voltage and fill factor losses in perovskite solar cells by using luminescence measurements. Energy Technology. 2017 Oct;5(10):1827-35.
5. Huang F, Jiang L, Pascoe AR, Yan Y, Bach U, Spiccia L, Cheng YB. Fatigue behavior of planar CH3NH3PbI3 perovskite solar cells revealed by light on/off diurnal cycling. Nano Energy. 2016 Sep 1;27:509-14
6. Sheikh AD, Munir R, Haque MA, Bera A, Hu W, Shaikh P, Amassian A, Wu T. Effects of high temperature and thermal cycling on the performance of perovskite solar cells: acceleration of charge recombination and deterioration of charge extraction. ACS applied materials & interfaces. 2017 Oct 11;9(40):35018-29
7. Chen M, Dong Y, Zhang Y, Zheng X, McAndrews GR, Dai Z, Jiang Q, You S, Liu T, Harvey SP, Zhu K. Stress Engineering for Mitigating Thermal Cycling Fatigue in Perovskite Photovoltaics. ACS Energy Letters. 2024 May 8;9:2582-9
8. Khenkin MV, KM A, Visoly-Fisher I, Kolusheva S, Galagan Y, Di Giacomo F, Vukovic O, Patil BR, Sherafatipour G, Turkovic V, Rubahn HG. Dynamics of photoinduced degradation of perovskite photovoltaics: from reversible to irreversible processes. ACS Applied Energy Materials. 2018 Jan 29;1(2):799-806
9. Rodriguez-Manfredi JA, De la Torre Juárez M, Sanchez-Lavega A, Hueso R, Martínez G, Lemmon MT, Newman CE, Munguira A, Hieta M, Tamppari LK, Polkko J. The diverse meteorology of Jezero crater over the first 250 sols of Perseverance on Mars. Nature Geoscience. 2023 Jan;16(1):19-28.
10. Zhou Q, Wang B, Meng R, Zhou J, Xie S, Zhang X, Wang J, Yue S, Qin B, Zhou H, Zhang Y. Understanding temperature-dependent charge extraction and trapping in perovskite solar cells. Advanced Functional Materials. 2020 May;30(22):2000550.
11. Hoang MT, Yang Y, Tuten B, Wang H. Are metal halide perovskite solar cells ready for space applications? The journal of physical chemistry letters. 2022 Mar 25;13(13):2908-20
12. Royal Museums Greenwich. How long is a day on Mars? London: Royal Museums Greenwich. [Internet]. Available from: https://www.rmg.co.uk/stories/topics/how-long-day-on-mars

Chapter 5: Humidity Resistance of Polyimide/Epoxy/Glass Encapsulation for Perovskite Solar Cells

This chapter explores the performance of the Polyimide/Epoxy/Glass encapsulation technique on perovskite solar cells exposed to high humidity. Through a series of experiments, we examine the influence of humidity variations on the key photovoltaic parameters – PCE, V_{OC}, FF and J_{SC}.

The chapter is divided into four main sections: humidity stepping, humidity cycling, Jezero Crater humidity profile, and 90% relative humidity endurance testing. Each section details specific experimental conditions and their effects on the performance of the perovskite solar cells. Throughout the study, multiple iterations of both $MAPbI_3$ and triple cation devices were fabricated and tested. J-V measurements were conducted using the humidity-controlled stage under 0.4 sun AM0 illumination and under nitrogen gas environment. The pressure was maintained at approximately 0.1 bar at 90% RH and ~1 bar at 10% RH. This difference in pressure at the minimum and maximum relative humidity levels was necessary to ensure a consistent ramp rate, achieved by gradually controlling the pressure valve of the nitrogen flow line. These conditions were designed to simulate the atmosphere of Mars.

The results indicate that Polyimide/Epoxy/Glass encapsulation provides adequate protection in low-humidity environments (<30% RH). However, at higher humidity levels (>90% RH), this encapsulation method proves insufficient in preventing moisture-induced degradation. These findings highlight the need for a better encapsulation strategy to ensure the long-term stability of perovskite solar cells in extraterrestrial and high relative humidity environments.

5.1 Humidity Stepping

5.1.1 Humidity Stepping Measurement of $MAPbI_3$-Based Device

The degradation of perovskite materials, especially the widely used methylammonium lead iodide ($CH_3NH_3PbI_3$) in the presence of water is a well-documented phenomenon [1]. The weak Pb–I ionic bonds and the volatile CH_3NH_3I component in the lattice structure of $CH_3NH_3PbI_3$ contribute to its instability in humid environments. Water molecules can promote the decomposition of perovskites into CH_3NH_2, HI, and PbI_2, with HI further decomposing into H_2 and I_2 when exposed to light or oxygen. This process accelerates the overall degradation of the perovskite material [2]. The specific decomposition processes of $CH_3NH_3PbI_3$ are shown as follows:

$$
\begin{aligned}
&4CH_3NH_3PbI_3 + 4H_2O \leftrightarrow 4(CH_3NH_3PbI_3\cdot H_2O) \\
&\quad \rightarrow (CH_3NH_3)_4PbI_6\cdot 2H_2O + 3PbI_2 + 2H_2O \\
&\qquad\quad \rightarrow 4CH_3NH_3I + 4PbI_2 + 4H_2O.
\end{aligned}
$$

Figure 5. 1: hydration decomposition processes of $CH_3NH_3PbI_3$.

The first reaction of the degradation process is the formation of monohydrate ($CH_3NH_3PbI_3\cdot H_2O$) which can be reversed to the original $CH_3NH_3PbI_3$ (or $MAPbI_3$) under dry conditions. Further incorporation of H_2O results in the irreversible formation of dihydrate $(CH_3NH_3)4PbI_6\cdot 2H_2O$ and PbI_2 (fig. 5.1). It is likely that the irreversibility of monohydrate-to-dihydrate reaction is due to the formation of separate solid-phase of PbI_2, as well as the further dissolution of the organic cation in the dihydrate, leading to its decomposition into PbI_2 [3].

Humidity not only promotes the hydrolysis of perovskites, which is a chemical reaction in which water molecules break down other molecules but also distorts the hydrogen bonding between the organic and inorganic components of the perovskite structure. This leads to the formation of pinholes which are tiny, often microscopic, voids or defects. Pinholes adversely affect the diffusion length, generation of charge carriers, mobility, charge carrier dynamics, and overall photovoltaic properties of the materials [4]. Furthermore, Wang *et al*. reported that higher relative humidity values cause a rapid reduction in the ability of the perovskite thin film to absorb light, altering the charge recombination mechanism from bulk-dominated to surface-mediated recombination due to interfacial charge accumulation [5].

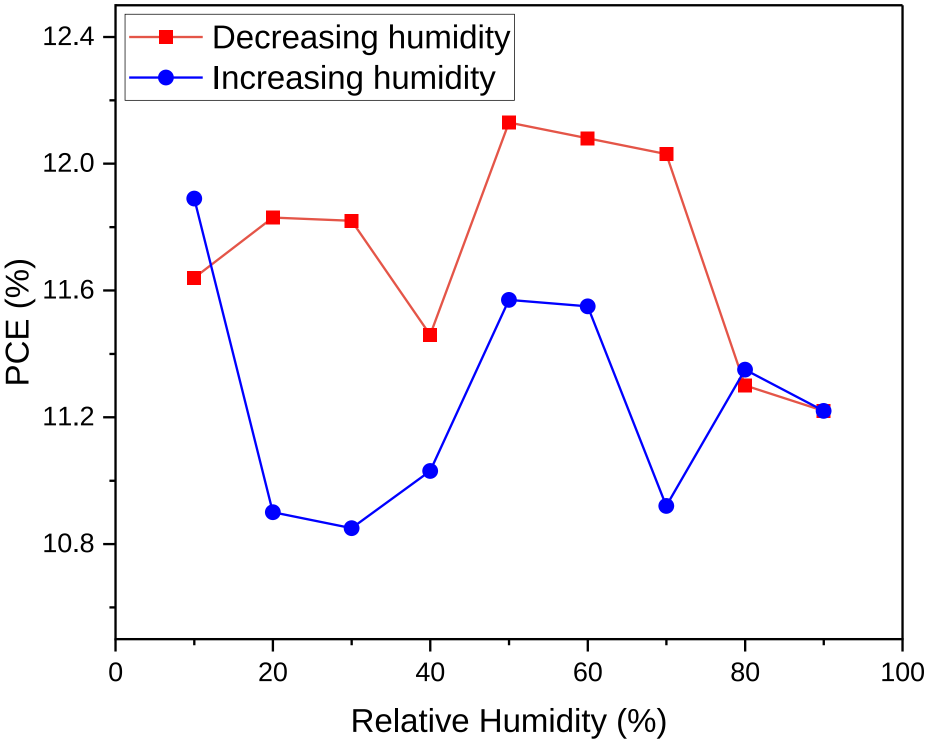

Figure 5. 2: PCE under 0.4 sun AM0 (54.7 mW/cm^2) intensity versus humidity of the $MAPbI_3$-based device. The relative humidity was first increased from 10% to 90% RH, then RH decreased back to 10%.

Fig. 5.2 shows the 0.4 sun AM0 (54.7 mW/cm^2) performance parameters of $MAPbI_3$-based device plotted against relative humidity, ranging from 10% to 90% RH. Relative humidity is the amount of moisture in the air expressed as a percentage. This range was selected to mimic the extreme humidity variations found in Martian environments and to match the capabilities of the humidity controller.

Humidity was initially increased from 10% to 90% RH and decreased back to 10% RH, in 10% RH increments. As illustrated in figure 5.2, the data shows considerable variability.

At an initial humidity of 10% RH, the PCE starts at 11.89%. As humidity increases, the PCE generally declines until reaching 30% RH, where it drops to 10.85%. Beyond this point, the PCE shows slight recovery and stabilises around 11.55% at 60% RH, before dropping again to 10.92% at 70% RH, 11.35% at 80% RH, and 11.22% at 90% RH. When the humidity is reduced from 90% back to 10% RH, the PCE initially increases, peaking at 12.13% at 50% RH. It then slightly decreases but remains relatively stable at 11.64% at 10% RH, which is 0.25% lower than the initial PCE recorded at the start of the measurement. Given the difficulty in deriving a conclusive trend from Figure 5.2, we will focus on the humidity data starting at 10% RH and ending at 90% RH.

Leguy *et al*. related the efficiency drop after moisture exposure to the isolation of perovskite grains, which reduces charge transport and increases recombination at grain interfaces, thereby shortening the charge diffusion lengths [3].

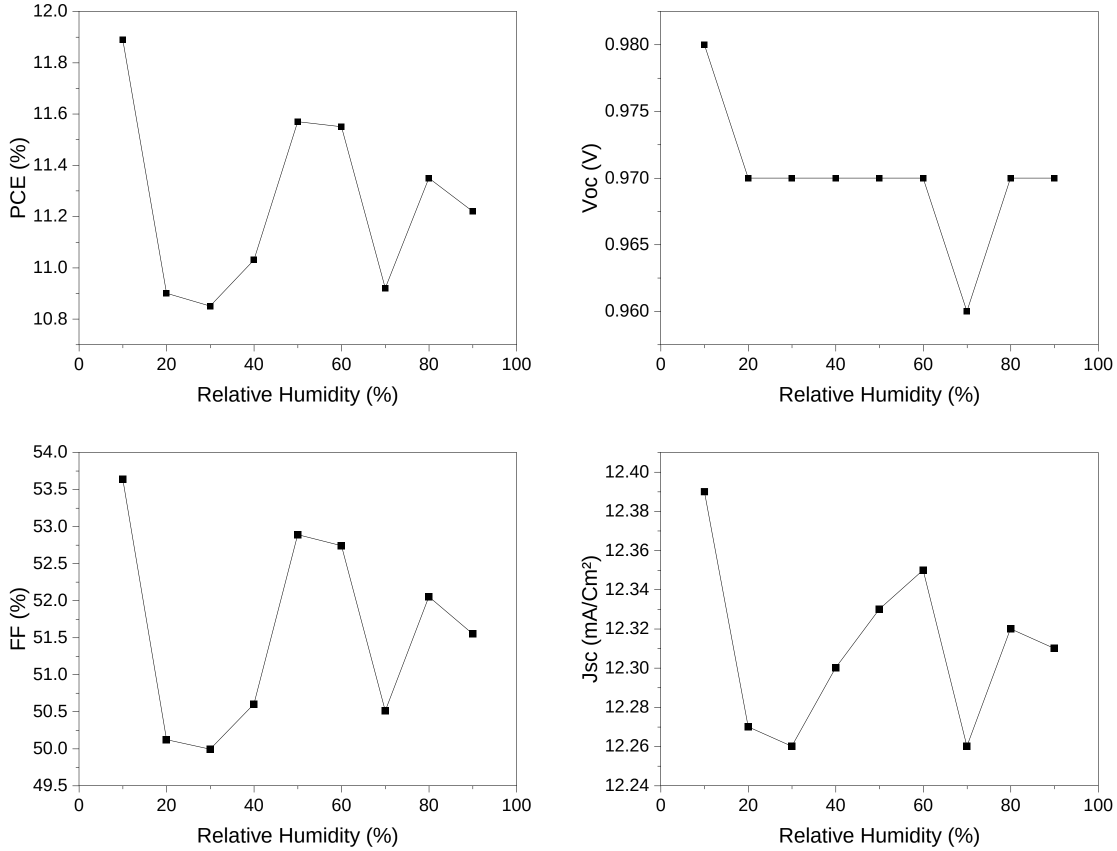

Figure 5. 3: 0.4 AM0 intensity, PCE, V_{OC}, FF and J_{SC} humidity stepping results of $MAPbI_3$-based device.

In Figure 5.3, PCE, V_{OC}, FF and J_{SC} humidity stepping results of $MAPbI_3$-based device. The figure indicates a slight decrease in PCE with increasing humidity, with an average PCE change of -0.08375% per 10% RH step. Similarly, V_{OC} shows a minor negative trend, nonetheless, throughout the measurement period V_{OC} remains relatively stable, fluctuating between 0.98 and 0.96 V.

The J_{SC} is very stable: it decreases from 12.39 mA/cm² at 10% RH to 12.26 mA/cm² at 30% RH, then increases to 12.35 mA/cm² at 60% RH, followed by further fluctuations to 12.26, 12.32, and 12.31 mA/cm² at 70%, 80%, and 90% RH, respectively.

The FF fluctuates throughout the measurement, peaking at 53.64% at 10% RH and reaching a low of 49.99% at 30% RH.

The good stability observed at 90% RH can be attributed to several factors. Firstly, the devices were encapsulated using glass-glass encapsulation. This method creates a closed environment around the PSC, significantly reducing the ingress of water molecules into the perovskite material, thereby improving the humidity stability of the device [1]. Secondly, the device was maintained at each humidity level for only 3 minutes, which might be insufficient time for moisture to cause damage, as it is known that the performance tends to decrease due to the decomposition of the materials with respect to the moisture exposure time [6]. Further analysis is required to determine the impact of these conditions on an unencapsulated device and what encapsulation methods work best. The interaction between humidity and the structural integrity of perovskite films also depends on the type of hole transport layers used. For example, Yang *et al*. evaluated the impact of Spiro-OMeTAD, P3HT and PTAA HTLs on the rate of perovskite decomposition and showed that Spiro-OMeTAD appears to accelerate the perovskite decomposition process, whereas PTAA and P3HT appear to act as barriers to moisture ingress. For example, the high molecular weight of P3HT provides better adhesion to the varied morphology of perovskite, effectively blocking moisture penetration, whereas the small molecules of Spiro-OMeTAD are prone to cracking under water vapour, allowing moisture to attack the perovskite layer [7]. Salado *et al*. further confirmed this [6]. Thus, it is likely that the reduced stability of $MAPbI_3$/ Spiro-OMeTAD devices is linked to both – the breakdown of the perovskite material and its higher susceptibility to water, which in turn leads to the deterioration of Spiro-OMeTAD. These results display that moisture can influence the performance of perovskite solar cells.

5.1.2 Humidity Stepping Measurement of Triple Cation-Based Device

The performance of triple cation perovskite under varying humidity levels is presented in figure 5.4. In contrast to the MAPI-based device, the trend of triple cation PSC is more discernible. At 10% RH, the PCE starts at 14.31%, decreasing to 13.51% at 60% RH, which corresponds to a 5.6% reduction from its initial value. Subsequently, the PCE slightly increases to 13.87% at 80% RH before falling again to 13.64% at 90% RH. The average PCE change with every step is -0.08375%, which is the same as the MAPI-based device.

The open-circuit voltage demonstrates a downward trend with increasing humidity, decreasing from 1.1 V at 10% RH to 1.08 V at 90% RH, representing a marginal 1.8% reduction.

The fill factor also shows a decline, starting from 60.5% at 10% RH and dropping to 58.85% at 20% RH. It further decreases to 57.84% at 70% RH, but ends slightly above that, at 58.49% at 90% RH.

At 10% RH, J_{SC} is 11.71 mA/cm^2 and remains stable up to 60% RH. But interestingly, it then jumps to 11.98 mA/cm^2 at 70% and 80% RH, due to unknown reasons, before slightly decreasing to 11.84 mA/cm^2 at 90% RH.

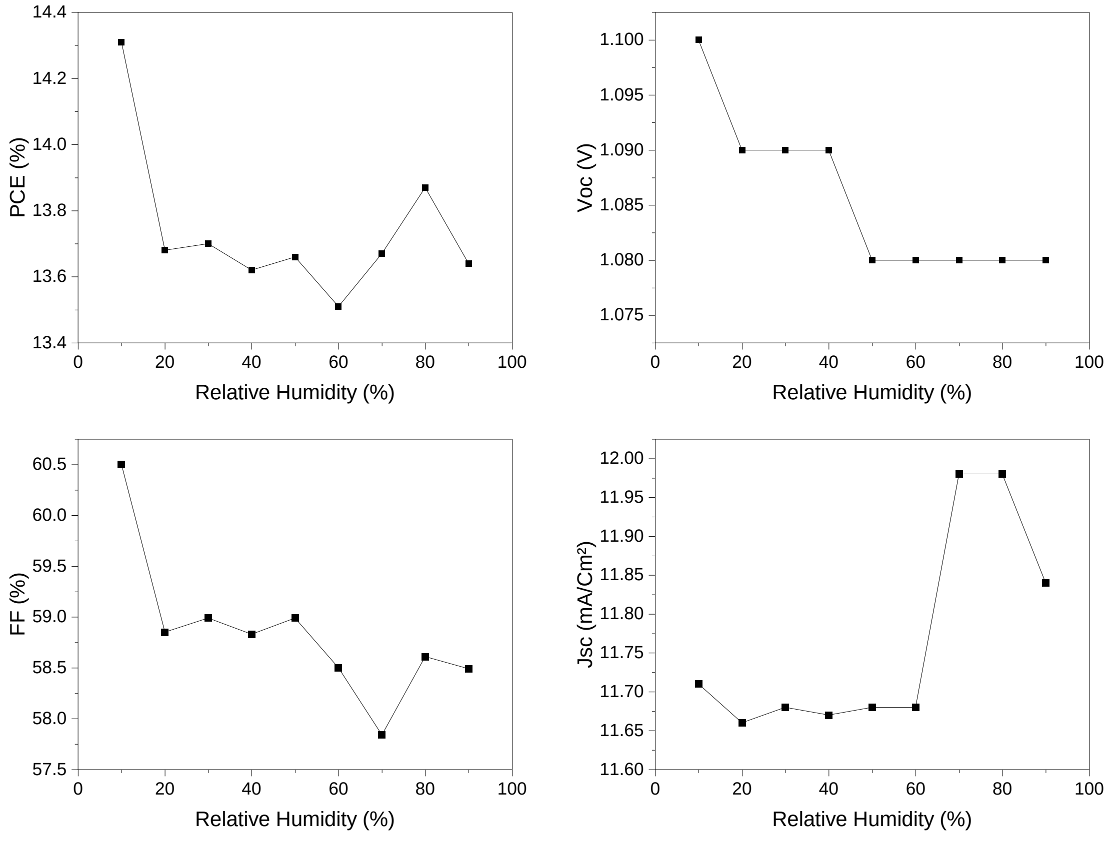

Figure 5. 4: 0.4 AM0 intensity, PCE, V_{OC}, FF and J_{SC} humidity stepping results of triple cation-based device.

5.1.3 Comparison of Humidity Stepping Results Between $MAPbI_3$ and Triple Cation-Based Devices

When comparing $MAPbI_3$ and triple cation perovskite devices under varying humidity levels, several distinctions in performance metrics become evident.

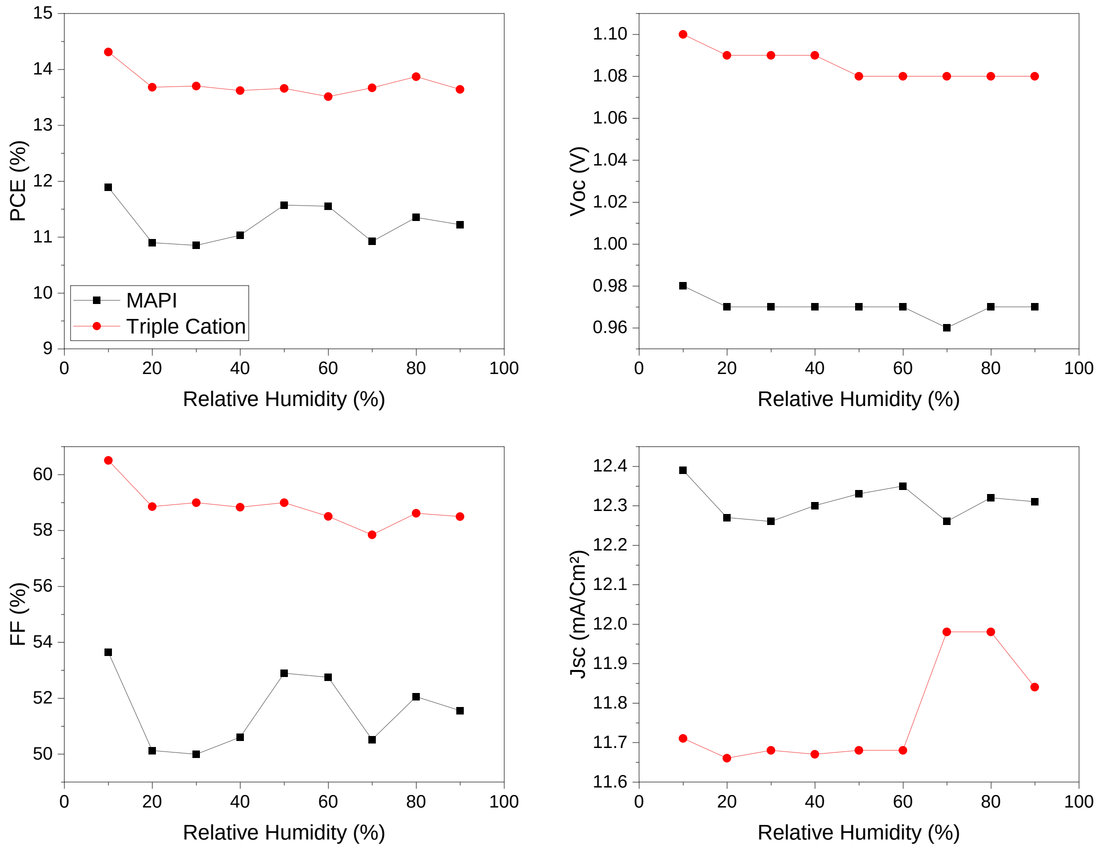

Figure 5. 5: Comparison of the humidity stepping performance parameters between $MAPbI_3$ and triple cation-based devices.

The triple cation device exhibits significantly higher PCE, ranging from 14.31% at 10% relative humidity to 13.64% at 90% RH, as shown in fig. 5.5. In contrast, the MAPI-based device starts at 11.89% PCE at 10% RH and decreases to 11.22% at 90% RH. Despite this difference in absolute performance, the percentage change in PCE between 10% RH and 90% RH is remarkably close for both devices, with MAPI degrading by 5.6% and the triple cation degrading by 4.7%.

The decline in V_{OC} for both perovskites is minor, with $MAPbI_3$ fluctuating between 0.98 V (at 10% RH) and 0.96 V (at 70% RH) and TC decreasing from 1.1 V (at 10% RH) to 1.08 V (at 90% RH) (fig. 5.5).

$MAPbI_3$ shows irregular J_{SC} trends, with fluctuations at various RH levels. In contrast, TC remains stable up to 60% RH and even shows an increase at higher RH levels, indicating better stability and resilience to increased RH.

5.2 Humidity Cycling

5.2.1 Comparison of Humidity Cycling Results Between $MAPbI_3$ and Triple Cation-Based Devices

To begin, figure 5.6 presents the power conversion efficiency of both MAPI and triple cation-based devices throughout the measurement period.

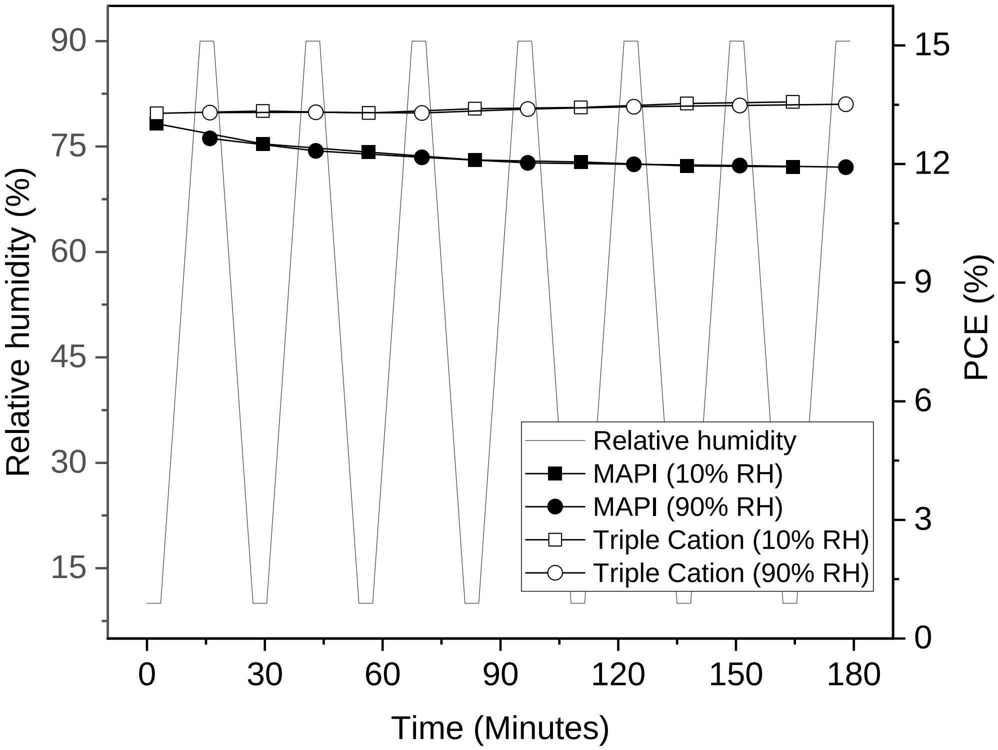

Figure 5. 6: Comparison of the humidity cycling PCE between $MAPbI_3$ and triple cation-based devices.

The encapsulated MAPI device shows a slight, linear degradation in PCE with each cycle, averaging a loss of -0.085% PCE per half cycle. The initial PCE recorded at 10% RH is 13.02%, while after six cycles (approximately 3 hours), the final PCE measured at 90% RH is 11.92%, representing an 8.5% reduction. In contrast, the triple cation device demonstrates excellent performance stability during the measurement, assuming that encapsulation quality is the same for both devices. Initially, the PCE is measured at 13.28% and, interestingly, it gradually increases by approximately 0.0177% per measurement, resulting in a final PCE of 13.51%, marking a 1.73% improvement in efficiency.

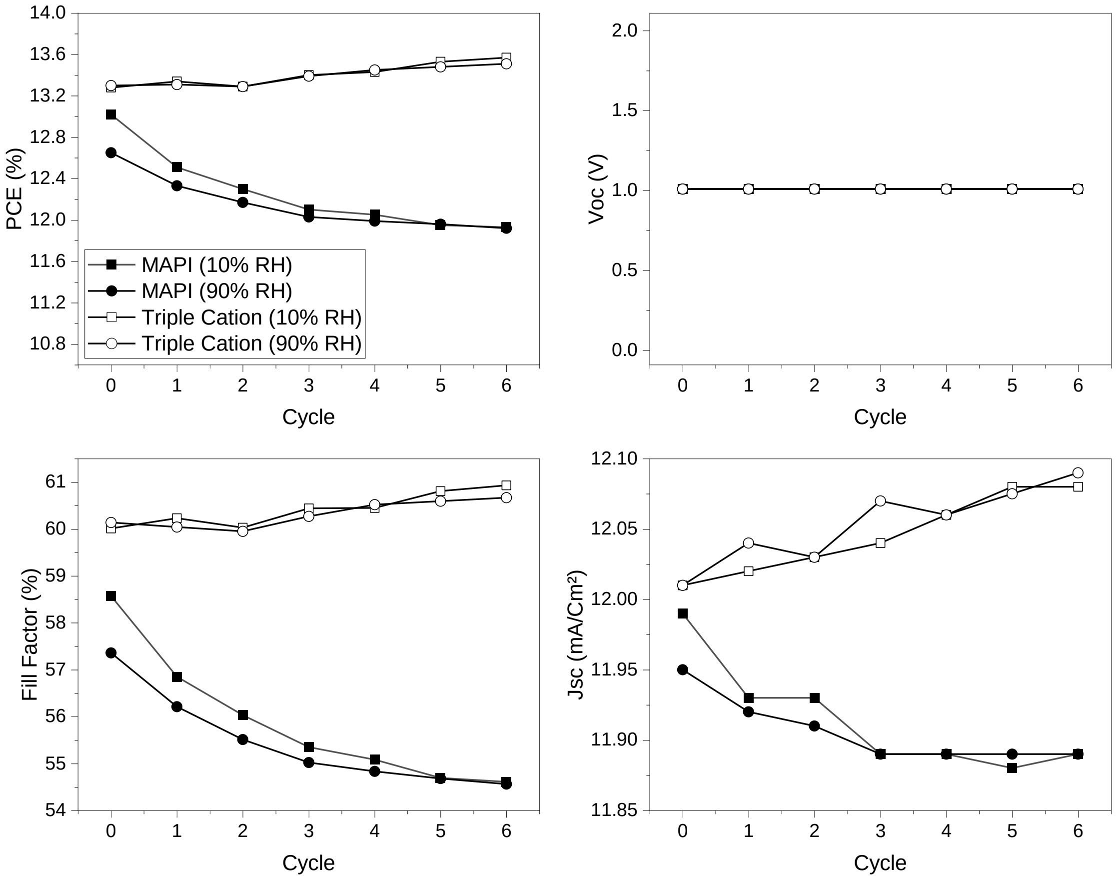

Figure 5. 7: PCE, V_{OC}, FF, J_{SC}, as a function of humidity cycle of $MAPbI_3$ and triple cation-based devices.

As depicted in figure 5.7, the open-circuit voltage for both MAPI and triple cation devices remains constant at 1.01 V throughout the entire measurement period. The fill factor of the MAPI device starts at 58.57% and declines to 54.56%, a reduction of 6.85%. Conversely, the fill factor for the triple cation device slightly increases from 60.01% to 60.67%. Lastly, the short-circuit current density remains stable for both devices. For the MAPI device, J_{SC} decreases slightly from 11.99 to 11.89 mA/cm^2, while for the triple cation device, J_{SC} increases marginally from 12.01 to 12.09 mA/cm^2. This means that the FF is the main parameter causing the PCE reduction for MAPI and PCE increase for triple cation.

Research by Mishra *et al*. proved that reducing humidity levels to below 50% RH can recover the performance of $MAPbI_3$-based devices if the degradation is modest up to that point [8]. This recovery occurs because drying reduces the number of trap states in the perovskite material, as described in studies on the effect of humidity on perovskite solar cells. In our study, the exposure time to high relative humidity levels above 50% is brief before the devices are dried with the humidity reduced to below 50%. This limited exposure prevents significant degradation, ensuring minimal performance loss for both devices, especially the triple cation device. Therefore, it is plausible that any slight degradation experienced during a brief period at 90% RH can fully recover when the RH is reduced back to 10%.

The superior humidity cycling performance of triple cation perovskites compared to $MAPbI_3$ can be attributed to the incorporation of Cs and FA cations into the $MAPbI_3$ matrix but could also likely be caused by better encapsulation quality for those particular devices. While MA cations are known for their poor humidity stability, Cs and FA cations help improve the overall stability of perovskite structures in high humidity environments [6].

5.3 Jezero Crater Humidity Profile

5.3.1 Jezero Crater Humidity Profile Measurement of The $MAPbI_3$-Based Device

During the 24-hour Jezero Crater humidity profile measurement, the power conversion efficiency values of the MAPI perovskite solar cells vary between 12.26% and 12.78% (fig. 5.8), resulting in an overall percentage change of only ~4.1%. The highest PCE is observed at 14:00 local Mars time (10% RH), while the lowest is recorded at 6:00 local Mars time (30% RH), indicating that diurnal humidity changes impact the solar cell performance.

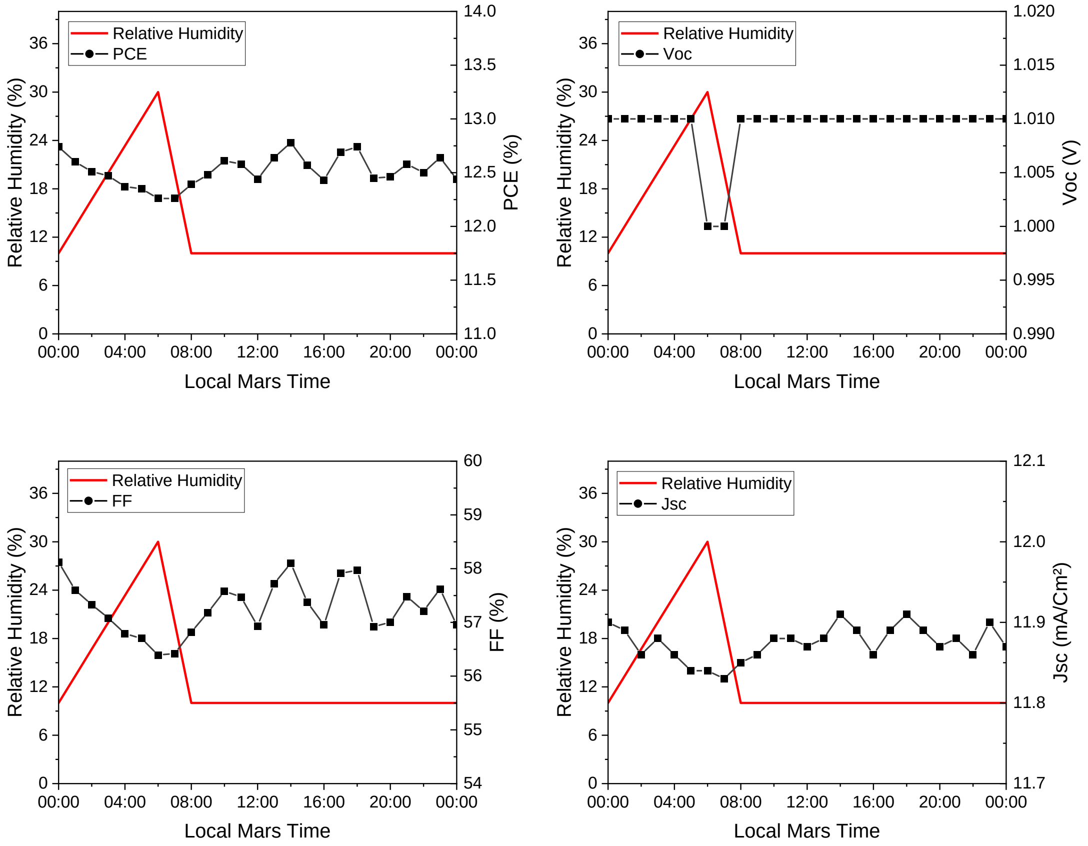

Figure 5. 8: PCE, V_{OC}, FF and J_{SC} of the $MAPbI_3$-based device during a simulated Martian day.

The open-circuit voltage remains relatively stable, fluctuating between 1.00 V and 1.01 V throughout the experiment. These minor variations in V_{OC} suggest resilience to the simulated diurnal humidity changes. The fill factor also shows slight variations, with the highest value of 58.12% recorded at 00:00 and the lowest – 56.49%, at 6:00 local Mars time, a percentage change of only 3%. The short-circuit current density ranges from 11.83 mA/cm² to 11.91 mA/cm². Like PCE, J_{SC} reaches its peak at 14:00 local Mars time and its lowest point at 6:00 local Mars time.

5.3.2 Jezero Crater Humidity Profile Measurement of The Triple Cation-Based Device

During the simulated Jezero Crater humidity profile measurement, the PCE values of the triple cation-based perovskite solar cell varies between 13.57% and 14.29% (figure 5.9), resulting in an overall percentage change of 5.3%.

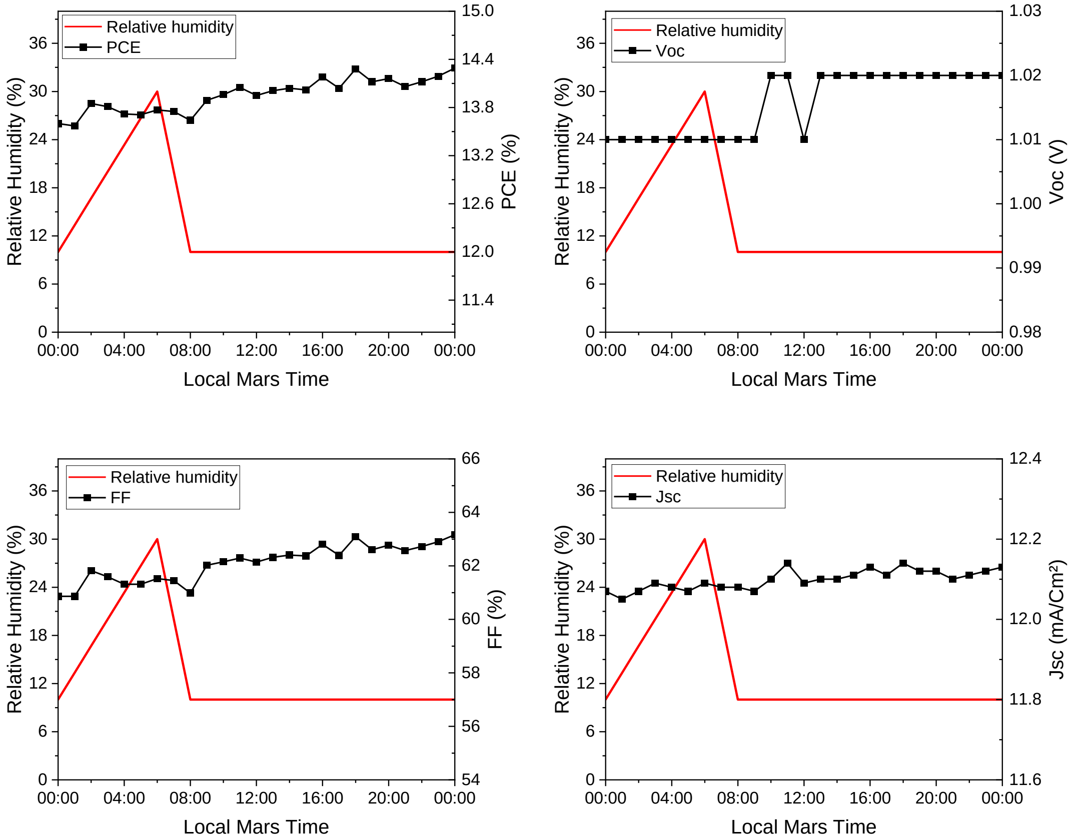

Figure 5. 9: PCE, V_{OC}, FF and J_{SC} of the triple cation-based device during a simulated Martian day.

The highest PCE of 14.29% was recorded at 24:00 local Mars time (10% RH), while the lowest PCE of 13.57% occurred at 6:00 local Mars time (30% RH), indicating that diurnal humidity changes impact the performance of the device. As the day progresses, the PCE of triple cation rises, which could be because after 06:00, the RH declines from 30% to 10% and stays there until 24:00. The V_{OC} remains stable, fluctuating between 1.01 V when RH was mostly above 10% and 1.02 V throughout the experiment. The FF is also stable, with slight variations; the highest value of 63.16% was recorded at 24:00, and the lowest value of 60.86% was recorded at 00:00 local Mars time, representing a percentage change of approximately 3.8%. The J_{SC} ranges from 12.05 mA/cm² at 01:00 to 12.14 mA/cm² at 11:00.

5.3.3 Comparison of Jezero Crater Humidity Profile Results Between $MAPbI_3$ and Triple Cation-Based Devices

The performance of MAPI PSC exhibits minimal sensitivity to changes in relative humidity within the 10-30% range. As depicted in figure 5.10, the PCE varies between 12.26% and 12.78%, which is only a 4.1% change. Similarly, the triple cation-based device also responds well to low humidity variations, with PCE ranging from 13.57% to 14.29%. V_{OC} and J_{SC} both remain extremely stable throughout the measurement, varying by only ±1%, while FF is fluctuating slightly more, but only ±4-5%.

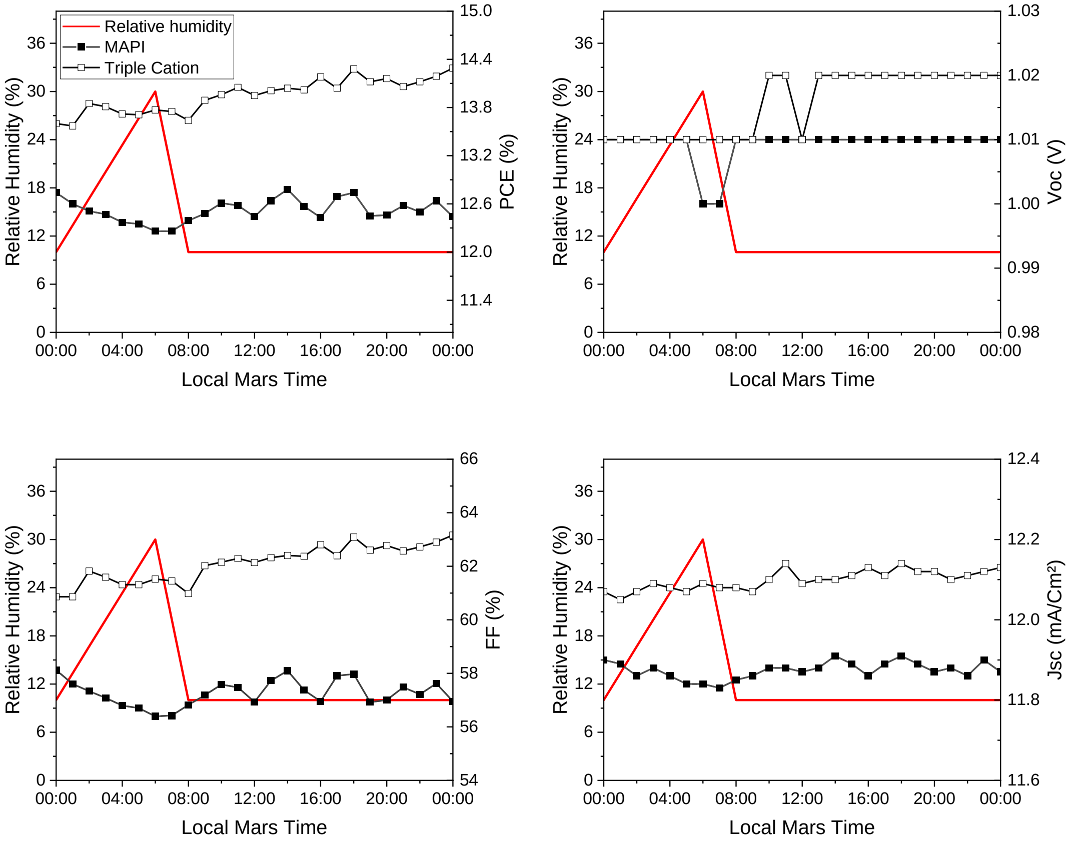

Figure 5. 10: Comparison of the PCE, V_{OC}, FF and J_{SC} of the $MAPbI_3$ and triple cation-based devices during a simulated Martian day.

5.4 90% Relative Humidity Endurance

5.4.1 Comparison of 90% Relative Humidity Endurance Results Between MAPbI$_3$ and Triple Cation-Based Devices

Firstly, for identifying the humidity stability of perovskite, devices are kept at room temperature (~20 °C), in a nitrogen filled stage (0.1 bar), as light-activated oxygen degradation and thermal effects have substantially key roles in the degradation process and J-V measurements were recorded under $0.4 \times AM0$ intensity. The decomposition rate of perovskite film is substantially related to the exposure degree to RH. Exposure to high relative humidity (>80%) can be short, but represent fast transfer to hydration and PbI$_2$, hence perovskite decomposition [7].

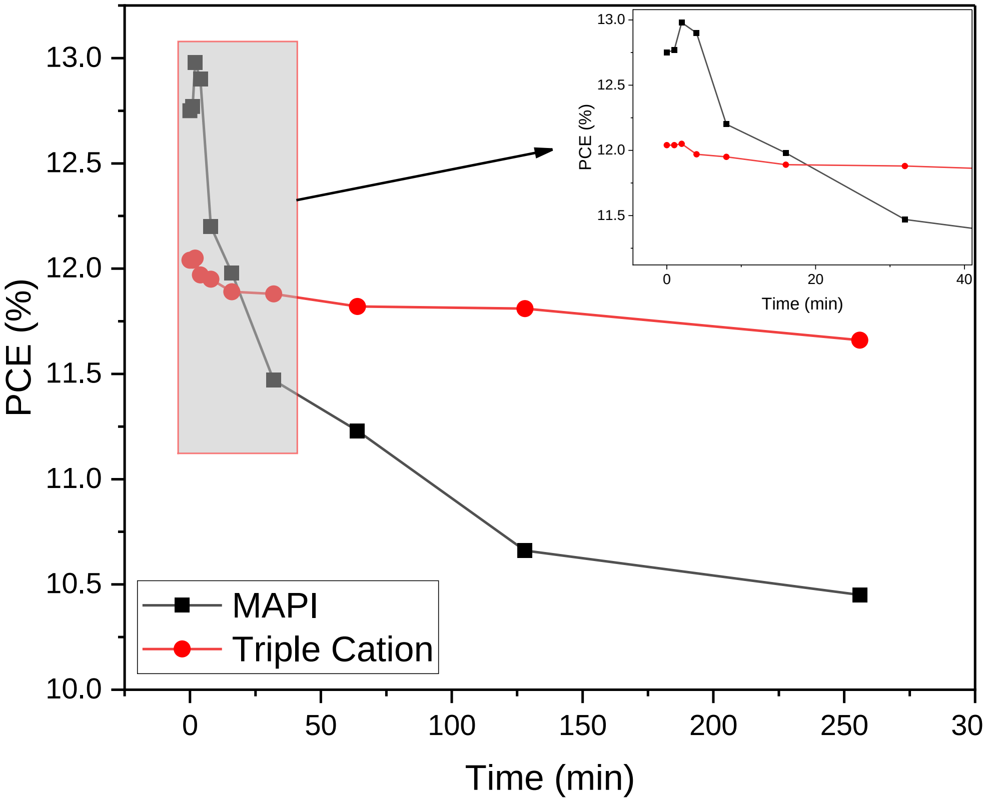

Figure 5. 11: PCE comparison between MAPbI$_3$ and triple cation perovskite solar cells during the first 256 minutes of exposure to 90% relative humidity.

Figure 5.11 illustrates the stability of the PCE for both $MAPbI_3$ and TC perovskite devices under 90% relative humidity conditions. Initially, both devices exhibit stable PCE measurements. The MAPI device starts with a PCE of 12.75%, which slightly increases to 12.77%, 12.98%, and 12.9% after 1, 2, and 4 minutes of exposure. However, as time passes, the effect of humidity starts to affect the device and the PCE begins to decline. After 8 minutes, the PCE drops to 12.2%, while after 256 minutes at 90% RH, the PCE falls to 10.45% – a reduction of approximately 18% from the initial measurement. After 24 hours, the MAPI device is no longer functional, with a PCE of just 0.01% (table SB.9).

It has been indicated that grain boundaries and defects facilitate the absorption of H_2O molecules, leading to structural decomposition in $MAPbI_3$. This process generates new grain boundaries over time. The ingress of H_2O molecules breaks down entire perovskite grains into smaller fragments, thereby increasing the number of grain boundaries and creating more defect states at surfaces and interfaces [10]. Moreover, trapped charges along grain boundaries have been shown to drive irreversible deterioration during moisture-induced degradation [11].

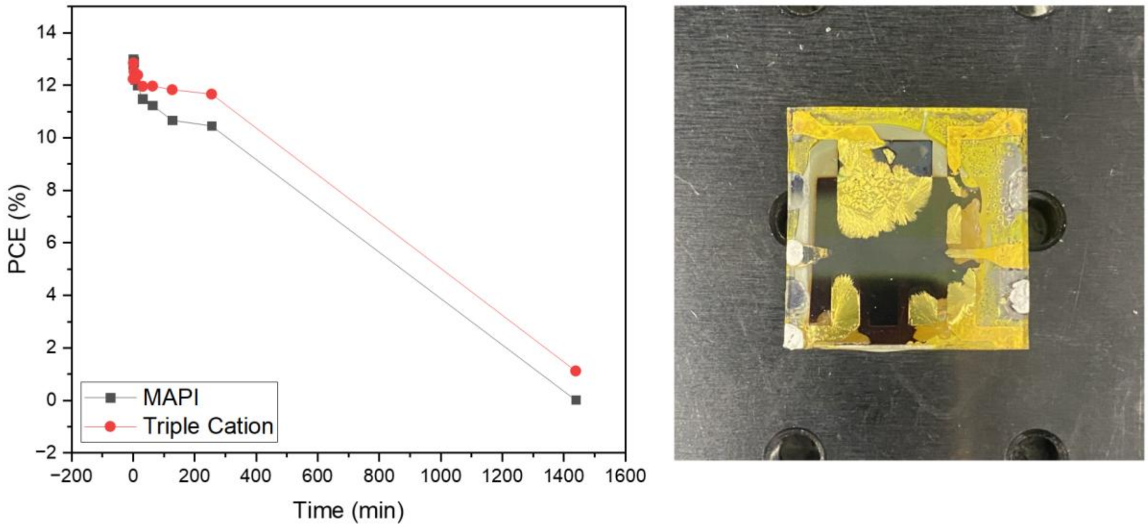

Figure 5. 12: PCE comparison between $MAPbI_3$ and triple cation perovskite solar cells under 90% relative humidity endurance measurement (left). The right side shows a degraded triple cation-based device after 24 hours of exposure to 90% RH.

The triple cation device shows a similar trend but with greater resilience to humidity. The initial PCE is 12.04% (unusually lower than MAPI-based PSC's, but likely due to the fact that this device is from a worse batch), remaining stable at 12.04% after 1 minute and slightly increasing to 12.05% after 2 minutes. Thereafter, the PCE starts to decline. After 256 minutes, the PCE measures 11.66%, reflecting a modest reduction of only about 3.2%, significantly better than the 18% decline observed for the MAPI device. However, after 24 hours, the triple cation device also shows substantial degradation, with a PCE of 1.12% (fig 5.12). The deterioration rate of crystallinity and the increase in PbI_2 phase fraction are significantly slower for triple cation perovskites compared to $MAPbI_3$ [12]. However, after 24 hours of exposure to 90% relative humidity, the device experiences complete degradation just like MAPI.

As illustrated in figure 5.12, the degradation is evidenced by the formation of PbI_2, which changes the film color from dark brown/black to pale yellow [10]. Additionally, the Au contacts appear damaged by the humidity, indicating that moisture has penetrated every layer of the device. Moreover, a recent study has reported that Au can trap water molecules and diffuse through the hole transport layer, exacerbating the degradation process [13].

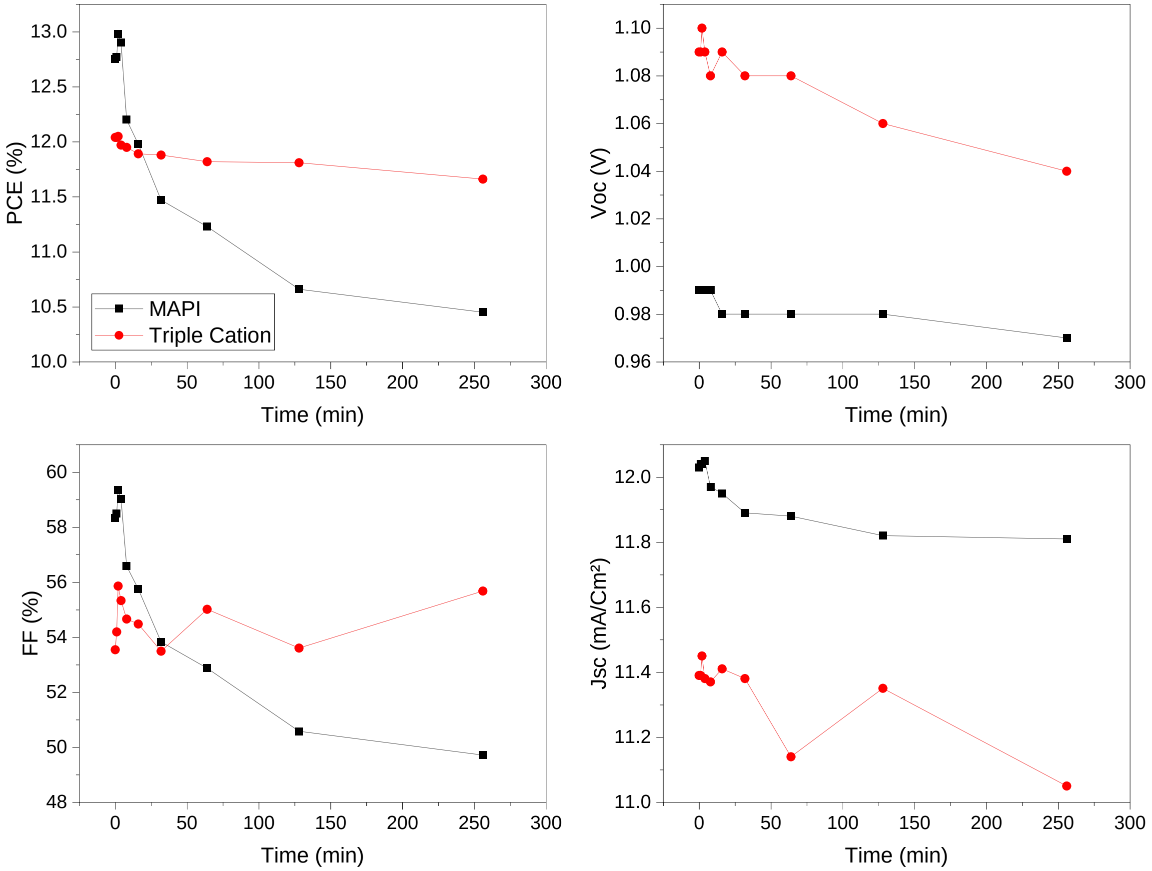

Figure 5. 13: PCE, V_{OC}, FF and J_{SC} comparison between $MAPbI_3$ and triple cation perovskite solar cells during the first 256 minutes of exposure to 90% relative humidity.

As shown in figure 5.13, the V_{OC} degrades at different rates between $MAPbI_3$ and triple cation perovskite solar cells. Darvishzadeh *et al.* modelled the change of V_{OC} over time, demonstrating that ion migration and PbI_2 defects are the primary causes of V_{OC} degradation upon moisture exposure [14]. For $MAPbI_3$, the V_{OC} remains relatively stable for the first 256 minutes, decreasing slightly from 0.99 V to 0.97 V. However, after 24 hours of exposure to 90% relative humidity, the V_{OC} drops to 0.05 V – complete degradation. In contrast, the triple cation perovskite exhibits slightly more fluctuation but maintains a higher V_{OC} overall. It starts at 1.09 V and decreases to 1.04 V after 256 minutes, then drops to 0.36 V after 24 hours. Further work is required to understand the intricacies of this behaviour.

The FF is the main parameter causing the decline in PCE and shows a distinctive pattern of decline between the two types of devices. The FF of $MAPbI_3$ experiences a substantial drop from an initial 58.32% to 49.71% after 256 minutes, marking a 14.8% reduction. After 24 hours, the FF is measured at 78.19%, which must be a faulty result, but this anomalous reading does not alter the fact that the device is no longer functional. For the triple cation perovskite, the FF starts at 53.54% and fluctuates between 53.49% and 55.86%. Notably, the second highest FF of 55.68% is recorded after 256 minutes, but it declines to 33.87% after 24 hours.

The J_{SC} of $MAPbI_3$ remains relatively stable over the 256-minute period. It begins at 12.03 mA/cm², rises slightly to 12.05 mA/cm² after 4 minutes, and then trends downward to 11.81 mA/cm², representing a change of approximately 1.8% from the initial measurement. After 24 hours, the J_{SC} drops to 0.15 mA/cm². Similarly, the J_{SC} of the triple cation perovskite shows commendable stability. Initially measured at 11.39 mA/cm², it remains around this value for most measurements, with a slight decrease to 11.14 mA/cm² after 64 minutes and to 11.05 mA/cm² after 256 minutes, representing a 3% change from the initial measurement. However, after 24 hours of exposure, the J_{SC} degrades to 5.03 mA/cm².

Conclusion

The results of the humidity measurements indicate that triple-cation and $MAPbI_3$-based perovskite solar cells with Polyimide/Epoxy/Glass encapsulation exhibit a steady linear decline in performance as humidity increases. However, they maintain strong stability in low-humidity environments (10–30% RH), conditions representative of Martian regions such as Jezero Crater. This finding underscores the potential viability of perovskite photovoltaics encapsulated with Polyimide/Epoxy/Glass for specific low humidity areas. At increased humidity levels of >90% RH, however, the Polyimide/Epoxy/Glass encapsulation proves insufficient in preventing moisture-induced degradation, highlighting a critical limitation of this encapsulation technique.

Any difference in the performance between the two types of devices could have happened due to differences in encapsulation qualities, as it was a very manual process and therefore cannot be linked to the perovskite composition, although it has been found that triple cation perovskites have better humidity resistance compared to $MAPbI_3$ and this can be attributed to the incorporation of Cs and FA cations into the $MAPbI_3$ matrix. While MA cations are known for their poor humidity stability, Cs and FA cations help improve the overall stability of perovskite structures in high humidity environments [6].

These findings emphasize the need to further investigate how humidity interacts with other extraterrestrial environmental stressors, such as intense UV radiation, extreme temperature fluctuations, and atmospheric gases, which may collectively accelerate perovskite degradation beyond what moisture alone would induce. Given that prolonged moisture exposure is a well-documented cause of perovskite decomposition [10], future research should prioritize optimizing material compositions, advancing encapsulation methods, and studying the synergistic effects of multiple environmental stressors. This comprehensive approach will be essential in ensuring the long-term stability and practical deployment of perovskite solar cells in both extraterrestrial missions and harsh terrestrial environments.

References

1. Dong Q, Liu F, Wong MK, Tam HW, Djurišić AB, Ng A, Surya C, Chan WK, Ng AM. Encapsulation of perovskite solar cells for high humidity conditions. ChemSusChem. 2016 Sep 22;9(18):2597-603
2. Koushik D, Verhees WJ, Kuang Y, Veenstra S, Zhang D, Verheijen MA, Creatore M, Schropp RE. High-efficiency humidity-stable planar perovskite solar cells based on atomic layer architecture. Energy & Environmental Science. 2017;10(1):91-100
3. Leguy AM, Hu Y, Campoy-Quiles M, Alonso MI, Weber OJ, Azarhoosh P, Van Schilfgaarde M, Weller MT, Bein T, Nelson J, Docampo P. Reversible hydration of CH3NH3PbI3 in films, single crystals, and solar cells. Chemistry of Materials. 2015 May 12;27(9):3397-407
4. Qiao L, Guo M, Long R. Unveiling the Dual Role of Humidity: The Interplay with Defects Manipulating the Charge Carrier Lifetime in Metal Halide Perovskites. The Journal of Physical Chemistry Letters. 2024 Feb 1;15(6):1546-52.
5. Wang D, Wright M, Elumalai NK, Uddin A. Stability of perovskite solar cells. Solar Energy Materials and Solar Cells. 2016 Apr 1;147:255-75
6. Salado M, Contreras-Bernal L, Caliò L, Todinova A, López-Santos C, Ahmad S, Borras A, Idígoras J, Anta JA. Impact of moisture on efficiency-determining

electronic processes in perovskite solar cells. Journal of Materials Chemistry A. 2017;5(22):10917-27

7. Yang J, Siempelkamp BD, Liu D, Kelly TL. Investigation of CH3NH3PbI3 degradation rates and mechanisms in controlled humidity environments using in situ techniques. ACS nano. 2015 Feb 24;9(2):1955-63
8. Mishra AK, Shukla RK. Effect of humidity in the perovskite solar cell. Materials Today: Proceedings. 2020 Jan 1;29:836-8
9. Rodriguez-Manfredi JA, De la Torre Juárez M, Sanchez-Lavega A, Hueso R, Martínez G, Lemmon MT, Newman CE, Munguira A, Hieta M, Tamppari LK, Polkko J. The diverse meteorology of Jezero crater over the first 250 sols of Perseverance on Mars. Nature Geoscience. 2023 Jan;16(1):19-28.
10. Huang J, Tan S, Lund PD, Zhou H. Impact of H2O on organic–inorganic hybrid perovskite solar cells. Energy & Environmental Science. 2017;10(11):2284-311
11. Ahn N, Kwak K, Jang MS, Yoon H, Lee BY, Lee JK, Pikhitsa PV, Byun J, Choi M. Trapped charge-driven degradation of perovskite solar cells. Nature communications. 2016 Nov 10;7(1):13422
12. Kumar A, Kumar R, Kumar Y, Singh A, Gupta RK, Garg A, Nalwa K. Elucidating the Effect of Defect Density in the Degradation of Mapbi3 and Triple Cation-Based Perovskite Solar Cells. Available at SSRN 4710842
13. Domanski K, Correa-Baena JP, Mine N, Nazeeruddin MK, Abate A, Saliba M, Tress W, Hagfeldt A, Grätzel M. Not all that glitters is gold: metal-migration-induced degradation in perovskite solar cells. ACS nano. 2016 Jun 28;10(6):6306-14
14. Darvishzadeh P, Babanezhad M, Ahmadi R, Gorji NE. Modeling the degradation/recovery of open-circuit voltage in perovskite and thin film solar cells. Materials & Design. 2017 Jan 15;114:339-44

Chapter 6: Conclusion and Further Work

This thesis explores the performance of solution-processed perovskite solar cells, specifically those based on $MAPbI_3$ and triple cation compositions, under simulated Martian environmental conditions. Additionally, it assesses the effectiveness of Polyimide/Epoxy/Glass encapsulation in protecting the devices from humidity-induced degradation. The results demonstrate that triple cation perovskite solar cells achieve higher power conversion efficiency and enhanced stability compared to $MAPbI_3$-based devices. In particular, triple cation devices exhibit superior performance during thermal cycling and under the temperature profile of Jezero Crater. However, at temperatures below -50 °C during thermal stepping, $MAPbI_3$ cells unexpectedly outperform their triple cation counterparts, suggesting potential advantages in extremely cold conditions.

In low-humidity environments (10–30% RH), the tested encapsulation strategy appears viable for perovskite photovoltaics. However, at higher humidity levels (>90% RH), the Polyimide/Epoxy/Glass encapsulation fails to prevent moisture-induced degradation, highlighting a critical limitation that must be addressed for long-term operation in extreme environments.

Further research is necessary to investigate the unexpected decline in open-circuit voltage (V_{OC}) at decreasing temperatures, a trend that contradicts established literature. Fabricating perovskite solar cells with different layer configurations will help determine whether this phenomenon arises from device architecture or experimental conditions.

To deepen our understanding of perovskite solar cell behaviour in extreme environments, future studies should incorporate prolonged thermal stepping and cycling experiments under Martian-like conditions. Extending measurement durations to replicate the full Martian diurnal cycle will provide a more accurate assessment of long-term performance and stability. Advanced characterization techniques should be prioritized to gain deeper insights into material properties and device performance. This includes temperature-dependent X-ray diffraction (XRD) for phase stability analysis, impedance spectroscopy (IS) for investigating charge transport properties, and scanning electron microscopy (SEM) for detailed examination of material interfaces. Additionally, dark I-V measurements should be employed to precisely assess the influence of series and shunt resistances on device performance, time-resolved photoluminescence (TR_{PL}) can provide valuable information on carrier dynamics, while lifetime efficiency measurements will further clarify device degradation pathways. Moreover, irradiation studies involving high-energy rays and particle bombardment will be crucial in understanding radiation-induced degradation and its long-term impact on performance. Assessing the effects of Martian dust accumulation on optical and electrical properties will also be essential in developing protective strategies against environmental degradation.

While this research demonstrates the potential of perovskite solar cells for space applications, overcoming current limitations requires immediate advancements in material composition, encapsulation strategies, and device architecture. Addressing these challenges is essential for ensuring the long-term viability of perovskite solar cells in future Mars missions and other extraterrestrial applications.